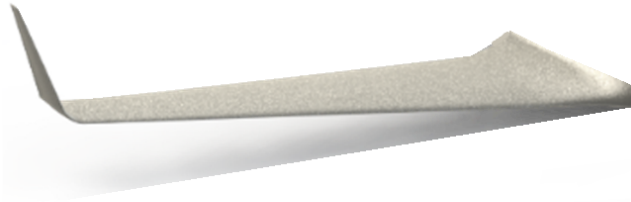# Model Updating Based on Static and Ground Vibration Tests of a Blended Wing Body Aircraft

Gonçalo Rodrigues de Araújo

Thesis to obtain the Master of Science Degree in

Aerospace Engineering

Supervisors: Prof. Afzal Suleman
Dr. José Lobo do Vale

Examination Committee

Chairperson: Prof. Fernando José Parracho Lau
Supervisor: Prof. Afzal Suleman
Member of the Committee: Prof. Hugo Filipe Diniz Policarpo

January 2021

To my parents and grandparents.

Acknowledgments

This thesis is the portrait of a stunning seven-month experience in Canada, on board of a speechless involvement supported by a unique, solid and overflowing knowledge team of engineers with many years of experience at the Center for Aerospace Research at the University of Victoria. These were times that enriched my intellect, that expanded me as a human being and far-reaching, made me understand how a professional work experience is and the valorization of a united team.

Beyond a shadow of a doubt, a special thank you go to my supervisor, Professor Afzal Suleman, for this one in a lifetime opportunity of developing a Master's thesis on the other side of the world, with guidance, technical and logistics support, always available to help and conveying trust in my capabilities. Engineers that shared with me high levels of expertise, experiences and made me feel at home, truly embraced, like a family.

I intensify my words to Doctor Jose Vale. Since the first day doing a seamless co-supervision in every detail, always dedicating a lot of time and exhaustive support. An undeniable thank you.

I would also like to thank Stephen Warwick, for always being available to help, with a superb knowledge about instrumentation, and this thesis topic in general.

Finally, words are not enough to demonstrate the acknowledgment for all the passionate support given by my parents during all this journey that I call life. All the trust, experiences, opportunities, moments, that culminates in the person I am today. To them, a nondimensional thank you.

Resumo

Ao longo das últimas decadas, a indústria da aviação tem vindo a explorar novas configurações de aeronaves para um ambiente ótimo de desempenho. Durante a fase de projecto conceptual, estimativas sobre o desempenho e capacidade de voo destas novas configurações podem ser obtidas utilizando demonstradores de voo escalados. O conceito de corpo de asa misturada consiste numa aeronave de arquitetura híbrida que apresenta consideráveis vantagens em eficiência aerodinâmica. O centro de investigação aeroespacial da Universidade de Victoria está a desenvolver um veículo aéreo não tripulado (VANT) que representa, à escala de 16.5%, um modelo de teste em voo que pretende quantificar o desempenho em voo e otimizar estratégias de controlo de voo.

Esta tese apresenta estudos de testes experimentais estáticos e de vibração em solo numa asa e uma atualização do modelo de elementos finitos da estrutura da asa. O objetivo é relacionar o modelo de elementos finitos simplificado com comportamento estático e dinâmico da asa manufacturada. Este modelo atualizado vai posteriormente ser utilizado para estudos aeroelásticos. Diferentes modelos que representam o comportamento da estrutura da asa foram obtidos com precisão, no entanto, foram identificadas alguns desafios ao combinar formas de modo dinâmicas computacionais e experimentais.

Palavras-chave: Blended Wing Body, Teste de Carga Estático em solo, Análise Estática Experimental, Testes de Vibração em Solo, Análise Modal Experimental, Atualização de Modelo de Elementos Finitos.

Abstract

Over the past few decades, the aviation industry has been exploring new aircraft configurations for optimal environmental performance. During the conceptual design phase, estimation on the performance and flightworthiness of these novel configurations can be attained by using scaled flight demonstrators. The Blended Wing Body (BWB) concept consists of a hybrid architecture aircraft and it presents considerable advantages in aerodynamic efficiency. The University of Victoria Center for Aerospace Research (UVic-Cfar) is developing an Unmanned Aerial Vehicle (UAV) that represents a 16.5 % scaled flight test model to quantify flight performance and optimize flight control strategies.

This thesis presents experimental static and Ground Vibration Tests (GVT) studies on the BWB wing and an update of the finite element model for the wing structure. The goal is to correlate the simplified FEM with the static and dynamic behavior of the real structure as manufactured. This updated model will be subsequently used for aeroelastic studies. Different models that accurately represent the behaviour of the wing structure were obtained, however, some challenges were identified when trying to match the computational and experimental dynamic mode shapes.

x

I declare that this document is an original work of my own authorship and that it fulfills all the requirements of the Code of Conduct and Good Practices of the Universidade de Lisboa.

Contents

List of Tables

List of Figures

Nomenclature

Greek symbols

δ — Difference operator

ϵ — Convergence margin

λ — Wavelength

ω — Angular frequency

ϕ — Phase

π — Pi (3.14159...)

ζ — Damping coefficient

Roman symbols

$[C]$ — Damping matrix

$[G]$ — Gain matrix

$[K]$ — Stiffness Matrix

$[M]$ — Mass matrix

$[S]$ — Sensitivity matrix

A — Cross section area

A_{pq} — Residues

b — Base length of the wingbox

E — Young's Modulus

e — Thickness

f — Frequency

g — Gravity of Earth (9.80665 m/s^2)

h — Height length of the wingbox

$H(s)$ — Transfer function

j — Imaginary unit

L_{load} — Limit load

M — Moment of Inertia

P_{factor} — Proof factor

P_{load} — Proof load

s — Poles

t — Time

U_{load} — Ultimate load

f — Vector of externally applied forces

P — Vector of selected parameters value

R — Vector of responses

$u(t)$ — Vector of displacements

U — Vector of static displacements

Subscripts

a — Analytical

e — Experimental

i — Measured DOFs

o — Originally estimated

R — Vibration mode

u — Updated

x, y, z — Cartesian components

Superscripts

$'$ — First derivative

$''$ — Second derivative

-1 — Inverse

$*$ — Complex Conjugate

T — Transpose

Abbreviations

3D Three Dimensional

BWB Blended Wing Body

CAD Computer Aided Design

CAE Computer Aided Engineering

CC Correlation Coefficients

CfAR Center for Aerospace Research

CMIF Complex Mode Indicator Function

CMM Coordinate Measuring Machine

CSAC Cross Signature Assurance Criterion

CSF Cross Signature Scale Factor

DOF Degree of Freedom

EMA Experimental Modal Analysis

FEA Finite Element Analysis

FEM Finite Element Model

FFT Fast Fourier Transform

FRF Frequency Response Function

GVT Ground Vibration Tests

MAC Modal Assurance Criterion

MDOF Multiple Degree of Freedom

MMIF Multivariate Mode Indicator Function

NASA National Aeronautics and Space Administration

ODS Operational Deflection Shape

POC Pseudo-Orthogonality Check

SDOF Single Degree of Freedom

SEAMAC Sensor Elimination Algorithm by Modal Assurance Criterion

TF Transfer Function

UAV Unmanned Aerial Vehicle

USA United States of America

UVic University of Victoria

VIC Visual Image Correlation

Chapter 1

Introduction

During the last years, technology in aviation has been showing an enormous impact and importance in the development, research and study of new features to help solving day-to-day problems.

Thereby, the aspiration of this chapter is to present the reader with the project background, and proceed with the motivation and value proposition for the development of this thesis. On the following section, a topic overview can be found that presents some procedures and tools used to study the behaviour of a wing structure in static load conditions and its experiment modal response with roving hammer impacts test. A comparison between model updating through static load test and ground vibration tests will be performed to support or disavow the necessity of the realization of both tests to validate a Finite Element Model (FEM).

Then, the final objectives of this document are briefly explained and, a detailed thesis outline is presented.

1.1   Background

Nowadays aeronautics and aerospace are one of the most advanced engineering fields where there is a need to unceasingly improve and find solutions for new designs, with the objective of optimizing the performance in a specific task. Numerous companies are currently exploring unusual aircraft configurations with a strong hope to achieve a better product to implement in a near future.

Bombardier Aerospace is a global player in the transportation industry, which is pushing researchers and developers to explore a new configuration called Blended Wing Body (BWB). This hybrid architecture is being investigating to try to take advantage of the benefits of a flying wing accompanied with the benefits of a traditional aircraft: "has a more obvious centerbody, highly aerodynamic efficient outer wing providing part of the lift, and a smoothly blended (integrated) region in between." [1].

This engineering task of design, building and testing this new aircraft configuration prototype is being undertaken by the Center for Aerospace Research (CfAR) at the University of Victoria (UVic). The first model built for this project (already developed) is a 7% scaled aircraft with the main purpose of collecting dynamics data in flight to validate and improve the control models used by the autopilot. After

the success obtained with the manufacturing and testing of the small scaled aircraft, the project evoluted to a higher level of complexity with the buildup of the 16.5% scaled aircraft. This new prototype, is a 5.4 meters wingspan aircraft, currently under development. The content of this thesis is part of this prototypes wing ground testing, one of the fundamental assignments for the validation of the previously designed model.

The study of a BWB configuration in the past years has been explored not only by Bombardier but also by other companies, specially in United States of America (USA). Boeing, National Aeronautics and Space Administration (NASA) and universities in the United States (Stanford, South California, Florida and Clark-Atlanta) and also Airbus, outside of the USA, are some of the entities that are researching and the results indicate: "a significant difference in potential aerodynamic performance." "The authors conclude that a reduction of about 30% fuel burn per seat can be achieved for both BWB-800 and BWB-450 configurations in comparison with the conventional designs (requiring 3 instead of 4 engines)." [2]

This is an example of the advantages and why the aeronautical world is trying to get increased confidence in the improvements with the research studies.

Passenger planes have not been manufactured yet with this configuration but one of the aircraft shown on the figures below, (figure 1.1(a)), is called X-48B and was developed by a partnership between NASA and Boeing, previously flown a scaled model. The other figures, figures 1.1(b) and 1.1(c), are other BWB aircraft examples that have been proposed in the last decade.

(a) Nasa-Boeing X-48B   (b) DZYNE Ascent 1000 BWB   (c) DZYNE BWB-XLC

Figure 1.1: Some concepts of BWB aircraft [3].

1.2 Motivation

Being this innovative project such a complex aircraft with 24 control surface devices and approximately 5.4m wingspan, it presents a challenging level of study. Thereby, the main motivation for this thesis is to generate and optimize the properties of a beam FEM in order to match as well as possible the static and dynamic response of the original wing structure.

Ground testing of aircraft structures provides valuable information for the characterization of important aircraft behaviour, for model validation and subsequent modelling.

To answer this challenge, static load tests will represent the approximate tip deflection correspondent to 30% of a 2.5g pull up flight maneuver. Relative to the Ground Vibration Tests (GVT), the interest arises from the study of the real life modal response of this complex wing using experimental analysis.

The static and vibration ground test results will supplementary endorse the validation of the wing FEM as well as to give information of the behavior to update the characteristics of the stick beam model

developed.

To the best of the author's knowledge, the study of the differences between beam models generated from static load behaviour and modal response, in such complex wing structure, was never performed previously, neither using computational tools or experimental response correlation.

1.3 Objectives and Topic Overview

In order to perform a successive aeroelastic analysis, this thesis objective consists in generating and optimizing the properties of simplified beam FEM in order to match as well as possible the static and dynamic response of the original aircraft structure. Trying to achieve the high level of similarity between both models, mass, inertia and stiffness of structures as well as natural frequencies and modes can be quantified resorting to static load tests and vibrational tests [4]. These quantities in turn can be used for modelling and calculation of aeroservoelastic behavior or aeroelastic stability.

Generally speaking, ground testing is used for validating the quality of the assumptions in the models used during the design and provide real world information to work with from that point on [5]. Model up-dating and tuning based on experimental results increases the confidence on the model and subsequent results obtained from its use [6].

If a relatively complex representation of the structure is available, the updating of the model can be a cumbersome task to accomplish, particularly when the uncertainty in the level of the model corre-spondence to reality is high. This is a strong possibility with experimental aircraft, when manufacturing processes and structural solutions are in an early stage of development. Some tools are available for automatic or manual model updating that facilitate the communication between analysis software and provide metrics for the model-experiment comparisons [7].

Static loading tests were planned to update the stiffness and, high accuracy GVT need to be done to find experimental modal response of the structure and pair the dynamic characterization with the beam model. Once these two updated FEMs are available, they can be compared and, since GVT are expensive to perform, the static load test can be assessed to be sufficient or not to update and capture the dynamic aeroelasticity with the model thus answering the question: Is GVT required to assess the wing's aeroelastic characteristics or does a static test suffice if mass and stiffness can be matched to experimental data? One of the updated models with the experimental data will then be used to update the beam model to simplify future flutter and divergence speeds calculation.

1.4 Thesis Outline

This thesis' work reports a comparison of static load and GVT tests results with the correspond-ing predicted results based on an FEM of a wing structure, followed by the process of generating a representative beam model for a future aeroelastic dynamic instability boundary calculation.

A summary of each chapter is presented below, from a literature review to the final conclusions of the work performed.

- **Chapter 2** presents some indispensable topics on Linear and Nonlinear Modal Analysis, theoretical and practical features of Static and Ground Vibration Testing. It ends with a description of the techniques used in FEM Updating.

- **Chapter 3** starts with a brief description of the Wing FEM, presents the computational static loading results corresponding to a 2,5g pull up maneuver and finishes with the modal analysis results, frequencies and mode shapes.

- **Chapter 4** describes the static load tests, starting with a delineation of the plan used followed by an explanation on the experimental setup and finishes with the presentation of the results obtained and preliminary comparison with the FEM.

- **Chapter 5** is similar to the **Section 4** but relative to the Ground Vibration Testing. It presents the strategy and pretesting used for the experiment followed by the GVT setup and ending with results demonstration and discussion.

- **Chapter 6** reports the methodology used for the generation of the representative beam model and the model updating results obtained with the static tests and GVT results.

- **Chapter 7** discuss the conclusions, the main findings and presents the future work coming out of this thesis.

Chapter 2

State of the art, Theoretical Background and Methodology

Unmanned Aerial Vehicles (UAVs) are aircraft operated without human pilot on board, under a remote control by a human some miles away or autonomously by a on board computer and have been one of the technologies that is exponentially growing in the past decade. From the beginning of the UAV's history, the military sector was the pioneer and responsible for the earlier developments and maturation of this new technology. Since the World War II, the research done with these vehicles showed that the importance of humanity's physical involvement on the battlefield, because it is such a high risk involvement exposed to danger situations, is not strictly necessary. On the past, no weapon in history has allowed soldiers to avoid tactical battlefield risks and, with this booming of UAVs, human soldiers are now being removed from tactical operations [8].

Lately, not only the military sector has been showing interest in the developments and improvements of new UAVs but that interest has also spread through different industries. There are already developed applications on sensing, mapping, goods and equipment delivery, inspection and monitoring. Other UAVs fundamental capabilities helpful for border, traffic and maritime surveillance, wildfire fighting, agriculture, and more are already in study and being used.

There is no question the UAV's industry is booming, but that popularity growing brings a collection of benefits and challenges. The application of these technology to all of these industries comes from the advantages of not having a human on board of the aircraft. UAVs can accelerate and manoeuvre beyond the limits permitted by human biology. Despite these advantages, UAVs remain slightly controversial. Vulnerability in the command and controls of the operations, a lack of technological and operational standards needed to guide safe and consistent performance, government regulations to integrate the UAVs into the national airspace system are some of the challenges to this technology [8].

Moreover, this typology of aircraft is pronouncing a wide use in aerospace companies as flight test proof for concept validation, as is the case in this study. Improving the aircraft performance and efficiency as well as decreasing the CO_2 emissions caused by civil aviation has been intended and, in order to meet these requirements, there are different paths that can be explored. Advanced composite materials

with the purpose of weight reduction is one example and the use of materials with higher stiffness to support the implementation of higher aspect-ratio wings, is another one, both improving lift to drag ratios that enhance the overall efficiency [9].

For this designing and improving of the flight performance and efficiency of an aircraft, the dynamic aeroelasticity needs to be studied. This consists in the interactions between three important forces: elastic, inertial and aerodynamic, evidenced on the figure 2.1 [10]. The essential phenomenons and theories related with dynamic aeroelasticity in this work are detailed along this chapter.
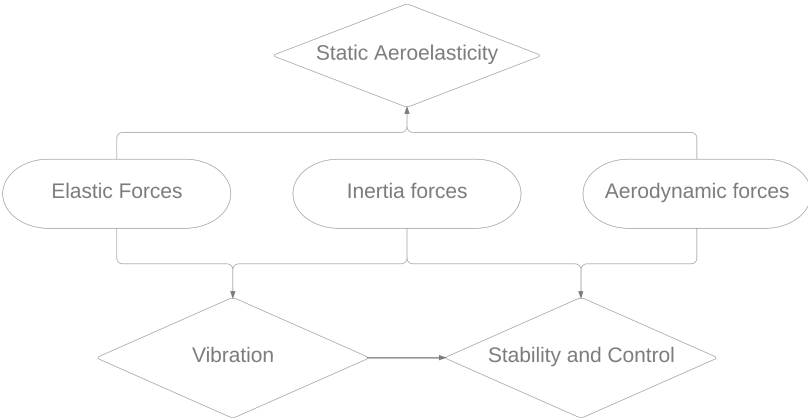
Figure 2.1: Schematic of Dynamic Aeroelasticity.

The remainder of this chapter will start with an overview of the techniques used in static testing for stiffness characterization of structures, proceeds with a discussion about the modal analysis theory, applications, data acquisition and visualization techniques and is followed by an examination of the dynamic characterization techniques used in GVT. Ending the chapter, a brief summary of the FEM updating approaches and criteria are presented.

2.1 Static Load Testing

Static aeroelasticity models the coupling effect between elastic and aerodynamic forces. It considers the non oscillatory effect of forces applied on a structure. The stiffness of the wing will influence the in-flight wing shape and consequent lift distribution, either in cruise flight or performing specific manoeuvres. However, sometimes aerodynamic calculations and computational simulations (even accurate ones) can induce errors if the structure model is not perfectly representing the test article. To tackle these differences, static tests are the best operation to confirm and validate the data [10].

For better understanding, in general, how is the design plan of a ground static test, a flowchart is presented in the figure below.
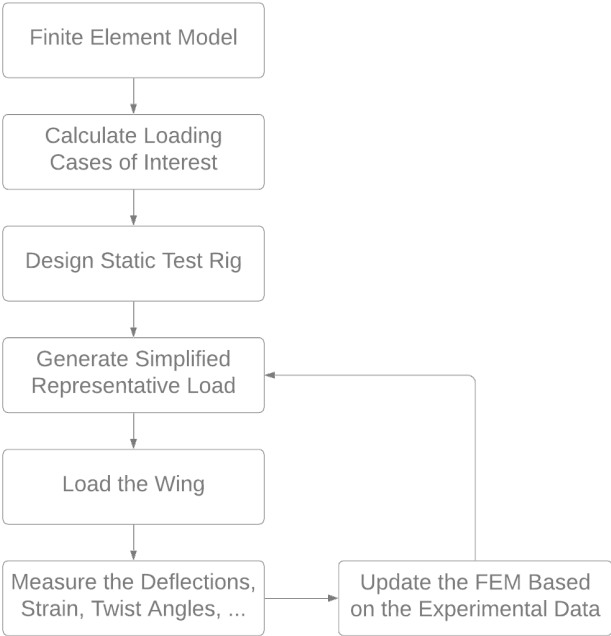
Figure 2.2: Schematic of Ground Static Load Test Plan.

2.1.1 Test Strategy and Pre Testing

The plan path for the static load test approach starts with finding a good simplified representation of the load cases desired to simulate and study. Location of suspension and boundary conditions need to be identified to optimize the test and the set of response Degree of Freedom (DOF) to be measured. A computational simulation is advisable to obtain pre testing expected results. With this information available it is time to proceed for the static test rig design that needs to be capable of fulfil requirements.

2.1.1.1 Calculations of Load Cases

The designing of a structure takes into account the ability to support ultimate loads without collapse and limit loads without permanent deformation when unloading. For example, the usual values for

transport category airplanes limit load factors are between -1g and +2.5g [11] and for normal category airplanes, from -1.52g to +3.8g [12].

Proof load, P_{load}, is defined by the equation below.

$$P_{load} = L_{load} \times P_{factor} \tag{2.1}$$

Where:

- L_{load} is the limit load;

- P_{factor} is the proof factor, generally taken as 1.0 for civil aircraft.

Ultimate load U_{load} is defined by the following equation.

$$U_{load} = L_{load} \times U_{factor} \tag{2.2}$$

Where U_{factor} is the ultimate factor normally assumed 1.5 for civil aircraft [13].

A proof test on the aircraft is mandatory before the first flight but, an ultimate load test is done later on because in most of the cases only one structure exists. Since this type of tests are more probable to failure, the structure requires a preliminary meticulous analysis to make sure the ultimate loads can be applied without damaged.

2.1.1.2 Design of Static Rig

After choosing the type of load to apply it's time for rig design where there is a need to build a jig taking into account the boundary conditions necessary for the experience, mass bags and any other required equipment.

From the later 1960s and 1970s, the advantages of dynamic sub-structuring and component-mode synthesis became a fundamental research topic in the field of structural dynamics. In the 1980s, coupling techniques excited the experimental community, due to the development of tests equipment. Thereby, the boundary conditions among substructures started to become very important when using component mode synthesis for structural dynamic analysis and model updating. When talking about "modes" here, it includes all structural modes from the exact eigenmodes, approximate modes, static modes, interface modes, etc [14].

Regarding the coupling method used, there are two conditions that should be respected.

1. Compatibility of substructures' displacements at the interface.

2. Force equilibrium on the substructures' interface DOF.

These boundary conditions chosen and applied in the experimental tests needs to be the same as on the FEM analysis.

Next step will be performing the loading and measure the deflections, strains, twist angles or others, depending on the main purpose of the study.

2.1.2 Data Acquisition System

The innovative part of static ground testing is on the method used to get the experimental data with high levels of accuracy when measuring the displacements. This data is the final answer of the work and since it needs to be precise there are already a number of technologies and solutions behind it being developed and tested.

Visual Image Correlation (VIC) is one of the techniques to measure the displacements and local deformation which started in the early 1950s comparing analogue representations of photographs [15]. Nowadays, it consists in a non-contact stereo-image to capture full-field displacement with a system that uses stereo triangulation to digitize a random speckling pattern placed on an object, and thus compute its three-dimensional features. It was already investigated in aircraft sector by Wu, Ifju, Albertani and Stanford *et al.* [16] [17].

Photogrammetry study started around 1850 and it was divided in four different phases where an advance in the mathematical component is noticeable [18]. They are nominated as plane photogrammetry (1850–1900), analogue photogrammetry (1900–1950), analytical photogrammetry (1950– 1985) and digital photogrammetry (1985–present). This concept also consists in getting precise measurements from photographs of an object and it has been recently used to perform Three Dimensional (3D) digitizing of tests objects for testing applications [19]. The process is similar to VIC and consists in two or more cameras to get spacial motion. There are two systems to locate the measurement points, a camera photogrammetry system and a photogrammetric digitizer. Photogrammetry usage to measure displacement on wings was already performed earlier by Galvao [20], Jacob[21] and Fleming [22].

The method used in this thesis work to get the displacements during the wing static loading ground tests was a metrology 3-dimensional scanning method in different load cases using a grade optical Co-ordinate Measuring Machine (CMM). It results in high accuracy results, in the same order as photogrammetry but with a simpler tool. There are recent studies with this technology applied to measurements on aircraft testing used by Nuno [23], Francisco [24] and Stephen [25]. For the surface scanning it was used the Creaform Metrascan 750, an externally referenced optical CMM, manually controlled. It uses infrared light emitted and observed from the C-Track base station to monitor the position and orientation of the hand-held scanning unit to about 25 μm accuracy. The hand-held unit uses class 2 red lasers with a red filter over greyscale stereo cameras to map and measure the surface for a total accuracy of 78 μm in a 16.6 m^3 envelope.

For the deformation analysis it was used the Creaform Handyscan 700, an internally referenced scanner that relies upon the use of reflective fiducial markers with a 6mm diameter to triangulate its position in space relative to the subject. It is essentially a combination of the Metrascan and C-Track, infrared emitters are used to allow the cameras to see the trackers, with the same class 2 laser array. This system is accurate to 43 μm per cubic meter. This manually controlled device builds a 3-dimensional geometry of the wing in different load cases with the same coordinate reference system. The reference coordinate system needs to be somewhere on the jig or on the floor to not interfere with the deformation measurement of the wing when load is applied. Captures and more information of this system can be

seen in section 4.2 of this thesis.

There are more technologies developed to measure the deformations or the modes, such as projected dot videogrammetry or laser doppler vibrometer. The reader can find more information in Simões [23].

2.2 Modal Analysis

For better understanding the vibration characteristics of mechanical structures there is a need to resort to modal analysis. It makes the analysis process easier when converting an utterly bewildering vibration signal of excitation and responses measurements into a simple set of parameters clear to visualize.

Structure vibrate or deform in a precise mode shape when excited at their natural frequencies. Beneath normal operation conditions, a structure will vibrate in a complex combination that is an overlay of all the mode shapes together. Recognizing each of them, it is possible to understand all types of vibration [26].

In a nutshell, this concept of Modal Analysis is in practice the identification of natural frequencies, damping ratios and mode shapes of a structure coming out of Frequency Response Functions (FRFs) measurements [27].

For example, if the structure is excited at its first natural frequency, the first mode shape will be visible. If it is excited at second natural frequency, the second mode shape will appear. But if the excitation frequency is in between natural frequencies, the deformation shape will be a combination of the two mode shapes closer to that frequency. It is expected to have more node points as the frequency of the mode shape goes higher. Node points are points along a standing vibration wave where the amplitude is zero, the exact opposite of anti node points where the amplitude is maximum. Between two node there is always an anti node [28].

Although real structures are Multiple Degree of Freedom (MDOF) systems and have some degree of non-linearity, they can commonly be estimated as a superposition of Single Degree of Freedom (SDOF) linear models. Non linear modal analysis of a full scaled aircraft was already done by Peeters *et al.* [27] because there were bolted joints on the aircraft that induced a non-linear behaviour. In their works, it is visible that these non-linearities haven't affected significantly the modes. Peeters and Kerschen in [29] state that non-linearities of the structure are mainly stiffness non-linearities and the effect of these on normal modes is similar to those caused by a static preload that has pre-deformed the structure. Carregado [30] also performed a non linearity study on a flexible wing aircraft and states that stiffness non linearities induced by structural deformations are not significant at small deformations. A static loading test is presented on section 4 where it is visible that the deflections were small and there was no deformation on the wing when unloaded.

2.2.1 Eigenvalues and Eigenvectors

2.2.1.1 Undamped System

In general, modal analysis begins with the calculation of an undamped case. The eigenvectors of this system can be called normal modes, where all the points move in phase or phase opposition. Not taking into account the damping matrix and in a free vibrating system, Newton's equation can be simplified as:

$$[M]\{u^{''}(t)\} + [K]\{u(t)\} = 0 \tag{2.3}$$

Where:

- $[M]$ is the mass matrix;

- $[K]$ is the stiffness matrix;

- $\{u^{''}(t)\}$ corresponds to the second derivative of $\{u(t)\}$, being $\{u(t)\}$ the vector of displacements.

The poles of each mode are found using the expression below, demonstrated by Brandt [31].

$$s_R = \pm\sqrt{-\lambda_R} = \pm j\sqrt{\lambda_R} \tag{2.4}$$

Where the undamped natural frequencies can be obtained by the relation $s_R = j\omega_R$, where the subscript R represents the vibration mode.

2.2.1.2 General Damping

When analysing a general damped case, the complete Newton's equation will be considered.

$$[M]\{u^{''}(t)\} + [C]\{u^{'}(t)\} + [K]\{u(t)\} = \{f(t)\} \tag{2.5}$$

Where:

- $[C]$ is the damping matrix;

- $\{f\}$ is the vector of externally applied forces;

- $\{u^{'}(t)\}$ corresponds to the first derivative of $\{u(t)\}$.

From this point on, the nomenclature denoting time dependence will be dropped for brevity.
Re-writing the system in state space form results in the equation:

$$\begin{bmatrix} C & M \\ M & 0 \end{bmatrix} \begin{Bmatrix} u' \\ u'' \end{Bmatrix} + \begin{bmatrix} K & 0 \\ 0 & -M \end{bmatrix} \begin{Bmatrix} u \\ u' \end{Bmatrix} = \begin{Bmatrix} F \\ 0 \end{Bmatrix} \tag{2.6}$$

Simplified as:

$$Ax' + Bx = F \tag{2.7}$$

Where:

$$A = \begin{bmatrix} C & M \\ M & 0 \end{bmatrix} \tag{2.8}$$

$$B = \begin{bmatrix} K & 0 \\ 0 & -M \end{bmatrix} \tag{2.9}$$

$$F = \begin{Bmatrix} \mathsf{F} \\ \mathsf{0} \end{Bmatrix} \tag{2.10}$$

$$\begin{cases} x = [u^T u'^T]^T \\ x' = [u'^T u''^T]^T \end{cases} \tag{2.11}$$

where the superscript T represents the transpose vector.

From equation 2.7 a first order differential equation may be recognized and a generalized family of solutions exists of the form,

$$x = \phi e^{\omega t} = \begin{Bmatrix} \phi \\ \lambda \phi \end{Bmatrix} e^{\omega t} \tag{2.12}$$

If equation 2.7 is equalled to zero, the free vibrations of the system may be solved and applying the Laplace Transform results in:

$$|sA + B|X(s) = 0 \tag{2.13}$$

Multiplying A^{-1} through equation 2.13 and $s = -\lambda$ it is possible to solve the eigensystem.

This will lead to 2N eigenvalues and eigenvectors. However, the solutions will either be real or conjugate poles leading to N eigenvalue and eigenvectors. Looking at the root locus of the solutions, a real eigenvalue represents a system with an overdamped pole. This, the study of free vibrations is the case when modes come in complex conjugate pairs [30]. To represent each mode, the second pole from the pair is considered with the positive imaginary part being written as:

$$s_R = -\zeta_R \omega_R + j\omega_R \sqrt{1 - \zeta_R^2} \tag{2.14}$$

Where ζ_R is the damping coefficient and the angular frequency ω_R is often presented in terms of cycles as $f_R = \frac{\omega_R}{2\pi}$. Each natural frequency is associated to a specific mode and represents a frequency at which the structure resonates [31].

2.2.1.3 Numerical Computations

In order to predict the vibration characteristics of a structure, dynamic analysis using the finite element method is performed. During the experimental work, these analysis were done with *Ansys* soft-

ware. Even though it is not the objective of this work, it was made with the purpose of having modal parameters predictions before the wing vibration testing. The results can be visible on section 3.4. When doing computational analysis, the structure is represented by a compilation of springs and masses that converges in a set of matrix equations that represents the structure behaviour [26].

Modern commercial Finite Element Analysis (FEA) packages, like *Ansys* and *FEMTools*, generally offer a number of solution methods for modal extraction including but not limited to Givens, Modified Givens, Householder, Modified Householder, Inverse Power, Sturm, and Lanczos. Lanczos method is a very efficient algorithm to perform a modal analysis for large models, it is a fast and robust algorithm and used for most applications as the default solver. In 1970, Ojalvo and Newman [32] publish the first paper proposing a practical reduction scheme for large eigenvalue problems based upon the use of Lanczos vectors. Latest versions of this method were explored later by various authors with modifications and improvements and apart being an old method, it is still the most universal method in eigenvalue extraction of FEM for large model with a large number of DOF, such as used in this study. This reduces solution time considerably.

There are also some other common methods but they have disadvantages comparing to the use of Lanczos method, like the Inverse Power Method [33] that does not allow the determination of a specific number and range of eigenvalues and eigenvectors or Supernode Eigensolver [34] that is not advantageous when a low number of modes is requested.

2.3   Ground Vibration Testing

Dynamic Aeroelasticity results from the coupling between elastic and inertia forces and considers the oscillatory effect of forces applied on a structure. One interest of the study of the dynamic behaviour of a structure is the prediction of occurrence of the tragic phenomenon called flutter. It's an instability derived by the a combination of the three forces presented on the figure 2.1 that involve two or more modes of vibration and prove that the structure can definitely extract energy from the airstream [10].

To assure no adverse dynamics behaviour like aeroelastic and aero-servo-elastic instability occurs, Experimental Modal Analysis (EMA), more specifically GVT, is performed. GVT is the experimental measurement of an aircraft structural vibration modes including peak frequencies, damping and mode shapes. Apart from the flutter identification, it also has good results on detection of structural flaws, and identification of flight control dynamic problems. Since it is an expensive method and it takes significant time to perform and analyse, there is constant economic interest in improvements to minimize its costs and time consumption without compromising results. This has motivated a lot of international research [35] [36] [37]. There are also more recent methods being studied for different approaches and different types of aircraft [25] [38] [39].

GVT, as most of experimental works, has specific methods, instruments, tools and data acquisition interfaces. Along the next sections, a brief explanation of some theoretical concepts is presented as well as the details for the tests done. Abundant options are available on the market for this kind of experiment and the final choice takes into account the purpose of the study and the budget for the experiment.

2.3.1 Frequency Response Function

The Transfer Function (TF) is a mathematical model representing the relationship between two signals, the excitation (input) and the response (output) of a physical system. Can be defined as:

$$H(s) = \frac{Y(s)}{X(s)} \tag{2.15}$$

Where:

- $Y(s)$ is the Laplace transform of the output;

- $X(s)$ is the Laplace transform of the input.

The FRF, used on the EMA along this document is mathematically the Fourier transform of the output divided by the Fourier transform of the input. Due to the similarity in the terminology most of the times they are used as the same and creates some source of confusion. FRFs are obtained by evaluating the imaginary axis of the Laplace domain where $s = j\omega$. The frequencies at which the structure vibrates freely are obtained from the poles of the TF.

$H(f)$ is a FRF matrix which contains all the receptance frequency responses for the system, that is to say for all the individual inputs q, and output responses p. A modal superposition equation can be written as every mode's residues divided by the complex conjugate poles of the system, for a particular mode [31].

The expression in Transfer Function (TF) form is visible on the equation 2.16 and as a FRF on the equation 2.17.

$$H_{pq}(s) = \sum_{r=1}^{N} \frac{A_{pq,r}}{s - s_r} + \frac{A_{pq,r}^*}{s - s_r^*} \tag{2.16}$$

$$H_{pq}(j\omega) = \sum_{r=1}^{N} \frac{A_{pq,r}}{\omega_r \zeta_r + j(\omega - \omega_r \sqrt{1 - \zeta_r^2})} + \frac{A_{pq,r}^*}{\omega_r \zeta_r + j(\omega + \omega_r \sqrt{1 - \zeta_r^2})} \tag{2.17}$$

Where:

- $A_{pq,r}$ and the complex conjugate $A_{pq,r}^*$ are the residues;

- ω_r and ζ_r are the frequency and damping for a particular mode r.

The advantage of FRF compared to TF is that it can be experimentally measured.The acceleration response of the structure is measured relative to the force excitation from the impact hammer in the time domain but it can be transformed into frequency domain using the Fast Fourier Transform (FFT),first published by Cooley and Tukey [40] in 1965, on the excitation and response measurement, visible in figure 2.3 and 2.4.

The signals obtained are analog sources, require sampling and quantization to get accurate sampled signals before passing through a FFT. Nyquist-Shannon sampling theorem, states that sample period must be at least half that of the signal of interest. A low pass filter should be applied to prevent signals with frequencies higher than half the sample rate from being misconstrued as lower frequencies.
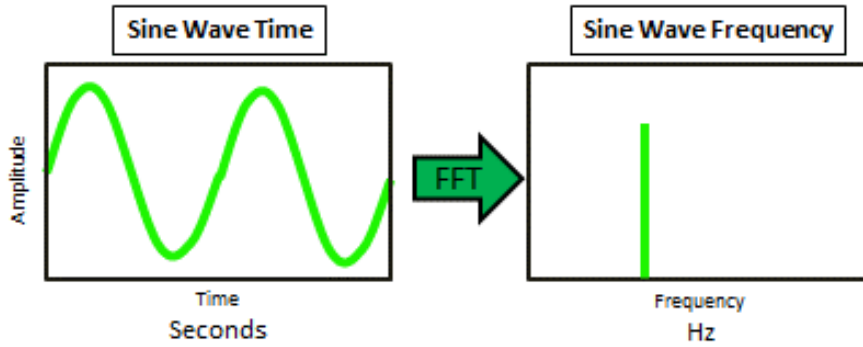
Figure 2.3: Response: Laplace domain vs Fourier domain [41].
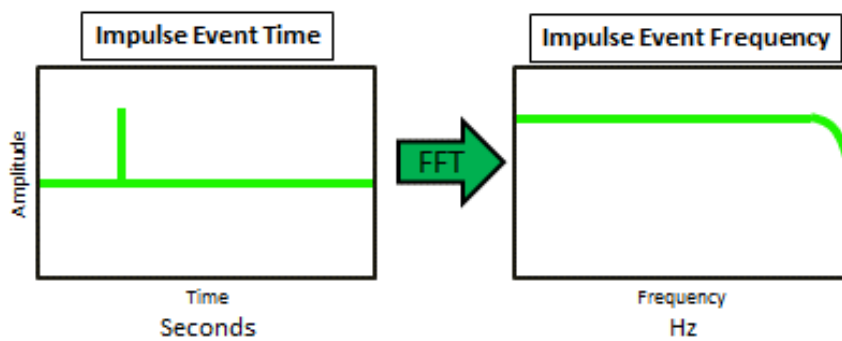
Figure 2.4: Excitation: Laplace domain vs Fourier domain [41].

There is a phenomenon that deserves attention called leakage. It happens when a signal is aperiodic and incorrect estimates of frequency and amplitude will result. In order to solve this possible problem, averaging, increasing frequency resolution, use periodic excitation and the use of time domain windowing functions are good and already studied approaches.

In impact testing, the signals are usually transient and because of that, the signal should not present signs of leakage, rendering the use of a window filter unnecessary.

Measured in a complex signal with either Magnitude/Phase or Real/Imaginary, FRFs are expressed in a Bode Diagram format like the one in the figure 2.5. Magnitude represents the ratio of the input force to the response, for example in g/N. The phase diagram is expressed in degree and indicates whether the response moves in and out of phase with the input.

Any function that has amplitude and phase can also be transformed to real and imaginary terms, as described in the equations below and visible on the figure 2.5.

$$Amplitude = \sqrt{Imag^2 + Real^2} \qquad (2.18)$$

$$Phase = tan^{-1}\left(\frac{Imag}{Real}\right) \qquad (2.19)$$

It is expected to have the real part of the FRF equal zero at natural/resonant frequencies and the
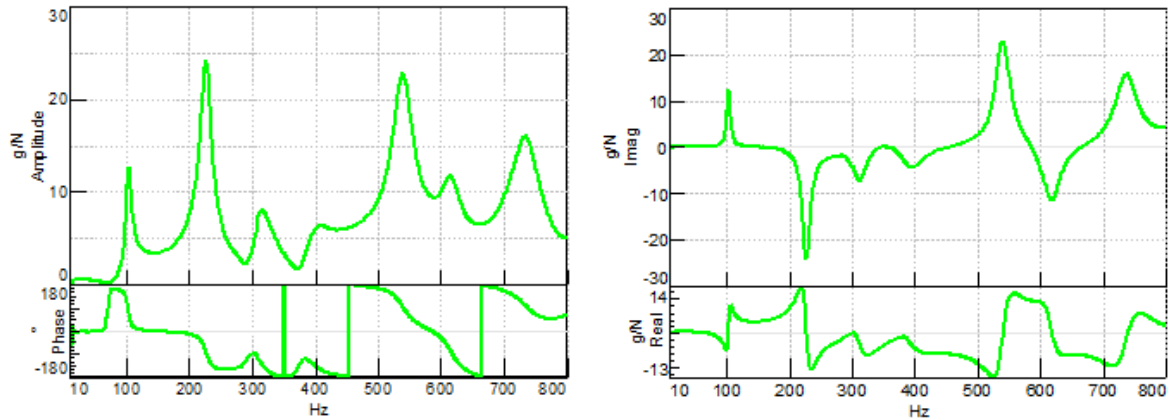
Figure 2.5: Bode Diagram: Left - FRF expressed in Amplitude and Phase, Right - FRF expressed in Real and Imaginary [42].

imaginary with peaks either above or below zero which indicate resonant frequencies. If more than one FRF is acquired at different locations on the structure and they are all phased with respect to a common reference, the imaginary part, taking into account the direction of the peaks, can be used to plot the mode shape.

In order to have reliable results, depending on the structure and how hard it is to get a good measurement, a specific number of impacts at the same point needs to be done. The purpose of this approach is to have a coherence graphic used to assess the quality of measurements displaying the average similarity level between the impacts and the FRFs. An example is presented on the figure 2.6. Coherence tells what portion of the response is attributed to the excitation. 1 would be the desirable value if the impacts were exactly the same and 0 would represent no similarity between impacts, which is a possible warning flag that there is an error in the measurement setup. Since this is a experimental work and perfect conditions are impossible to obtain, it is considered very good results when this plot presents values of coherence higher than 0.9 around natural frequencies. However, this value can be close to 0 at anti-resonant frequencies where the vibration and responses are small and their repeatability is made inconsistent by the noise floor of the instrumentation. This errors can occur due to instrumentation errors, inconsistent excitation or insufficient force and although it have not happened for the structure in study, it is normal and acceptable when the coherence is high around the points of interest [26][42].

2.3.2 Excitation Methods

For the vibration response studies, in general, an excitation source is a way to transfer energy to a test structure. It requires external motion to be induced in the form of stimulus. For a EMA on a mechanical structure, typically the input is force and output is acceleration, velocity or displacement.

Accordingly to the past researches related with this theory, there are two main types of excitations, implying a direct contact within the structure and an external source, denominated as impact testing and shaker testing. In theory, there is no difference between the type of results coming out of impact testing or shaker testing, they have exactly the same input and output characteristics.

16
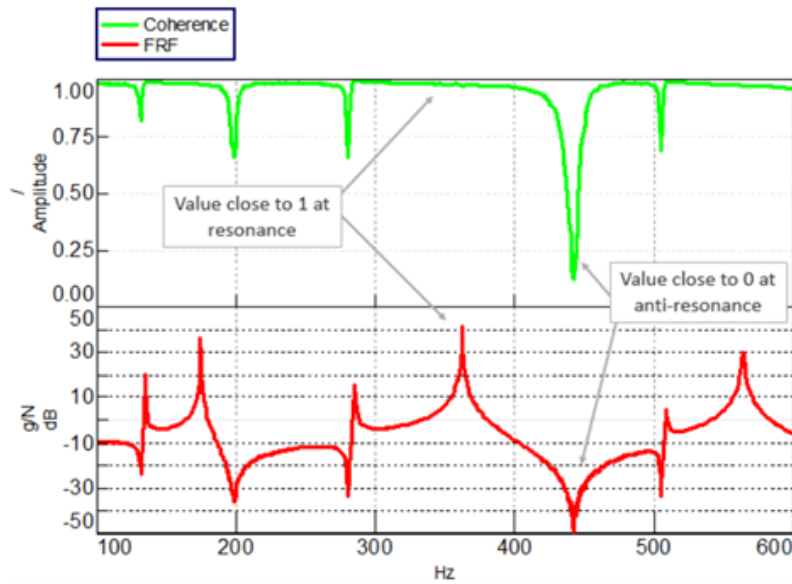
Figure 2.6: Coherence (Green) and FRF (red) relationship [42].

2.3.2.1 Impact Testing

The most straightforward approach to obtain FRFs consists in directly hit the structure with an impact hammer. This procedure is called Impact testing. Impacts are performed by a technician and should be as close as possible to a Dirac delta. The results may vary depending on skills and expertise of the operator and the objective is to get narrow pulse impacts to get higher frequencies in the input spectrum, perpendicular to the surface of the structure, low sharp, single peak and, similar as possible along time and different points, even tough they are normalized [30].

Since this is a skill that improves with experience, an improvement on impacts quality can be achieved by looking at coherence graphic, visible on data acquisition system, and trying to obtain values close to 1. An explanation of coherence is more detailed on section 2.3.3.

The impact hammer used is characterized by having an embedded impedance head that measures the force applied at the tip of the hammer. This tip can be from different materials with hardness levels. It is responsibility of the technician to choose the tip adequate to the material of the structure, as well as the intensity of the impact. Increasing the stiffness of the tip shortens the duration that the hammer is in contact with the structure. Despite this, most of the times it is easier to define which tip suits the best trying and looking at the FRF and learn by doing. For example, if the FRF becomes noisy at higher frequencies and the input spectrum drops off significantly, it is an indication that our hammer tip may be too soft [41].

In a lower level of complexity it is important to highlight that only a hammer and one accelerometer is enough to establish a TF within the response and excitation source at a specific DOF.

In figure 2.7 it is possible to see an example of an impact hammer, a structure with possible measurement locations and the accelerometers used to measure the responses.

While an impact is being done, there are high sensitive accelerometers well distributed along the wing to measure the response to the excitation.
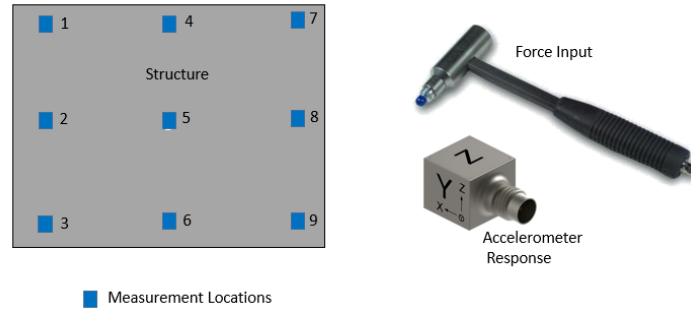
Figure 2.7: Example of a GVT test equipment [43].

2.3.2.2 Impact Testing vs Shaker Testing

In this study, shaker testing was deemed unworthy to perform. Analysing some details such as, setup duration, setup complexity, test duration, acquisition and control, it is visible that an impact test is much more convenient. It can be easily performed because it is quicker to mount the setup, due to the small complexity of it, and the acquisition and control is way simpler, although it takes longer to perform the tests. In fact, the only advantage of a shaker testing is that it gives the user an accurate control over the inputs. However, a problem called mass loading can appear while shaker testing. Mass loading is basically a phenomenon where the mass of the devices used to measured the responses affects the vibrations of the structure [31].

When using shakers to excitate the structure, these are fixed to a specific point on the structure and can not be moved due to complex installation. This means that, since it is impossible to have roving excitation, it is mandatory to rove the accelerometers. This constant repositioning of the accelerometers can change the rest position and mass loading of the structure. Finally, this specific structure is a stiff wing with very low flexibility. Thus, good results can be achieved with impact tests making the shaker test unnecessary. Even more when the instrumentation needs to be rented, affecting significantly the budget for testing [23].

2.3.2.3 Roving Hammer vs Roving Accelerometer

In order to restrain the budget, since all the precise instruments are extremely expensive, roving tests are a good option. Either roving the excitation source or the transducers that measure the responses around the structure means that a SDOF (one accelerometer) is enough to get the correct dynamics results.

Maxwell's reciprocity applied to modal testing states that it does not matter if there is a fixed reference with roving excitation or fixed excitation with roving response sensors. The results will be the same impacting at point 'a' and measuring the response at point 'b' or vice versa [23].

As can be observed in figure 2.8 two options can be considered:

1. Roving hammer means that a single or multiple response/s DOF is/are fixed and the excitation is roving around test points.

2. Roving accelerometer means that the excitation source will be always in the same point and every time there is an impact, the measuring sensor moves to other test point.

(a) Roving hammer method   (b) Roving accelerometer method
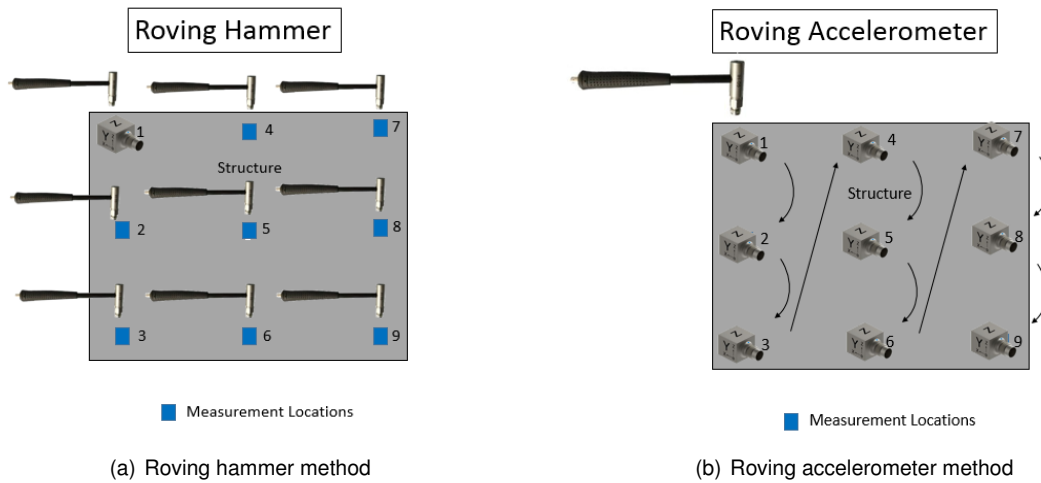
Figure 2.8: Roving hammer vs Roving accelerometer [43]

In order to avoid the mass loading effect and the need of always move the transducers around the structure once they are glued, it becomes unpractical to perform a roving accelerometer. Also, in case of a surface with high quality finishing, it can result in damage. Because of these advantages, the roving hammer method was used.

2.3.3 Data Acquisition System

Data acquisition was accomplished using National Instruments NI cDAQ-9188 with IEPE NI 9234 acquisition cards to connect the accelerometers and the impact hammer. Conversion and amplification of analogue signals into digital systems is responsibility of *LabVIEW* software that stores in the system's memory one data block for each measured DOF impacted. The digital signals are input a process that calculates the FRF matrix for multiple input multiple output systems, based on a built in FFT algorithm. Dealing with this FFT-based system, Nyquist criterion needs to be satisfied in order to prevent false frequencies in their frequency spectre [44]. No windowing was applied to the data prior to estimating the FRF as signal was pre-sampled prior to excitation and structural damping allowed signal to decay sufficiently during acquisition time. Graphical user interfaces of *Labview* software used to record the data information, with coherence and FRF magnitude and phase graphics available that can be visible on figure A.1.

After recording, the data is pre-processed on a *Matlab* script adapted by the author of this document and based on a similar work developed by Simões and Warwick [23][25], which the target is to format the files obtained from the tests into a Universal File Format 58 (UFF58) capable to be read by *MEScope*, the software used for the curve-fitting analysis.

19

2.3.4 Test Strategy and Pre testing

The first aspect to take into account when thinking about the test setup is designing the support jig. This structure can not interfere with the desired results. During the development of the jig, it is important to perform a computational modal analysis to make sure the natural frequencies are in a different range of the ones expected for the structure.

Defining the impact points as equally spaced, creating a mesh with a resolution high enough to avoid having points overlapping node positions is important.

The number of accelerometers placed along the structure is difficult to define. Although the engineer is looking for measures in as many points as possible, the high number of response DOF increases the testing and post processing times. Due to high sensitivity of this instruments, they are expensive and limited in number, which means simplifications on the distribution of accelerometers along the structure need to be detailed studies. Another problem that can occur is a phenomenon called mass loading [31] where the mass of the accelerometer (even though they are light) can affect the dynamic stiffness, thus affecting the test and consequently, the characteristics to be determined. Finally, for the post processing of the data, it would lead to undesirable higher complexity and longer computation times.

In order to have a good simplification when choosing the accelerometers placement, a special attention goes to avoiding the node points. If by mistake an accelerometer is glued on a nodal point, no information is recorded since the magnitude at that point is nearly zero. To help finding the optimal locations for placing measurement sensors on the structure which best capture all the mode shapes considered, it was resorted to a pretest planning method functionality of *FEMtools* software called Sensor Elimination Algorithm by Modal Assurance Criterion (SEAMAC). It uses an iterative procedure to eliminate DOFs that result in the smallest modal assurance criterion degradation in terms of largest out-of-diagonal term (spatial aliasing). This procedure can be very time-consuming when there are many candidate DOFs [45]. It is therefore recommended to reduce the number of candidate DOFs to as low as acceptable. Optimum single reference DOF is the one that is not a nodal point for any of the modes of interest.

While this is a computational method based on the FEM mode shapes imported *a priori* to the software, experimental mode shapes can be different from those. Accordingly, this method can hide some errors so it is advisable to use more than one accelerometer for redundancy purpose.

Always keep everything organized, tapping the cables and being careful with instruments is fundamental to protect not only the people but also the equipment. Due to high sensitivity of the instruments is necessary to find a calm and quite place for the tests because any type of movement or sound can be detected and will introduce in errors on the measurements.

2.3.5 Modal Parameters Extraction and Analysis

The content of this section consists in the procedures to extract some modal parameters, namely measuring the modal frequencies by inspection of FRFs, determining the modal damping with the aid of a frequency weighting function included in the analyser, and establishing the mode shapes by examining

the value of the imaginary part of the FRF [46].

The first stage in determining the dynamic behaviour of a structure is to evaluate these parameters with the help of calculations after curve-fitting procedures.

In summary, the modal parameters extraction can be done in a sequence of identifying the normal modes followed by least-squared curve-fit to get the natural frequencies and modal damping values and finishing with a refined curve-fit to determine the mode shapes [30].

2.3.5.1 Curve Fitting

Curve fitting is a data reduction process that converts the dynamic information from a set of FRFs into a set of modal parameters.

The software used for curve-fitting is called *MEScope* and has an available recommended path to perform the task.

Firstly, to visualize the reliability of the acquired data, it should be observed the Operational Deflection Shapes (ODSs) in animation (the forced response deflection shapes) on the 3D model of the structure directly from its FRFs.

Defining the mode indicator function is the next step and there are two available.

- Complex Mode Indicator Function (CMIF) [47];

- Multivariate Mode Indicator Function (MMIF) [48].

The following steps are to fit a mathematical function that results from a least-squared approximations between the analytical function and measured data. Again, there are options to choose and three methods can be used.

- Local Polynomial which estimates modal parameters one mode at a time;

- Global Polynomial which can simultaneously estimate parameters for two or more modes at a time.

- Stability Criteria that is used for specific applications.

Lastly, a more refined curve fit will provide the mode residues in order to find the mode shapes.

In this study a quick fit command was used that applies all three modal curve fitting steps in sequence to a set of FRFs, using a polynomial method [49].

2.3.5.2 Modal Parameters Estimation

The natural frequency is the easiest modal parameter to determine. A natural frequency is identified as a peak in the magnitude of the FRF, as shown on the figure 2.9.

The most common method of determining the damping at a natural frequency, is to identify the half power points, 3 dB down from peak value, of the magnitude of the FRF. The wider the peak, the heavier the damping. Damping ratio, ζ_R, can be written as:

$$\zeta_R = \frac{\Delta f}{2 f_R} \tag{2.20}$$
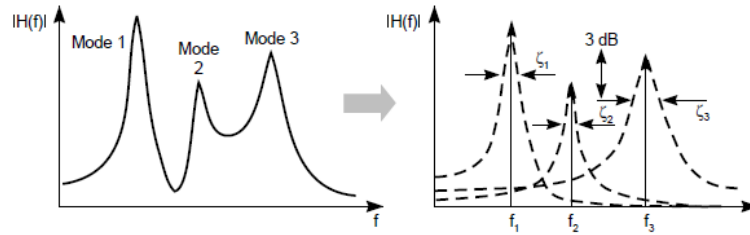
Figure 2.9: Method for extraction of Resonant Frequencies and Damping from a FRF..[46].

Where:

• Δf is the frequency bandwidth between the two half power points;

• f_R is the natural frequency.

Quadrature Picking is based on the assumption that the coupling between the modes is light and it is the simplest way to find the mode shapes. The value of the imaginary part of the FRFs at natural frquency, is proportional to the modal displacement. Therefore, by examining the magnitude of the imaginary part of the FRFs at a number of points on the structure, the relative modal displacement at each point is visible [46]. From these displacements, the mode shapes can be obtained, as can be seen on the figure 2.10.
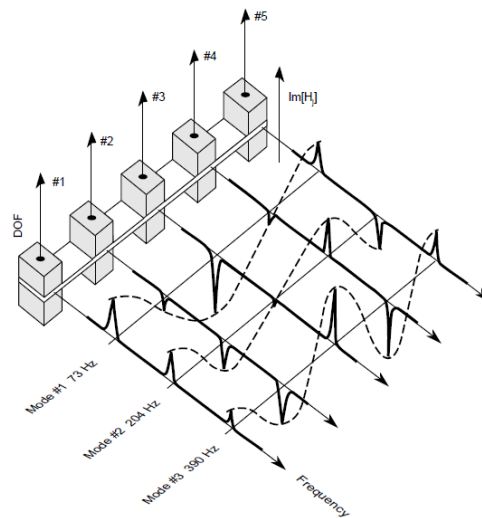
Figure 2.10: Method for extraction of Mode Shapes from Imaginary part of a FRF.[46].

2.4   Finite Element Model Updating

Regarding the analysis of the dynamics of a structure, Newton's Second law stated that it always converges on the use of second-order differential equations 2.5 [50][51].

These coefficient matrices contain constants that represent the properties of the DOF included in the model of the structure. It is the purpose of model updating to study how modifications of the design

22

variables will influence the system's response and how an error function that describes the deviation between analytical and experimental data, can be minimized. This is best achieved starting with a manual mass updating followed by sequentially validating and updating of modeling of mass, stiffness and damping using data from static and dynamic testing. Finally, when modeling errors can be excluded, experimental operational responses are used to identify dynamic forces. In order to have access to all of this constants presented in the equation 2.5 with the objective of planning the FEM update approach, the optimal sequence is presented on the figure 2.11.
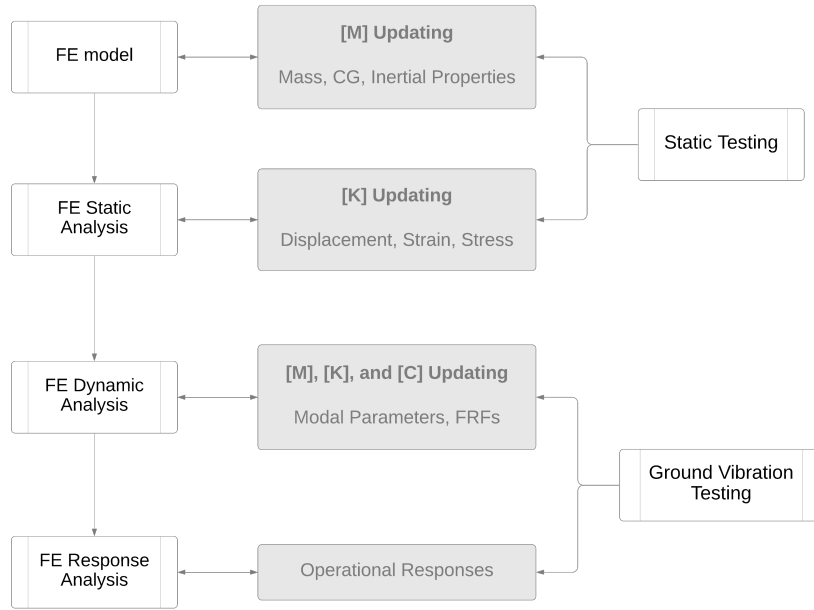
Figure 2.11: Optimal Updating Sequence.

Reliability of a finite element model is only achieved with real information and with that data, the model will be validated and verified. For flutter calculations, the FEM needs to be accurate and representing the reality with high fidelity. When analysing a complex non-linear structure, as in this study case, there are some problems, such as manufacturing weight differences, faulty boundary conditions definition, incorrect assumptions of the material properties or difficulty in modelling shapes and joints. The long process of model updating ensures the quality of the matching between the real and numerical data [38]. The schematic of the FEM updating for each process, static and dynamic is similar and presented on the figure 2.12.

2.4.1 Sensitivity Analysis

In order to update a finite element model with success, the main objective of the work is to minimize the Correlation Coefficients (CC) of the chosen parameter to update. A sensitivity based parameter estimation is the first step to choose what characteristics should be analysed. The relationship between the structural parameters, represented by a reference system responses vector $\{R_e\}$ with the experimental data, and the modal characteristics, represented by a predicted system responses vector $\{R_a\}$ for a given state of the parameter values $\{P_0\}$, can be expressed in terms of a Taylor series expansion

Figure 2.12: Schematic of Model Updating iterative loop [52].

limited to the linear term.
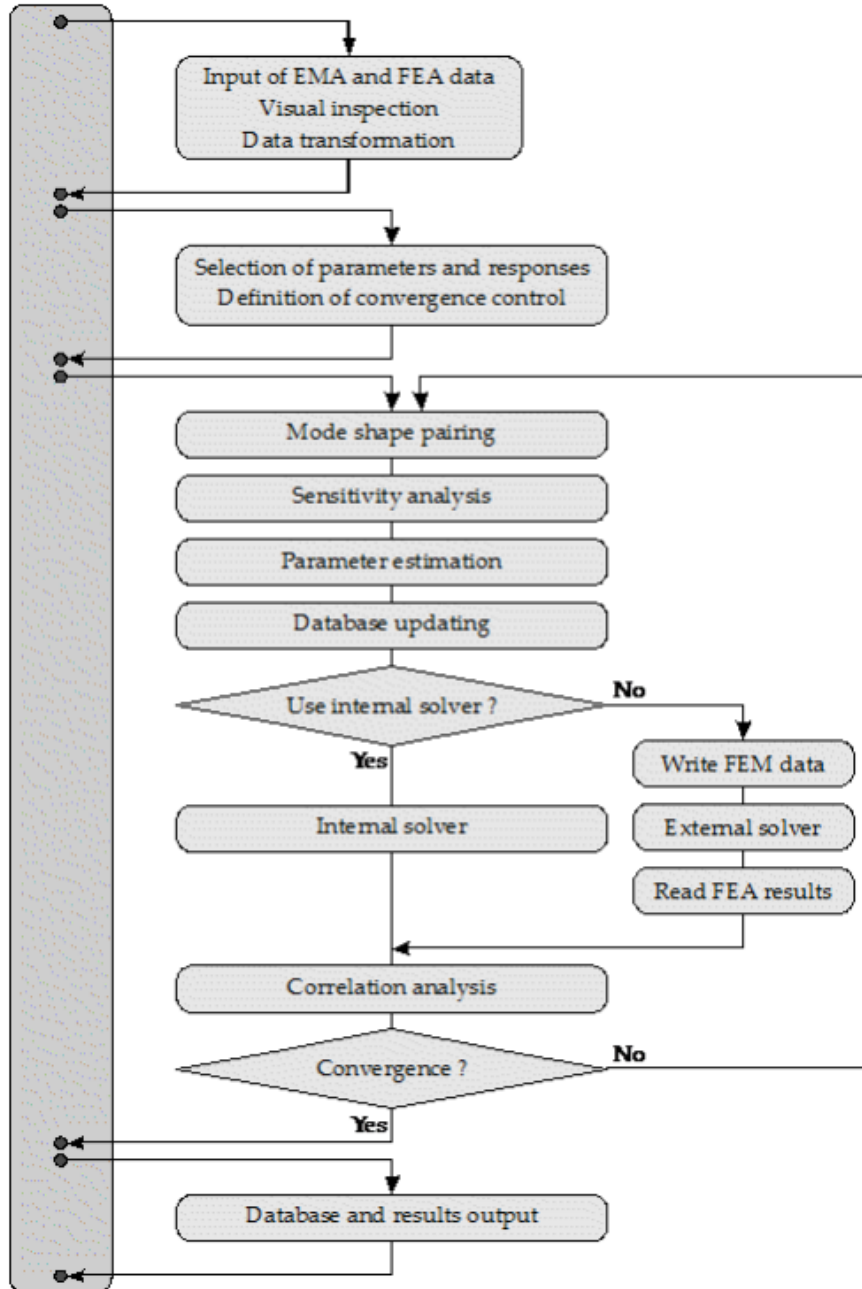
$${R_e} = {R_a} + [S]({P_u} - {P_0})$$ (2.21)

or

$${\Delta R} = [S]{\Delta P}$$ (2.22)

Where:

- ${P_0}$ is the vector composed by the selected parameter values for updating;

- $\{P_u\}$ is the vector of updated parameter values;

- $[S]$ the sensitivity matrix.

The equation 2.21 implies the pairing of the experimental responses with the analytical responses.

After a sensitivity analysis there are three parameter estimations methods. If the number of equations presented on equation 2.21 is the same as number of parameters, the parameter variation comes from inversion of the sensitivity matrix, called Pseudo-Inverse Parameter Estimation method. If the difference between the initial predictions and the experimental results is noticeable the Bayesian Parameter Estimation method is preferred. Weighted Least Squares Parameter Estimation method is used if the weighting matrix expressing the confidence in the model parameters equals zero, that means the experimental results has no confidence data and so, parameters are not updated.

The most appropriate method to the work developed here the Bayesian Parameter Estimation method because there were differences between the computational values and the experimental results. So, the sensitivity matrix [S] contains the gradients of reponse R with respect to paramenters P:

$$[S] = S_{ij} = \frac{\delta R_i}{\delta P_j} \tag{2.23}$$

The updated values of parameters P are obtained from equation 2.22 and 2.23:

$$\{P_u\} = \{P_0\} + [G](\{-\Delta R\}) \tag{2.24}$$

with the gain matrix [G] computed following Bayesian estimation theory as:

$$[G] = ([C_p] + [S]^t[C_R][S])^{-1}[S]^t[C_R] \tag{2.25}$$

Where:

- $[C_p]$ represents a weighting matrix expressing the confidence in the model parameters;

- $[C_R]$ is a weighting matrix expressing the confidence in the responses.

The reader can find more details about parameter estimation methods on the technical manual of the *FEMtools* software used in this work [52].

2.4.2 Convergence Criterion

A considerable number of CC can be computed to present the discrepancy between the numerical and experimental value of the responses with the *FEMtools* software:

- CCMEAN measuring the weighted relative difference between natural frequencies;

- CCABSOLUTE measuring the weighted absolute relative difference between natural frequencies;

- CCDISP measuring the weighted absolute relative difference between displacements;

- CCMASS measuring the weighted absolute relative difference between exact mass and calculated mass;

- CCMAC measuring the weighted difference between target and average actual Modal Assurance Criterion (MAC) or Pseudo-Orthogonality Check (POC) values;

- CCTOTAL measuring the total CC value that sums CCABS, CCMAC, CCDISP and CCMASS;

- MACMEAN is an additional CC that computes the weighted difference between target and actual MAC values.

To decide when the iterative process of parameters updating should stop, one of the tests presented below have to be satisfied. The CCs will be interpreted as an objective function that needs to be minimized.

The following criteria are used on *FEMtools* software and were also used on the development of the studies in this document [52]:

- The following reference value for the CC is simply an imposed margin:

$$CC_t < \epsilon_1 \tag{2.26}$$

Where:

  – CC_t is the reference CC at iteration t;

  – ϵ_1 is the first convergence margin chosen.

- Two consecutive values of the reference CC are within a chosen margin.

$$|CC_{t+1} - CC_t| < \epsilon_2 \tag{2.27}$$

Where:

  – CC_{t+1} is the reference CC at iteration t+1;

  – ϵ_2 is the second convergence margin chosen.

- The number of iterations is higher than the maximum defined limit allowed.

2.4.3 Based on Static Tests

When the objective is updating the stiffness, the error function that must be minimized is the difference between experimental and analytical static displacements, at the measured DOFs i, for a number of load cases j;

$$\{U_{ei}^j\} - \{U_{ea}^j\} = \frac{\partial(U_j)}{\partial p_k}(p_{ku} - p_{ko}) \tag{2.28}$$

where *a* stands for analytical, *e* for experimental, *u* for updated and *o* for originally estimated. From this equation, the updated parameter values p_{ku} can be easily obtained. The sensitivity coefficients are computed using a separate analysis.

Since the load force is invariable,

$$[K]\{\Delta U\} + [\Delta K](U + \Delta U) = 0 \tag{2.29}$$

When the different between displacements is known in all the points, the exact sensitivities can be computed with equation 2.29 and the exact updated parameters are obtained by solving the equation 2.28.

The process used on *FEMtools* software to perform the iterative model update of the stiffness matrix [K] is presented on the figure 2.13.
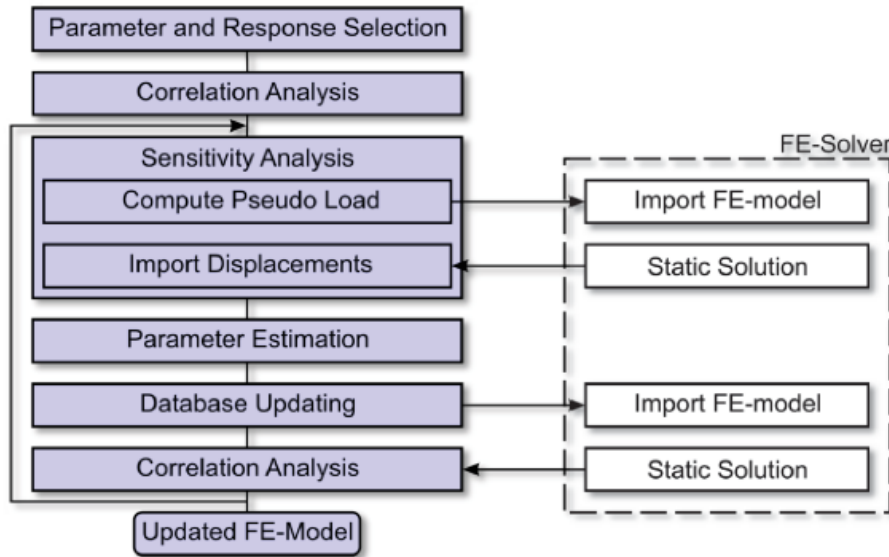
Figure 2.13: Schematic of Model Updating [52].

When performing the model updating using the static loading tests data, the CC used was the CCDISP because static data consists in measuring the displacements. This coefficient is the only one that measures the weighted absolute relative differences between displacements instead of natural frequencies that are not appropriate at this stage. Displacements can be operational or modal [52].

The CC CCDISP, for a particular DOF i, can be computed with:

$$CC = \frac{1}{C_R}\sum_{i=1}^{N} C_{R_i}\frac{|\Delta\psi_i|}{\psi_i} \quad \text{with} \quad C_R = \sum_{i=1}^{N} C_{R_i} \tag{2.30}$$

Where:

- N is the number of active displacement responses;

- C_R is the weighting matrix for the responses and C_{R_i} response confidences;

- ψ is the displacement or eigenvector of the system.

2.4.4 Based on GVT

After updating the stiffness based on static tests, the post processed results obtained from the GVT are important to proceed in the analysis and update of the mass and stiffness matrices.

This update can be based in modal parameters extracted from the post process data of the GVT or directly based on the FRFs obtained from the GVT [52].

The modal-based update can be performed using natural frequencies only or adding modal displacements, MAC or POC.

The MAC is a measure of the squared cosine of the angle between two mode shapes. To compute the difference between analytical (ψ_a) and experimental (ψ_e) mode shapes the equation 2.31 is used.

$$MAC(\psi_a, \psi_e) = \frac{\left|\left(\{\psi_a\}^T, \{\psi_e\}\right)\right|^2}{(\{\psi_a\}^T\{\psi_a\})(\{\psi_e\}^T\{\psi_e\})} \tag{2.31}$$

The most efficient CC to use in this case is the CCTOT since, as previously explained, it considers all the other CC, for example CCABS for the natural frequencies, CCMASS for the mass and CCMAC for the MAC, that are all important to analyze.

FRF-based is able to update the mass, stiffness and damping separately or combined using FRF amplitude differences or FRF correlation functions. This updating method was first introduced in 1994 [53] and has been adapted for implementation on FEMtools that solves the following equation:

$$[\alpha_A(\omega)][-\omega^2[\Delta M] + i\omega[\Delta D] + [\Delta K]][\alpha_X(\omega)] = [\alpha_A(\omega)] - [\alpha_X(\omega)] \tag{2.32}$$

Where:

- $\alpha_A(\omega)$ is the current analytical receptance matrix;

- $\alpha_X(\omega)$ is the measured receptance matrix;

- $[\Delta M]$, $[\Delta D]$ and $[\Delta K]$ are the mass, damping and stiffness matrices modification, correspondently;

- ω is the excitation frequency.

Femtools uses a new method to update mass, stiffness and damping of a finite element model resorting to FRF correlation functions Cross Signature Assurance Criterion (CSAC) and Cross Signature Scale Factor (CSF). More details of this functions can be found in the software's manual [52]. Using FRFs for the update have advantages because they are not subject to averaging and curve-fitting errors.

Chapter 3

Wing Finite Element Model

In order to perform pre testing static and vibration simulations, a FEM already developed by CfAR's engineers was used on this experimental work. The usage of FEMs is common and the standard tool for structural analysis. It allows engineers to have computational simulations that preliminary estimate the behaviour of a structure. These numerical methods have the advantage of being developed and tested before the manufacturing process and extremely useful for detecting possible errors and optimizing conditions that can be truly precious for time and money savings. Not only in aeronautical but all over the engineering fields, such as mechanical, biomedical, construction and so on.

Although real conditions can be simulated, FEM analysis does not provide complete information about the behaviour of the structure in study. They are just an approximation and the validation of FEMs needs to be done with experimental tests. More information about the tests is discussed in the next chapters.

Static loading structural simulations have utmost importance because they allow the study of the stiffness properties of a structure, being usually used to perform ultimate fracture analysis and displacement or torsion shape analysis. On the other hand, dynamic analysis are not less important. They can output modal responses and help problems involving noise and fatigue damage.

As a pre-testing tool, FEMs are fundamental also to help the engineer improve test planning quality. As already mentioned on chapter 2, when looking to FEM simulations, approximated optimum conditions can be obtained. For example, while choosing the excitation and responses locations to measure it is good to have a primary idea of where the nodal points are, in order to avoid unsuccessful data for the study.

Even after this analysis, as in any structural modelling, it is acceptable and expected to find some differences when comparing the computational model with the manufactured structure. This discrepancy can have origin in assumptions made on the mathematical model or numerical modelling of the structural problem.

The structure's representation, choosen mesh, elements used, material properties, manufacturing details like joining parts, methods and boundary condition, are hard to exactly match in the experimental work and cause some of this differences.

The remainder of this chapter includes an analysis of the first differences between the mathematical and experimental models, followed by a presentation of the computational results obtained from a load case simulation and also a dynamic modal analysis of the FEM.

3.1 Model Description

The development of the FEM is out of the scope of this thesis, but to briefly introduce the model used during this work some details and information are presented next.

The geometry of the FEM will be derived from the Computer Aided Design (CAD) used to design and fabricate the aircraft, managed within *SolidWorks*.

Using the optimized geometry it is time to use *Ansys ® Workbench version 19.3.* to develop the mesh. Several meshes were applied with increasingly fine granularity to investigate balance between solution approximation and computation time.

As a prerequisite to all analyses, the element stiffness matrices must be available. For dynamic analysis also the element mass matrices are required.

A FEM is built by discretization of a structure into a number of welldefined geometrical elements. Each of this elements is characterized by dimensions, number of connected nodes, material and geometrical properties. Mass and stiffness matrices are obtained by assembling them to each individual element and the formulation used to compute these matricies depends on the characteristics of the elements.

The wing structure consists of the upper and lower skins, front and aft spars, aft spar insert, ribs and titanium bushings. For the surface skin and ribs it was used a shell element type, which designation is SHELL 181 in *Ansys* software, with composite material associated. For the spars it was used solid elements, nominated as SOLID 186 on *Ansys*, with composite (layered solid) associated. The software includes a composite material module (ACP) that allows for composite material layups setup and postprocessing of analysis results.

A fudamental component regarding the study consists in making sure that the boundary conditions are matching between in-flight or ground tests and computational simulations performed. In order to simulate the wing attached to the fuselage, exactly in the same way as it should be in the real aircraft, the fixed boundary conditions used for both static and modal analysis were four holes on the spars. These are the holes used to make the connection to the fuselage, using bolts. Since these holes are presented on the real structure and on the original FEM, they are the best option to represent and match properly the in flight, computational and testing conditions.

The fixed constraint in all DOF option was chosen because the aircraft's fuselage, due to high stiffness properties, can be considered as rigid. Considering this, having a fixed constraint near the root is deemed as a good representation of operational conditions. It was also considered that differences between computational and experimental boundary conditions should negligible.

The coordinate system chosen was with X representing the longitudinal axis, more specifically, the chordwise direction, Y the yaw axis and Z the spanwise direction or pitch axis.

3.2 Primary Differences Comparing with Manufactured Model

As mentioned before, it is expected to find some differences when comparing the computational with manufactured structure. Preliminary differences were detected even before testing the structure and can show how hard is to have an exact FEM to represent the structural static and dynamic behavior.

Table 3.1 shows the comparison between FEM predicted mass and an estimated excess mass breakdown based on information from the manufacturer about the amount of Duratec primer used, measurements before and after painting, non-structural internals mass and the previous assessment of deviations relative to the expected material density.

Table 3.1: Comparison between actual, FEM predicted mass and estimated excess mass breakdown on the starboard wing.

Starboard Wing	Mass (g)	FEM mass (%)
Predicted FEM mass	6970	100.00
Total wing mass	11150	160.00
Excess resin (density)	418.2	6.00
Bonding resin	459	6.60
Duratec	737	10.60
Paint	450	6.50
Non struc internals	379.8	5.40
Strutural mass	8706	124.90
Excess	1736	24.90

After all accounted mass deviations there is still about 25% excess mass that was not accounted for in the model. These differences are attributed mainly to the filleting used to increase the bonding area between skin and spars and ribs as well as to the final glassing of the whole internal wing surface although in much less significant degree.

This divergence of the mass needs to be corrected at this stage in order to improve the quality of pairing between computational and experimental modal results to perform later. The easiest way to update the mass of the FEM without compromising all the details is to change the density of the composite. The density of the composite used, with an original value of 1450 Kg/m^3, is updated to 2162 Kg/m^3 in order to get the 11,15 Kg of mass instead the predicted 6,97 Kg. At this moment, it is possible to implement this first update because it is possible to measure with high accuracy the real mass of the manufactured structure.

To understand how this differences can affect the rigidity and dynamic response, the tests were performed and the results can be visible in chapter 4.

3.3 Static Analysis Results

Ansys static analysis allows determination of the displacement and rotations at the nodal DOFs under static nodal loading. The main objective of the static analysis in this study is to simulate 30% or

more of predicted deflection under the maximum operating load 2.5g's pull up manoeuvrer in flight. For that, the choice is about how the load can be applied and what should be the magnitude of the load. The magnitude values used for this study and the method to choose the different load cases are part of the static test planning, detailed information about that can be found on section 4.1.

The loading cases analysed on *Ansys* software were:

1. 100N vertical load applied at the tip aligned with the aerodynamic center;

2. 225N vertical load applied at the tip aligned with the aerodynamic center;

3. 225N vertical load applied at the tip aligned with the aft spar;

4. 225N vertical load applied at the tip near the leading edge.

The first two loading cases are usefull to understand the vertical deflections along the span for rigity analysis and the last two loading cases are important for a twist analysis along the span. Applying the load at different chordwise points. The twist angle will vary and more obvious distributions can be evaluated. The results of the static loading cases number 1 and 2, obtained from the FEA, are presented on the figure 3.1. The second load case is the most important to analyse because it is the choosen to perform the model update with the static tests data. On the first loading test the deflections are small, in the order of milimeters along more than half of the span of the wing, which means it difficult *FEMtools* software to perform the model update with such small reference parameters. For that reason, after some testing on the software, the second load case showed improved results. It can be observed a maximum deflection at the tip of approximately 3.7 centimeters for the first loading case and 7.6 centimeters for the second loading case. A chord wise average distribution of deflections along the span taken from the static load cases three and four are used to calculate the twist distribution. Both deflections results and twist distribution are presented in figure 3.2.
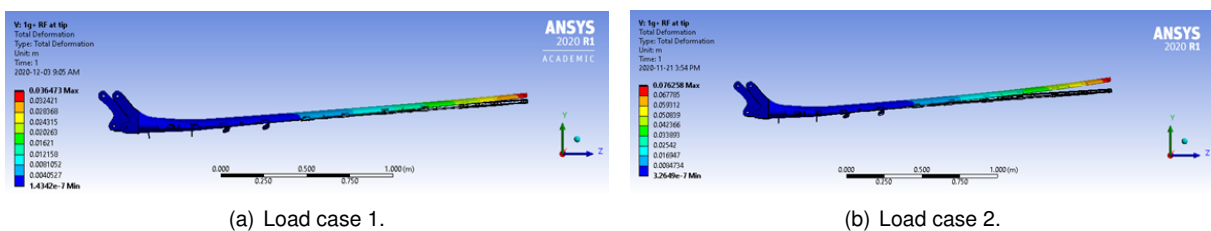

(a) Load case 1.   (b) Load case 2.

Figure 3.1: *Ansys* FEM static loading reults.

3.4 Modal Analysis Results

In order to match as well as possible the dynamic response of the original aircraft structure, a computational modal analysis improves the probability of success. This part of the process is fundamental before testing because, resorting to pretesting tools, it is possible to optimize the test plan. The computational modal analysis can give an approximation of the expected response. This information is precious

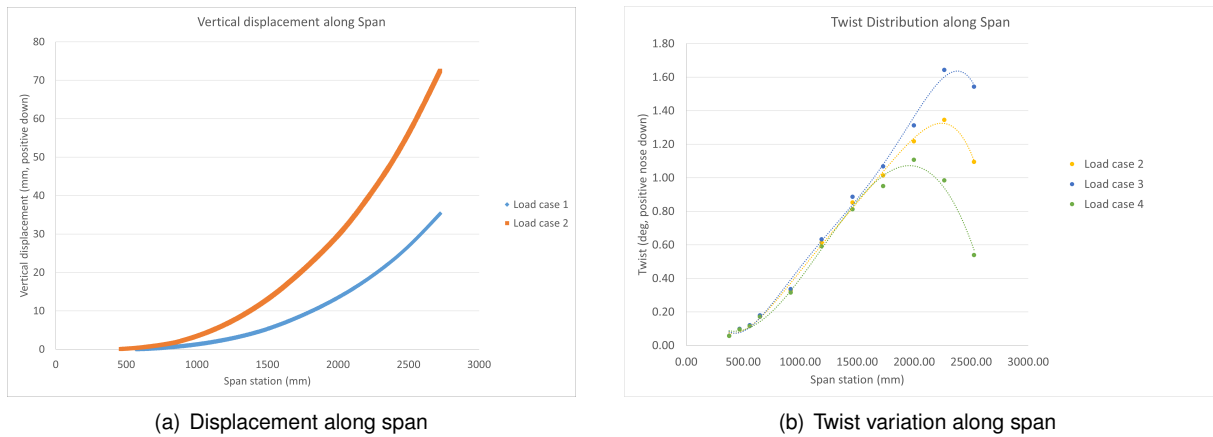(a) Displacement along span   (b) Twist variation along span

Figure 3.2: Results obtained from a static loading FEA

to choose where to install the sensors for the experimental tests, aiming to avoid nodal points and obtain data from points that can correctly represent all the targeted mode shapes separately.

To perform the FEM update, these computational results are also essential. Static loading tests can describe the stiffness properties of the structure but they can not convey the mass distribution information. Thus, the model update resorting to experimental modal testing can not be negleted.

The modal analysis' outputs consist of two important responses: natural frequencies and modal displacements of the structures. Each mode shape is associated to a specific natural frequency for which the results are presented in table 3.2 and figure 3.3 below.

In this specific case of study, the first six natural frequencies were analysed aiming to obtain the first in and out of plane modes as well as to visualize an approximation of the first torsion mode. This limit was defined because flutter can occur from a combination of the first out of plane and first torsion modes, therefore it is necessary to analyse the modal responses up to the first torsion mode.

Table 3.2: FEA natural frequencies extracted from *Ansys*.

FEA mode #	Frequency (Hz)
1	9.59
2	37.80
3	42.09
4	92.17
5	128.43
6	153.27

As it is possible to visualize in figure 3.3, it is expected to have the first frequency corresponding to the first bending mode around 9.6 Hz, the second frequency to the second bending mode around 37.8 Hz, the third frequency to the first in-plane mode around 42.1 Hz, the fourth frequency to the third bending mode around 92.2 Hz, the fifth frequency of 128.4 Hz to the second in-plane mode and finally the sixth mode corresponds to the first torsional mode around 153.3 Hz.
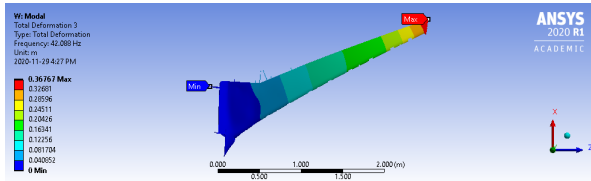
All this results will be used to compare and validate data in the next sections. They provide a first glimpse to check if the results obtained from the GVT are similar. High difference in frequencies may indicate that values of the experiences is incorrect and needs to be repeated. Nevertheless GVT results
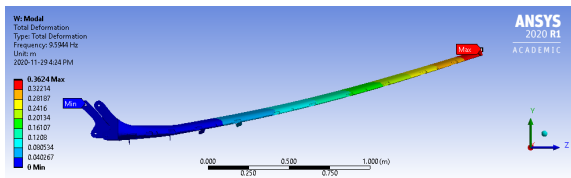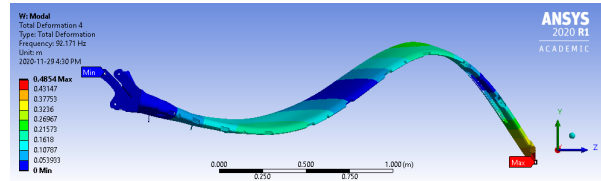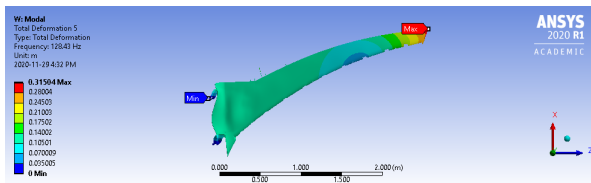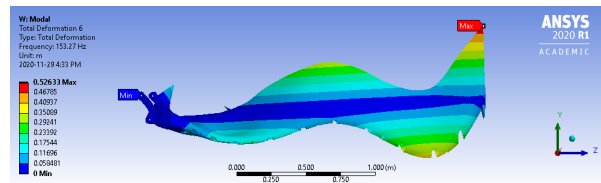
(a) First mode
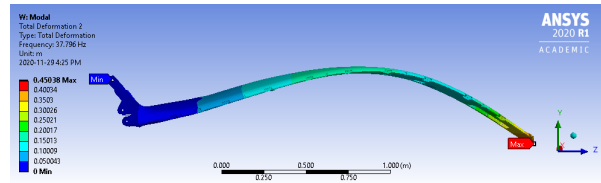
(b) Second mode

(c) Third mode

(d) Fourth mode

(e) Fifth mode

(f) Sixth mode

Figure 3.3: *Ansys* FEM modal analysis.

always have priority once validated.

Chapter 4

Static Testing

The most accurate method to verify the real characteristics of a structure is to perform experimental tests. Apart the disadvantage of possibly being expensive and time-consuming, they are irreplaceable to build a strong and reliable computational model of a structure.

Static loading tests are of utmost importance to provide information for verification of the FEM. For these experiments, the structure is intentionally deformed in several configurations with varying loads. For each loading case, displacements of specific chosen points along the span and the chord of the wing will be measured in order to extract the bending and the twist deformation of the structure.

The number of points chosen to measure the deflections needs to be high enough to have an accurate description of the deflected shape when load is applied but, at the same time, this number can not be exaggerated. As this number increases, the amount of time needed to find the measurement points position, attaching the stickers and, more importantly, for future post processing of all the data, becomes unacceptable. For that reason, this choice is made by the technician taking into account the level of precision required and the time available to perform the tests.

A note about the gravity load: it is important to know that in experimental wing loading tests, the presence of gravity can not be eliminated and for that reason, it is important to consider this force when performing the computational analysis and obtain comparable results.

The remainder of this chapter begins with a presentation of the test plan for the static loading tests followed by the experimental setup used. It finishes describing the results obtained and a brief discussion about the resemblance between computational and experimental data.

4.1 Test Plan

One of the first parameters to determine when planning a static loading test are: how the load is applied on the structure and what is the magnitude of that load in order to simulate a specific condition. As previously mentioned, the load should produce 30% or more of deflection with maximum operational load corespondent to a 2.5g's pull up manouvre. The FEM results provided for this flight condition show a deflection of 3.6 cm with the load applied at the tip of the wing. Calculations with *Ansys* for this requisit

show that aplying a load of 100N will result in an estimated displacement of 3.6 centimeters of maximum deflection at the tip.

In order to increase the displacement magnitude (aiming to get 7.4 centimeters of maximum deflection at the tip) the magnitude of the load to apply was 225N.

Due to the small maximum deflections obtained for the 100N loading at the tip, this second option is also an advantage for the model update. It is easier to obtain higher accuracy results on the stiffness model update with the 225N loading case. *FEMtools* considers zero all the values of deflections lower than 1 milimeter for this experiment values scale, which will affect a significant number of points in the 100N loading case.

The experimental setup consists in developing a jig that will be attached to an optical table and use four holes on the spars to fix the wing to the jig, upside down. Then, an aluminium part will be manufactured to fit in the tip of the wing with the purpose applying the load at three different chordwise positions: near the leading edge, the trailing edge and at the aerodynamic center. The leading and trailing edge options exists in order to force the twist deformation magnitude increase and, with the deflections results, calculate the twist distribution data to compare with the computational model. The load will be suspended at the tip of the wing in order to have loading test similar to the sum of the applied and the gravity load. The planned setup is presented on figure 4.1.
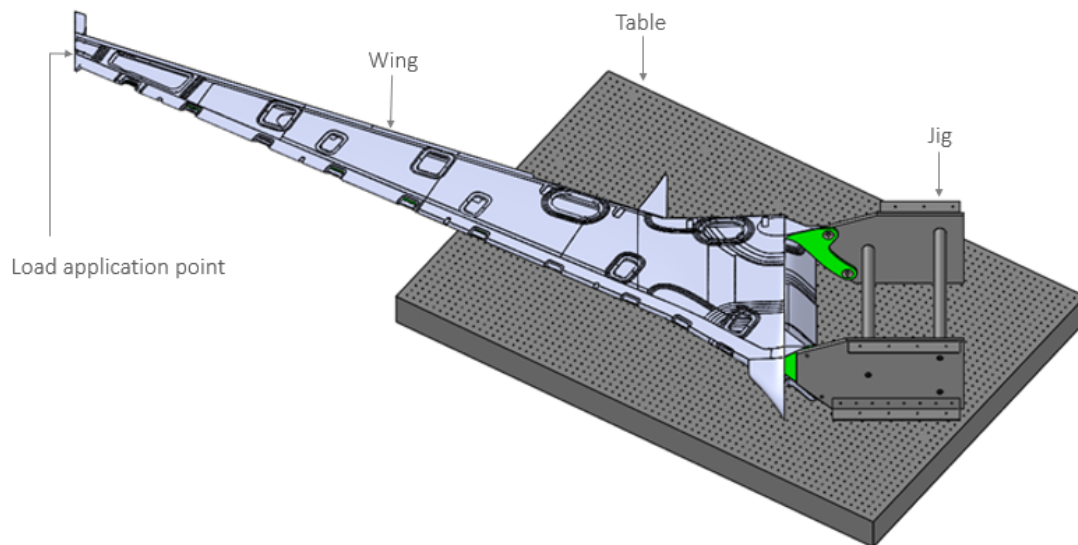

Figure 4.1: Planned static test setup.

As mentioned before, approximates 100N and 225N will be applied on the wing tip and the scanning of the deflections will be measured in the six load cases presented below:

1. While resting mounted on the jig designed for that purpose;

2. Under a 10Kg load at the tip aligned with the aerodynamic center;

3. Under a 22.5Kg load at the tip aligned with the aerodynamic center;

4. Under a 22.5Kg load at the tip aligned with the aft spar;

5. Under a 22.5Kg load at the tip near the leading edge (LE);

6. After unloading the wing.

Another import planning detail is where to measure the deflections. Since the measurements were obtained with a hand scanner, already described on section 2.1, fiducial stickers need to be placed along the wing on the points of interest for the study.

For this experimental work, 6 points chordwise in 11 sections along the span were considered, 3 points per section on the top surface and another 3 points per section on the bottom surface of the wing. The distribution of the stickers in the top surface is visible in figure 4.2 and the displacement on the bottom surface will follow the same pattern. With these measurement points placement, it is assured enough data to accurately characterize the wing deflection shape for each load case. The middle chordwise position stickers can give an average value of the deflection along the span and the stickers along the front and aft spars will provide validation to the bending shape and detail on the twist behavior.

The plan to mark the position of these fiducial stickers consists in using tape to define the front and back spar's lines and also different spanwise sections perpendicular to the root, as visible on figure 4.2. The distances used to define these sections were calculated refered to preexisting pressure port points on the wing.
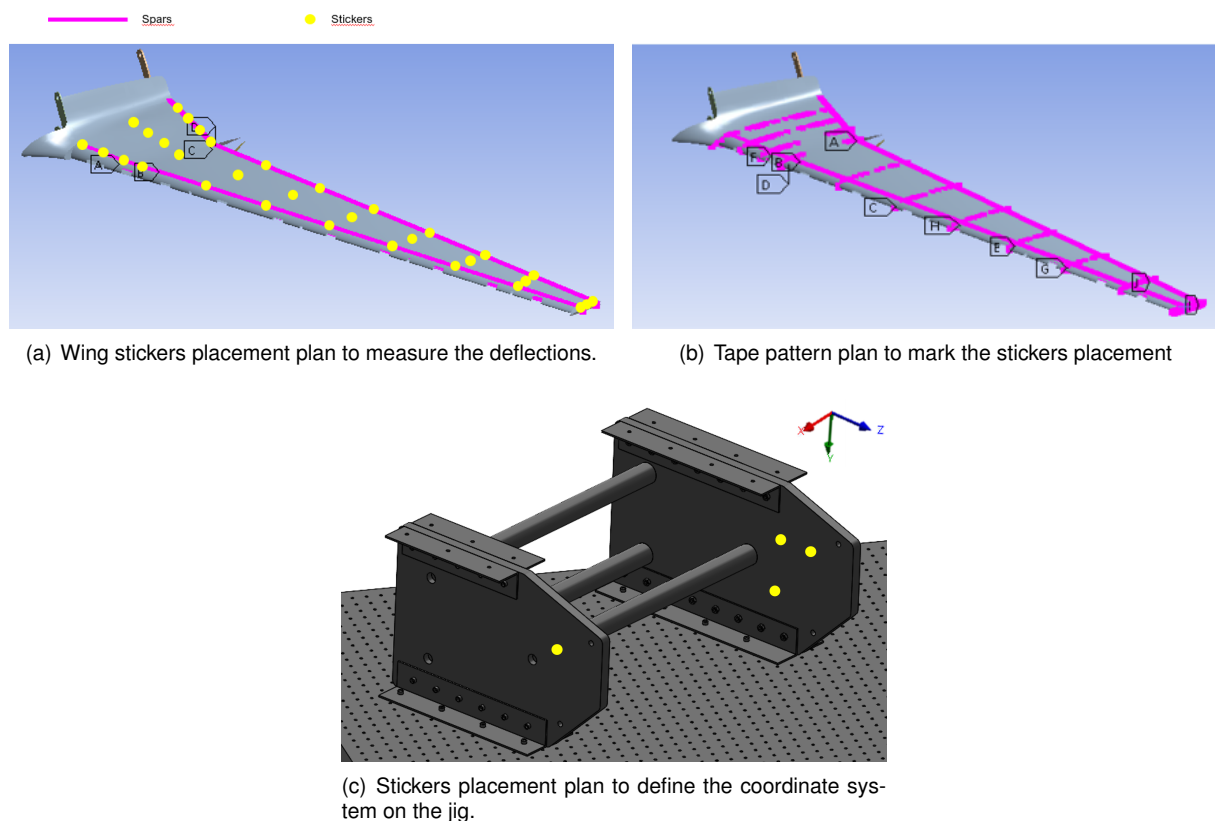

(a) Wing stickers placement plan to measure the deflections.

(b) Tape pattern plan to mark the stickers placement

(c) Stickers placement plan to define the coordinate system on the jig.

Figure 4.2: Fiducial stickers placement plan for the static tests.

To define a coordinate system, 4 fiducial markers need to be sticked in a reference structure in order to provide a reference frame for the scanning. It was chosen to define the coordinate system on the jig to be always the same for all the different loading cases and not be affected by any displacements.

The orientation of the coordinate system used was the same as the FEM to simplify the analysis. X represents the roll axis, Y the yaw axis and Z the pitch axis of the aircraft. This reference frame can be visible in figure 4.2.

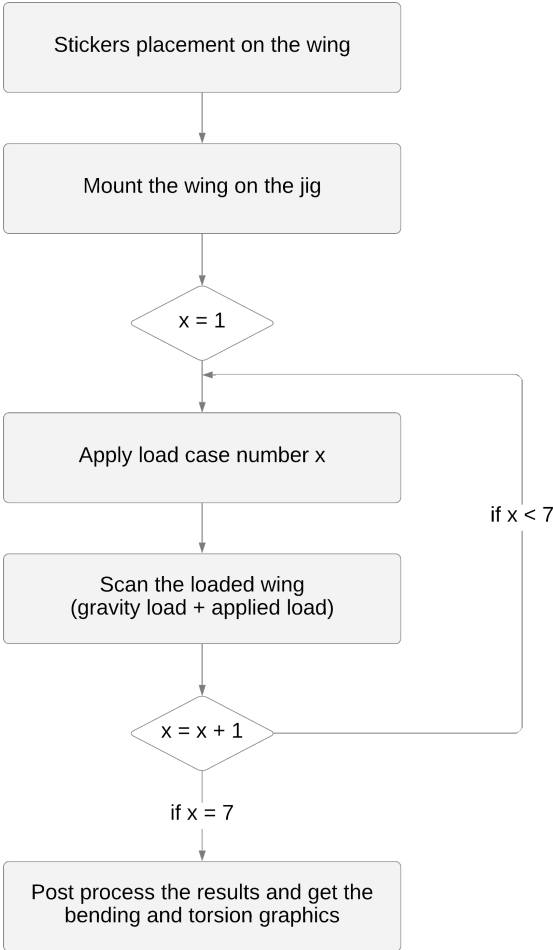A summary schematic of the planned process to perform the static loading tests is presented in figure 4.3.

Figure 4.3: Schematic of static test plan.

4.2 Experimental Setup

A large, heavy, and unyielding jig was manufactured with the objective of not interfering with the displacements of the wing and assure the boundary conditions planned. The material used was steel and it was fixed to an optical table with 48 steel screws to ensure negligeble displacements during the experience apart from the wing deflection. This jig also provides adequate boundaries conditions with tight tolerance using precise bushings to avoid displacements of the assembled surfaces.

To help marking the precise placement of the measurement points, planned on the section 4.1, green tape was used to define the spanwise sections, as visible on figure 4.4. Then, 64 fiducial stickers, 33 on the upper surface and 31 on the lower surface, are on the corrected positions along the wing and it is

ready to be mounted on the jig. 2 points are impossible to be marked because they fail in some match holes on the lower surface, for flight control actuators attachement. However, since there are a sufficient number of points in the study, the results should not be affected by the removal of these 2 points.

(a) Tape lines to help finding the exact position of fiducial stickers.

(b) Fiducial stickers placement on the wing

Figure 4.4: Strategy used to stitch the fiducial stickers.

The wing was mounted on the jig with its upper surface facing down. The assemblage of the wing to the jig was done the same way as it is fixed to the fuselage, in four points, two per spar, as shown on the figure 4.5.

Additional stickers were placed in the wing surface, on the mounting jig and table to facilitate the scanning and help establish a reference coordinate system to be used for displacement determination. Along with the 3D scanning and as a way to control some unexpected excessive deflection, a ruler was placed behind the wing tip in order to roughly monitor the vertical displacement of the tip.
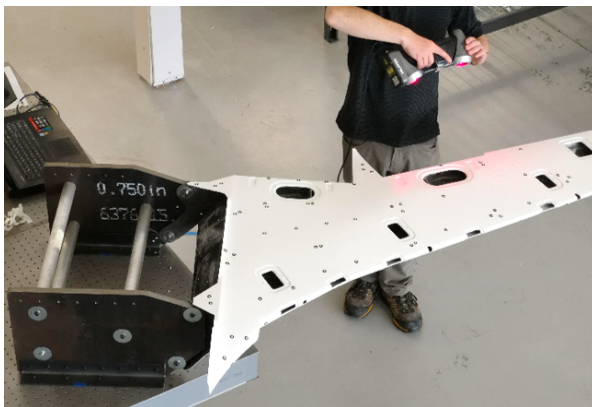
(a) Scanning of the mounted wing.

(b) Static tests setup with load applied on the tip.

Figure 4.5: Experimental Setup for Static Testing

Load application was done by bolting a custom manufactured aluminium part to the winglet attachment box in the wingtip, visible on figure 4.5. A crate progressively filled with 2.5 Kg sand bags was hanged on this custom part in order to reproduce the FEM analyzed load cases. Between each load case, a 2,5 Kg increment loading strategy was implemented instead of direct loading the 10 or 22,5 Kg. This technique may avoid some possible failing of the structure due to systematic inspecting of the

structural condition along the loading process. The hanging point was changed during the tests from loading case three to four and four to five. Both the custom part and the cradle were accounted for the total load on the wing.

After each load case, the fiducial stickers position on the wing is scanned. Comparing the position of these stickers from each load case to the first load case without load applied it is possible to find the displacements of the points.

4.3   Results

After collecting the data of the 64 fiducial stickers from the experimental tests, it is time to look at the results and post process in order to correctly analyse the information.

The data acquired on the 3D scanning are the coordinates in space of the fiducial stickers' points. In order to analyse the results with accuracy, the most effective approach is to look at displacements that represent the deflections between cases under load applied and inital case without any loading at the tip. Joining all the displacements in a graph it is possible to visualize the bending shape resulted from the load applied. The sixth loading case may seem redundant but it is important to determine if during all the loading cases, the wing was subjected to any plastic deformation.

The post processing of the wing scans data showed a significant difference in vertical position between initial resting shape and post loading shape (about 16mm). When analysing the data it was confirmed that despite that difference, if rotated around the longitudinal axis (parallel to the X axis in the aircraft) of the reference coordinate system, the shapes of the initial and post loading structures were coincident. This means that the structure experienced a rigid body rotation during the test. This suggests that probably a small displacement on the bonding between the attachment bushings and the spars occured, although not confirmed. Anyway, no permanent deformation was found.

To double check the vertical displacement magnitude, the static load tests were repeated for the third case and measurements were taken with a ruler only, without 3D scanning. After repeating the loading process 2 times for each case, the resting shape and post loading shapes were confirmed to be the same. It results on a vertical displacement around 58 mm when the load was applied at the trailing edge and about 56mm when applied at aerodynamic center. Figure 4.7 and figure 4.6 show the measurements taken.

The measurements obtained match with the 3D scan results displacements if calculated relatively to the post loading results. For this reason, the following displacement and twist results are relative to the post-loading wing shape.

Figure 4.8 and figure 4.10 depict the comparison between experimental results and FEM results for the third, fourth and fifth cases while figure 4.9 shows the experimental twist displacement results.

In figure 4.8, it is visible that the wing is significantly stiffer than predicted. The expected vertical displacement at the wing tip is around 40% different when compared to the experimental results. The experimental wing curvature shows consistently higher values along the wing span than the ones obtained in the computational static. Changing the load application point from the trailing edge to the
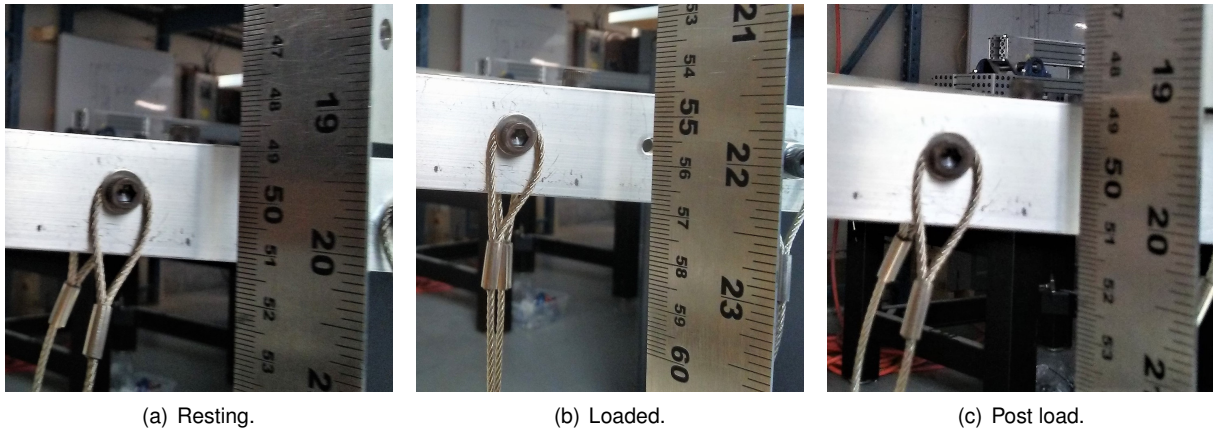
| (a) Resting. | (b) Loaded. | (c) Post load. |

Figure 4.6: Measurements at the aerodynamic center for the loading case three.

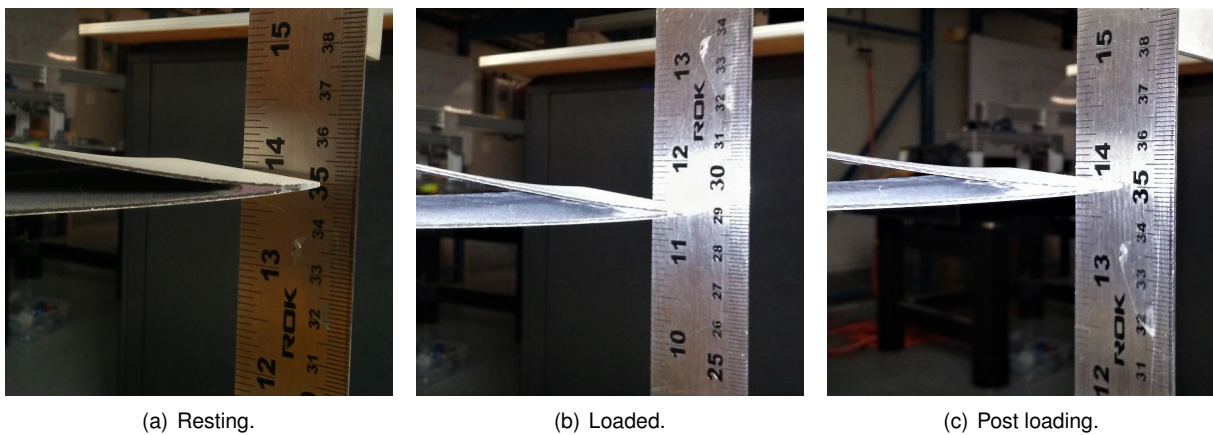| (a) Resting. | (b) Loaded. | (c) Post loading. |

Figure 4.7: Measurements at the aft spar for the loading case four.

leading edge also slightly increases the displacement. This was verified both in the FEM and the experimental results.

In figure 4.9, it is visible that two values for twist per section were used. These two values per section were obtained from CAD drawings by calculating the difference between the post loading and loaded angles relative to the horizontal direction of the vectors defined by the points closer to the leading edge of the upper and lower surfaces. In figure 4.11, the two values represent the upper and lower surface twist with the lower magnitude values corresponding to the lower surface.

It is important to note that the twist tends to invert the trend in areas closer to the wing tip as the loading application point is moved towards the leading edge. Figure 4.10 shows that the previously mentioned pattern is captured by the FEM although with a different magnitude. It also shows that the torsional stiffness of the wing is under predicted by the FEM.

In conclusion, the experimental results show that the significant increase in structural mass is followed by a significant increase in torsional and bending stiffness of the wing.
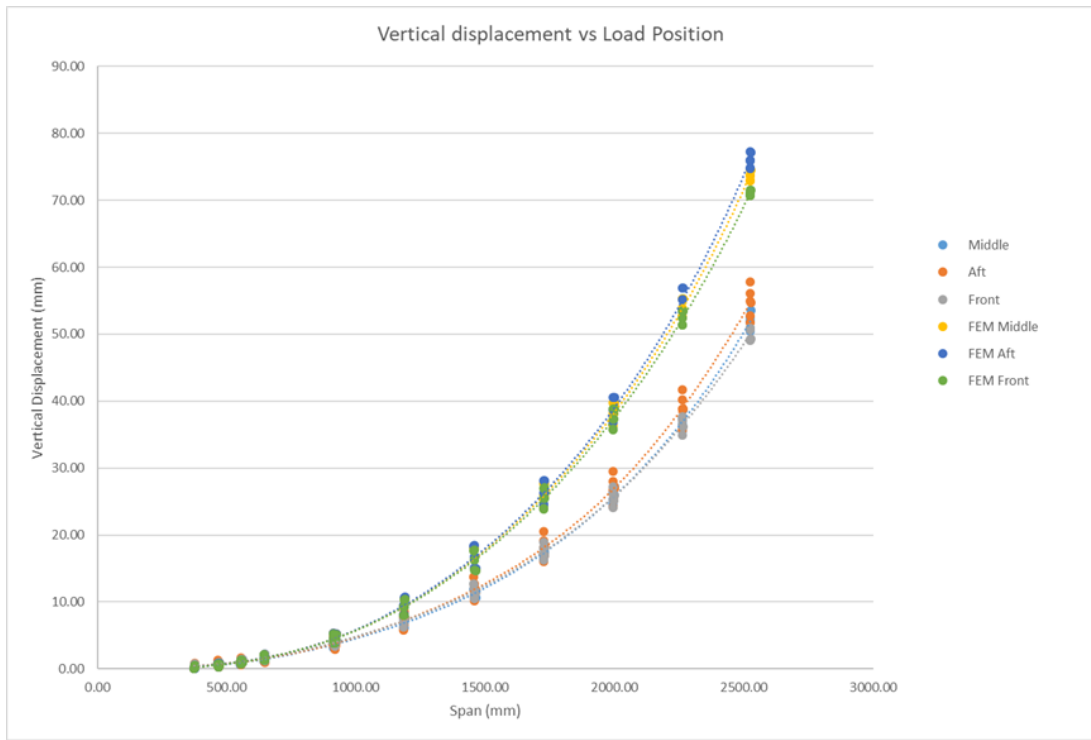
Figure 4.8: Comparison between experimental and FEM vertical displacement results for different loading positions.
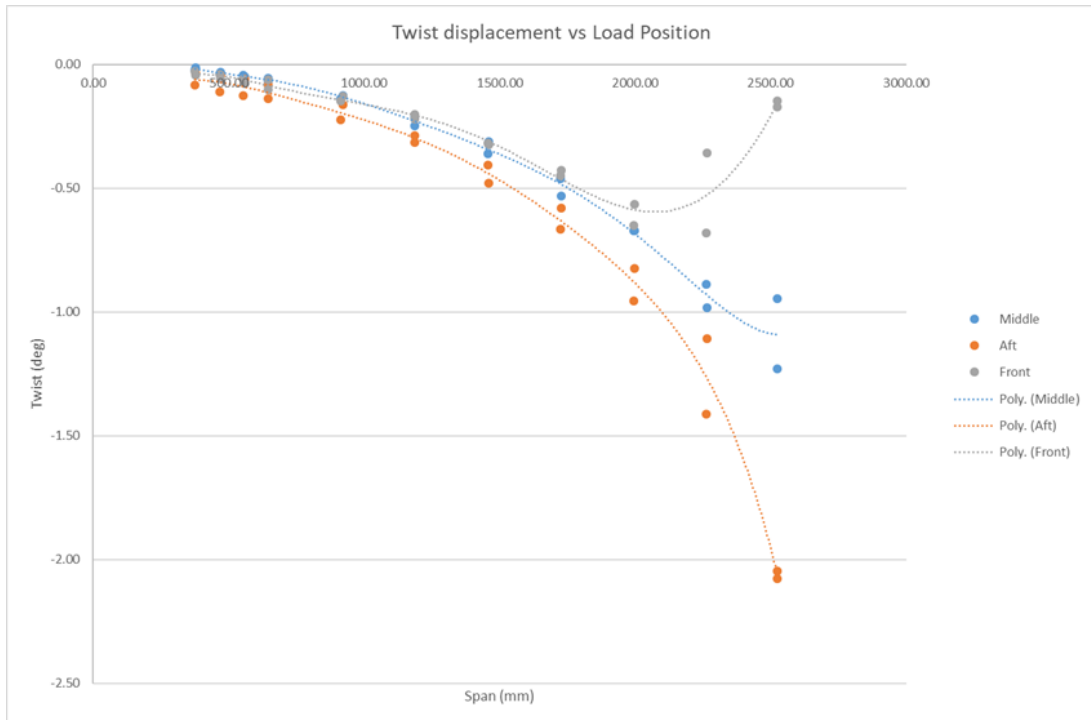

Figure 4.9: Experimental Twist displacement results for different load positions (cases 3, 4 and 5).

Figure 4.10: Comparison between experimental and FEM twist displacement results for different load positions (cases 3, 4 and 5).

Figure 4.11: Retrieving the twist displacement.

Chapter 5

Ground Vibration Testing

GVT are the experiments performed to study the dynamic behaviour of a structure. The main goal of this work is to validate the structure's FEM and generate a stick model with the same behaviour as the real structure in order to perform aeroservoelastic calculations later. The extraction of modal parameters to validate the original model and perform any model update can be obtained from the post processing of the GVT results.

Compared to the static loading tests, GVT have the disadvantage of being more expensive. The instrumentation and equipement used in this experimental work, due to the high accuracy level required, is sometimes impossible to afford for small projects. However, it is of importance to determine the modal characteristics of the structure. It is also a standard procedure for structural certification in the aeroespace field. As it will be discussed in the end of this chapter, static tests are not enough to demontrate properties or to validate a FEM.

Elaborating a test plan with optimized conditions and doing the pre testing is of utmost importance to reduce experimental costs and time. A preliminary FEM modal analysis was performed and presented in section 3.4, mode targeting and sensor placement strategy is explored in the next section.

Despite the advantages, experimental modal testing can have limited outputs. For example, in structural dynamics, natural frequencies can be measured with high accuracy but limited in range. Less accurate results, but also possible to obtain, are mode displacements.

When perfoming experimental ground tests, the number of possible DOFs to measure is almost infite. For that reason, it is mandatory to decide what are the best points to record measurements. The execution of GVT is time-consuming and expensive, thus there is interest in finding the best compromise between having the less amount of locations to perform the impacts without jeopardizing the results.

The level of accuracy of the results obtained comes from the know-how and attention to detail dedicated when operating the instrumentation. Some known noise sources that might happen are associated to: test configuration (fixtures, excitation technique, locations of the measurements); calibration and distortions of the instrumentation and data acquisition system and eventual noise that can exist in the laboratory environment. Some of these noise sources can be eliminated or improved with experience of the technician and extra care.

The remainder of this chapter describes the test plan developed for the GVT, followed by the experimental setup used and finalized with a presentation of the data obtained and a brief discussion about the results.

5.1 Test Plan

The first stage of the test plan is the development of the jig. A modal analysis of the structure was done to make sure the jig's natural frequencies will be far from the wing's frequency range of interest. The range of frequencies in study is between 0Hz and 200Hz. A design requirement was to have a first natural frequency of the jig higher than 300Hz. This jig is the same one used on the static loading tests as it provides adequate boundary conditions as mentioned earlier.

Also mentioned was that the best GVT method for this case is to perform a roving hammer impact testing. This mean that transducers used to measure the responses are fixed and the hammer will impact the points of interest along the wing.

Instrumentation resources are limited in any experimental tests and althought, for this case of study, a single position of accelerometers is enough to have good results, there are 8 transducers available on the laboratory. In order to have redundancy on the results and different options to compare and choose the best outputs, 8 accelerometers should be used. Nevertheless, since the time consumption on model updating is high, only the best results' position is going to be used for that task.

Sensor selection tools from *FEMtools* software were used to help finding the optimum placement of the tansducers. The sensor elimination method, called SEAMAC and explained in detail in section 2.3.4, with 8 measurement devices available converged to the configuration visible in figure 5.1. The figure shows the positions where the accelerometers should be glued. There are only 4 positions because, for this study, it is important to measure the accelerations in two directions, X and Y. Since the piezoelectric accelerometers available are single axis, two accelerometers per position will be used. Z spanwise direction is not important to analyse for this case of study because frequencies will be higher for modes along this axis due to the high stiffness of the wing.

To fix two sensors in the same position, an aluminium cube will need to be manufactured to guarantee the orthogonality of the sensors. Aluminium material was choosen to avoid mass loading effects on the wing.

The next step is to define the number of impact points that best fits the compromise between having a non exaggerated amount of locations to perform the impacts and keeping enough data to well represent the behaviour.

A *LabVIEW* interface, already developed at CfAR, will be part of the data acquisition system. It is important to highlight that this interface was developed to record simultaneous information from 2 accelerometers. This means that each impact will output 2 FRFs, one per accelerometer connected to the interface. In order to have data from all the accelerometers, 4 impacts needs to be done, changing the transducers' connected between each impact.

To understand in the time consumption of all this process, 12 points for a preliminary analysis were
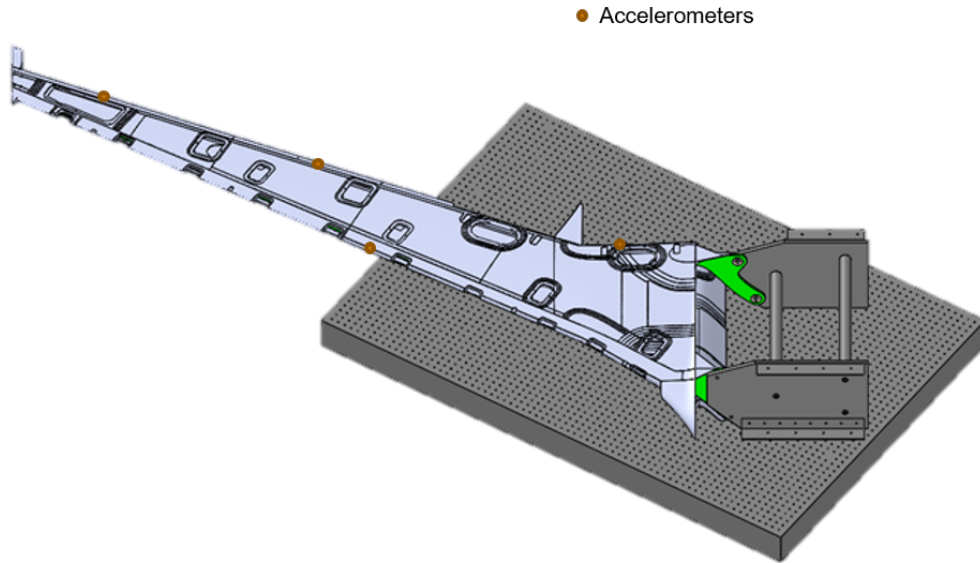
Figure 5.1: Planned GVT setup.

choosen. 6 impacts equaly distributed along the aft spar and other 6 along the front spar. This prelimi-nary choice will be important to analyse and check which sensor position is measuring the higher quality outputs. After chosing which sensor location measures the less noisy results, 25 points will be impacted to improve the quality of the mode displacements results. 12 equaly distributed points along the aft spar and 13 along the front spar lines.
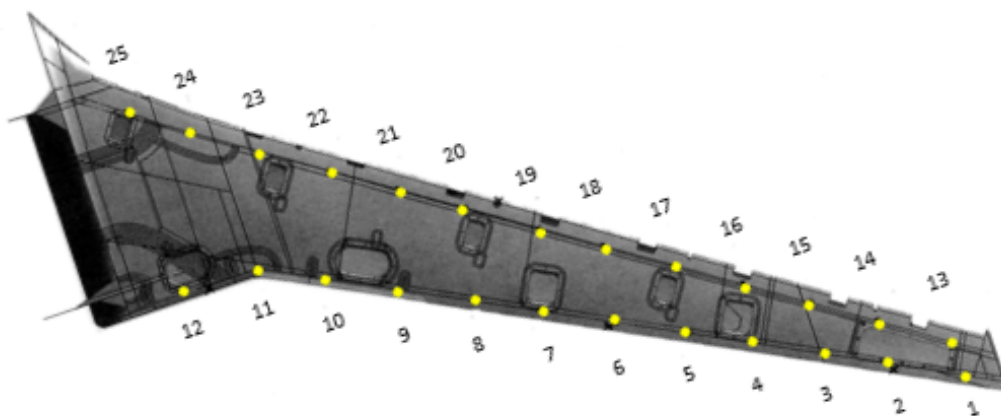

Figure 5.2: Roving impact DOFs for multi reference testing.

A schematic of the planned process to perform the GVT is presented in figure 5.3.
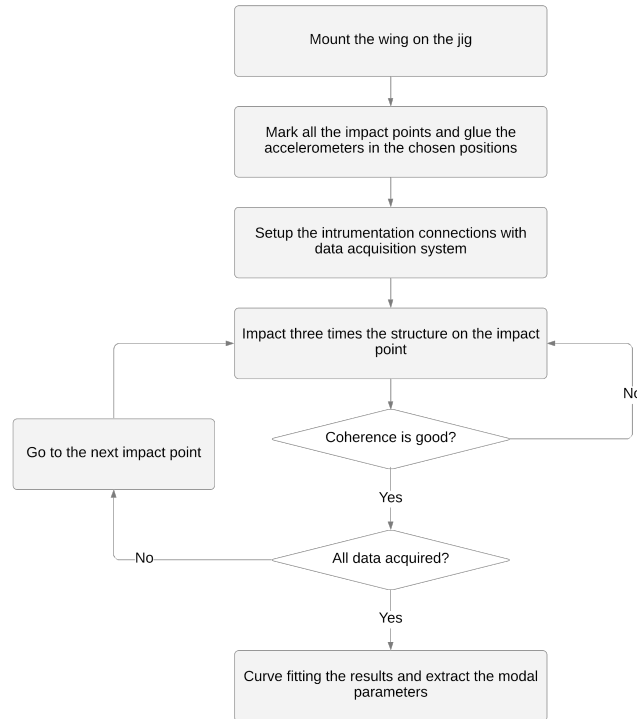
Figure 5.3: Schematic of GVT plan.

5.2 Experimental Setup

The wing was mounted upside down on the jig attached to a vibration isolated table, the same way it was previously mounted for the static loading tests. Details of the connection and boundary conditios were already explored in section 4.2.

The instrumentation used to impact the structure was a PCB model 086C03 hammer with the medium impedance tip (black rubber). For this type of high stiffness structures this tip is recomended but softer and harder tips were tested to verify if the results obtained would be better. It was checked the black rubber provides appropriete conditions for better results in this structure.

PCB miniature single axis piezoelectric accelerometers model 352A24 were the available sensors used to measure the response of the structure to the impact. In figure 5.4 it is visible the use of 2 single axis accelerometers glued to the aluminium manufactured cube, attached with petrowax to the wing's trailing and leading edge. A third accelerometer measuring the Z direction accelerations was glued to one of the cubes just to confirm no natural mode frequencies were hidden apart the ones detected in X and Y direction. After this confirmation it was removed again.

Before mounting the setup it is important to verify if the all the instrumentation is calibrated and working. Detailed specifications of the hammer and accelerometers used can be found in appendix A.

Data acquisition was accomplished using National Instruments (NI) 9234 IEPE acquisition cards connected to a NI cDAQ-9188 chassi. The PCB hammer and all the transducers are connected to the 9234 modules. The chassi will make the connection between the data acquired and the *LabVIEW*

(a) PCB single axis piezoelectric accelerometers mounted on the leading edge.

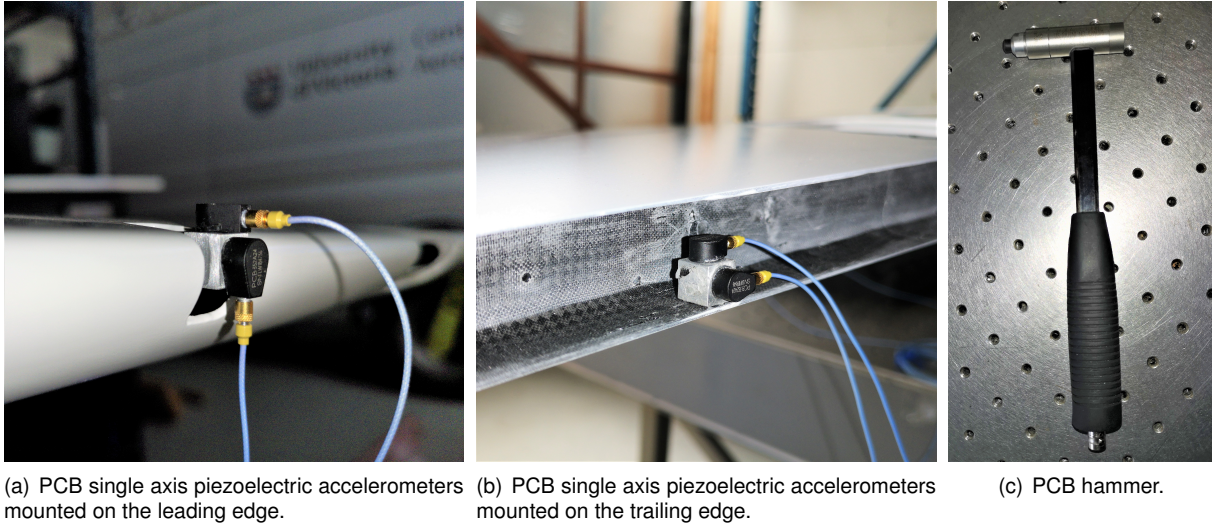(b) PCB single axis piezoelectric accelerometers mounted on the trailing edge.

(c) PCB hammer.

Figure 5.4: Intrumentation used on GVT.

interface.

It is important to highlight that in this stage of the experiment, there are a high number of cables to manage. It is mandatory to organize and divide them on the table because changes between accelerometers in the acquisition interface needs to be done and without organization it is almost impossible to understand which of the accelerometers is connected to a specific channel. It is also mandatory to fix the chassi to the table to avoid damage.
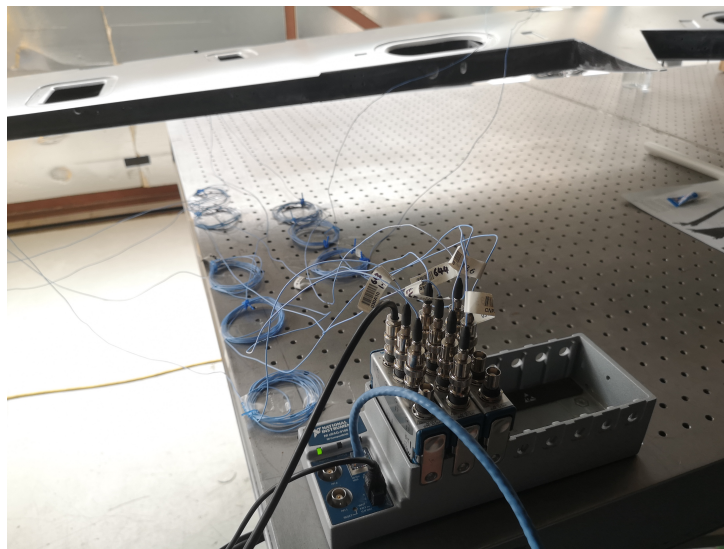
Figure 5.5: National Instruments 9234 IEPE modules connected to cDAQ-9188 chassis.

The hammer technique consists in doing short, narrow pulse impacts, always perpendicular to the structure. FRFs calculations are done by the *LabVIEW* software almost instantaneously when hitting the structure. To prevent errors or noise that may affect the results, 3 impacts needs to be done for the same DOF. An average of the 3 FRFs obtained is displayed on the interface and the experiment needs to be repeated untill values of coherence higher than 0.9 are reached all over the frequency interval under study. This coherence represents the similarity between the results. If this value is low, it means

something happened in one of the impacts, possibly noise or not perfect impacts.

(a) Accelerometer measuring Y direction.
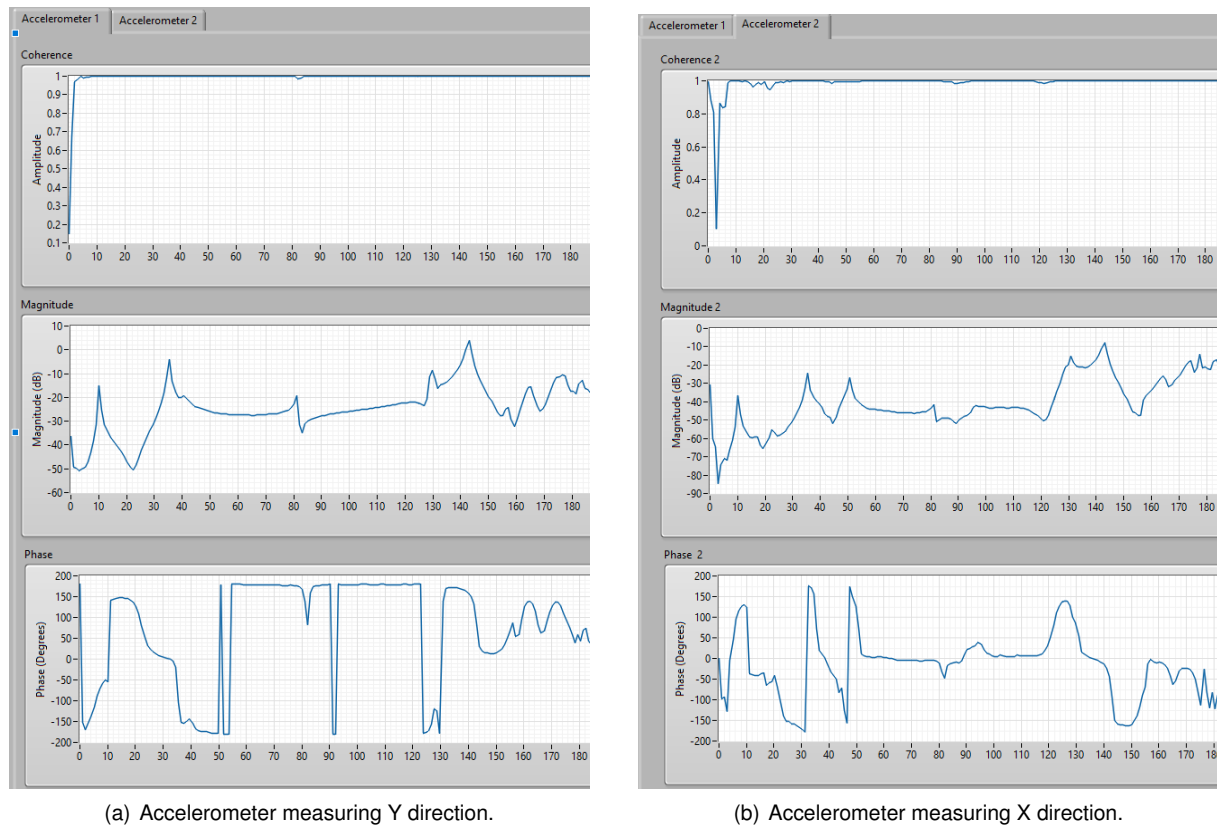
(b) Accelerometer measuring X direction.

Figure 5.6: *LabVIEW* interface output showing FRFs instantaneous calculations and coherence graph.

Intensive impacts training showed improvements in coherence. However note that for frequencies lower than 5Hz is hard to obtain reliable results. It happens not because of lack of impacting experience but because, due to so high sensitivity of the accelerometers used, noise in lower frequencies could not be totally eliminated. The minimum movement or sound in another room can be detected by the transducers and for that reason this values are to be accepted. However, it is not a problem because it happens away from the wing's expected frequencies.

At the end of the experiences, some flexibility in the schedule provided conditions to impact more points aiming to get better mode shapes representation of the structure, and consequently improve the results. The testing points planned form a mesh, previously presented in figure 5.2. It was decided to make a mesh refinement and instead of 25 impact points, 50 DOFs were impacted resulting in 100 FRFs, 50 in Y direction and another 50 in X direction.

5.3 Results

The experimental data acquired were accelerations(m/s^2), measured by the piezoelectric accelerometers and force(N), measured by the impact hammer with an impedance head. As already referred, this raw data goes across a *LabVIEW* interface that almost intantaneously, calculates the FRFs for each response.

This raw data available on the testing interface is helpfull to constantly check the results along the

experience and improve the quality of the technique based on this data. However, all the calculated FRFs to analyse needs be to curve fitted using *MEScope* software, by Vibrant Technology.

Before inputting the data in this software, all the FRFs' information needs to go over a *Matlab* script, adapted by the author of this thesis for this experience and previously developed at CfAR, in order to change the file formatting and organizing the results so that it can be read by *MEScope*.

The curve fitting done with the help of this software allows to isolate modes within the FRFs providing natural frequencies, mode damping and mode shapes.

Since 50 DOFs were studied resulting in 100 FRFs, it is not possible to present them all here, they are similar in shape, just different in magnitude and phase. Accordingly, only one of the results will be displayed here to help clarify some concepts.

An example of post processed magnitude and phase graphs from a FRF is presented in figure 5.7. It is possible to clearly identify the peaks on the magnitude graphs that correspond to the structure's natural frequencies. Note the relevance of measuring in the two directions. The peak around 50Hz, that corresponds to the first in plane mode, it is not visible in most of the FRFs obtained from the results of the accelerometer measuring Y direction. However, it is evident in all the results obtained with X direction measurements.

Although being easy to identify the peaks in the magnitude graph, the clear way to analyse the peak frequencies is looking to the imaginary graph of the FRFs. An overlaid of all the imaginary part of 100 FRFs is visible in figure 5.8 and all the natural frequencies can be evidently identified, with well defined sharp peaks. In the bottom chart of the same figure, it is possible to see the output of the quick curve fitting function of *MEScope* software. The black horizontal line on the graph limits the noisy area. All the peak values that might exist below this line are understood as noise and negleted. The complex mode indicator function (CMIF) is calculated using the polynomial method and all the peaks above the noise threshold line are counted.

At the first iteration of the quick fitting, the first inplane mode around 50 Hz was not identified. This happened because it only appears in half of the FRFs obtained (X measurements), resulting in the software interpreting as noise. This detail was quickly solved applying the smooth function to the mode indicator. Each time the mode indicator is smoothed, the natural frequencies' peaks will become wider and the modes more closely coupled. To obtain these results, CMIF using the imaginary part were smoothed only one time.

This post processed data converged in the extraction of the modal parameters presented in table 5.1.

The mode shapes of the structure associated to each of the natural frequencies presented in table 5.1 can be visible in figure 5.9. It is difficult to clearly identify which mode it corresponds to in the figure but in the animations on the software it is more evident. The mode shapes obtained correspond with the expected ones obtained from the modal FEA, presented in section 3.4.

The 6th and 7th modes obtained from the EMA are within a small difference to the first torsion mode obtained from the FEA. For that reason, it is not obvious which one corresponds to the first torsion. Observing the mode shape of the structure around 143Hz, a torsion mode can be identified but around
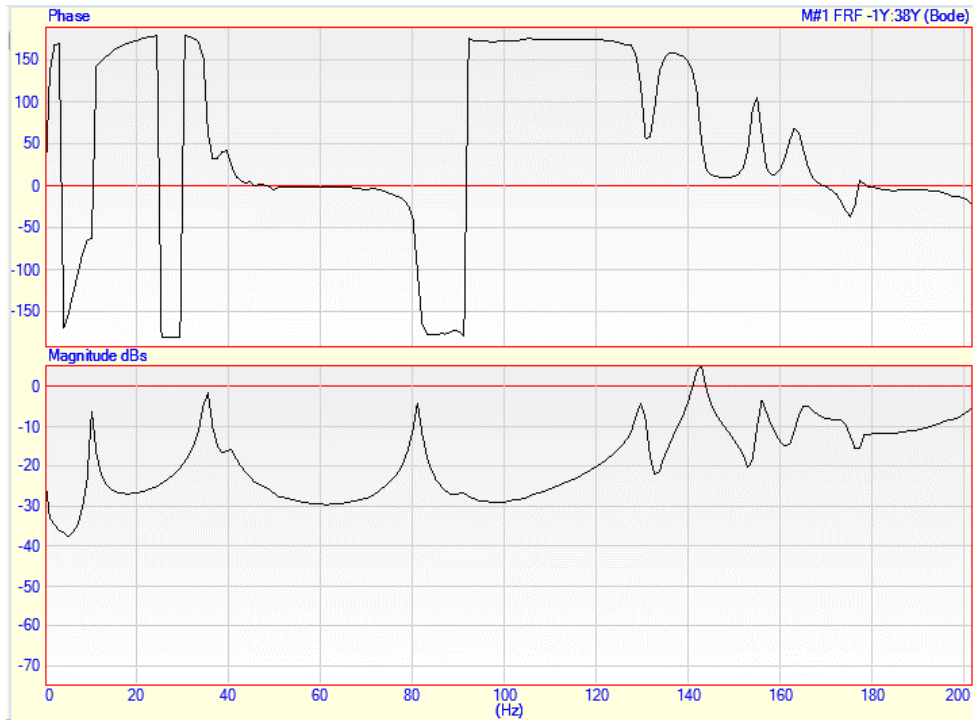
(a) Post processed FRF measured in Y direction.

(b) Post processed FRF measured in X direction.

Figure 5.7: *MEScope* software post processed magnitude and phase graphs from FRFs results for an impact in test point number 13.

157Hz the animation shows a strange shape that did not clearly allow the mode identification.

Since GVT is more time consuming and expensive than a static load test, one of the main goals of ground structural testing was to prove, when comparing the results of both tests, if it is reliable to validate the FEM model only resorting to static loading tests. From this experimental work results, it should be

52
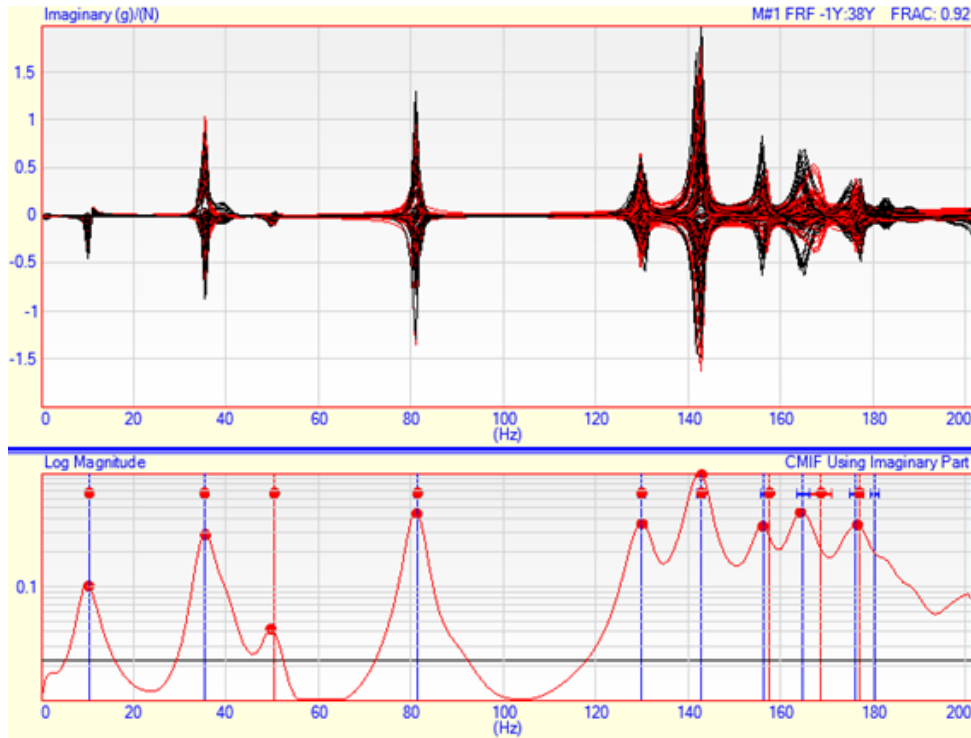
Figure 5.8: Automatic curve fitting function output of *MEScope* software used to determine the peaks correspondant to the natural frequencies.

Table 5.1: FEM vs EMA natural frequencies comparation.

Mode #	FEA Frequency (Hz)	EMA Frequency (Hz)	EMA Damping (Hz)	EMA Damping (%)	Difference (%)
1	9.59	10.34	0.04	0.39	7.35
2	37.80	35.28	0.52	1.47	-6.60
3	42.09	50.38	0.66	1.30	19.75
4	92.17	81.34	0.43	0.53	-11.79
5	128.43	129.80	0.77	0.60	1.22
6	153.27	142.72	0.82	0.58	-6.70
7	153.27	157.48	0.67	0.43	2.43

highlighted that the results of the static loading test are not proportional to the GVT's results. Differences around 40% between static loading tests results and FEA showed a significant increase in torsional and bending stiffness of the wing due to the significant increase in structural mass. It was expect to find differences in the same order of values when comparing GVT results with modal FEA, however, the average differences between experimental and computational natural frequencies is approximately 8.9%.

This difference values totally disprove the previous hipothesis. Having an increase in the stifness of the wing haven't affected that much the modal response. With this, it is imperative to perform both tests without the possibility of using one to replace the other.

(a) 1st out of plane.

(b) 2nd out of plane.

(c) 1st in plane.

(d) 3rd out of plane.

(e) 2nd in plane.

(f) 1st torsion.

(g) Not identified.
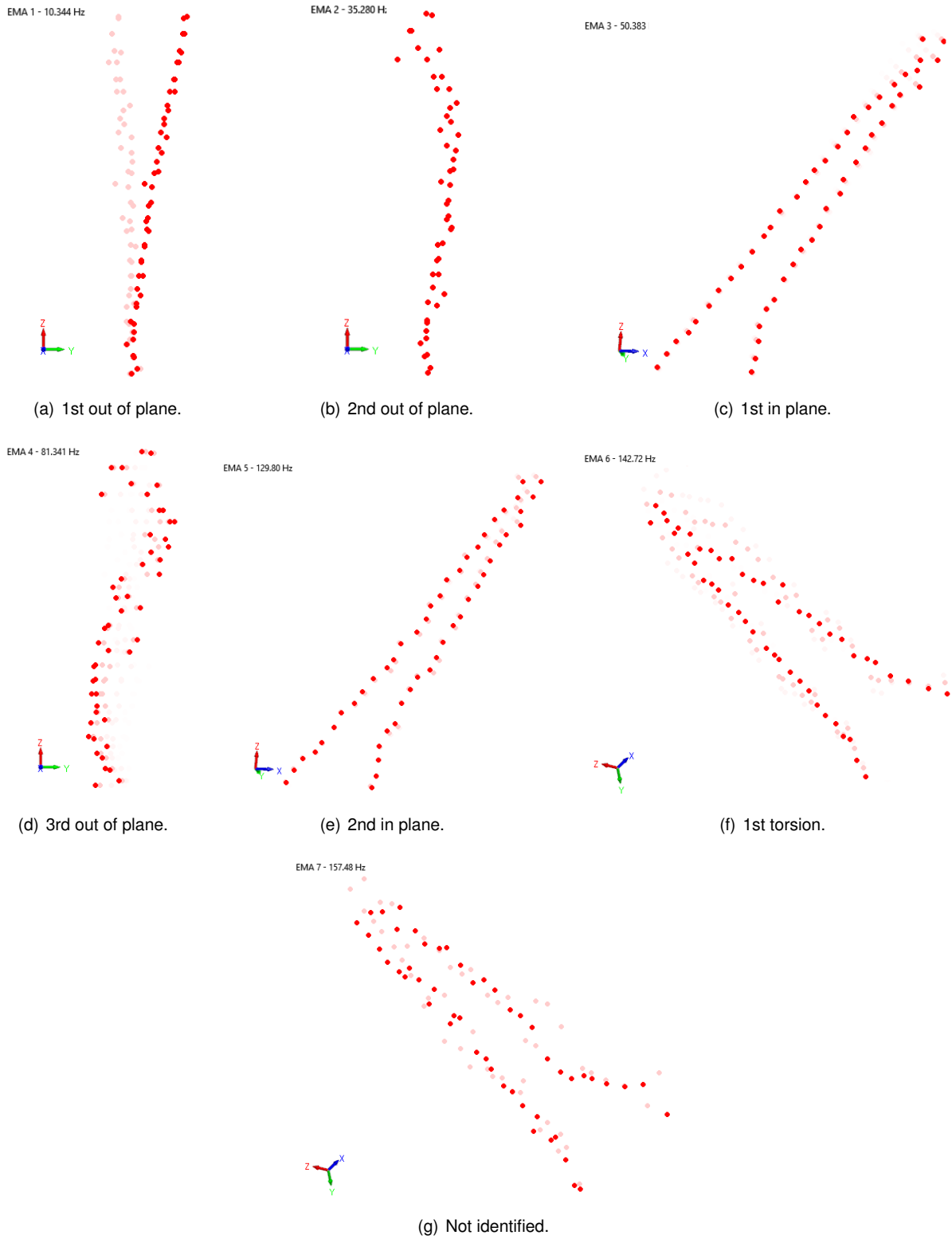
Figure 5.9: Experimental mode shapes associated to the natural frequencies.

Chapter 6

Beam Finite Element Model Update

To conlude this work, the last step consists in performing a model updating study of a FEM. The model-based approach begins with the development of a computational model, such as a FEM based on design calculations, to be matched using structural parameters to the experimental static load and GVT data.

The model updating process does not follow an already known specific procedure. For that reason, it can be done in different ways and generate always different outputs for each of them. The objective in model updating is to iteratively study and understand how can some parameters affect the model's responses and how can erros be avoided and minimized.

Recent science progress in data acquisition systems and sensors technology has improved the reliability of the nondestructive experimental work. High sensitive devices, used to measure the responses of a structure based on tests results can output essential information to update some chosen parameters of the FEM. This model needs to go over a calibration process that selects the less reliable model parameters which are impossible to be known *a priori*. A different range of methods can be used to find which measurements from the tests best match the model predictions.

In this study, it was impossible to perform the analysis on the original FEM of the wing due to the large size of the original model. It is impossible to input this complex model in both softwares used for the model updating and for the future aeroservoelastic calculations. This means that a new simplified FEM needs to be developed in order to correlate data between computational and experimental tests. The simplified model will be matched with the results obtained from the ground tests and updated in a way that ensures similar static and modal response behaviour to the real wing. The final model should be accurate enough to be used in a future flutter analysis at critical speed, a fundamental process on design and safety.

Sotware used to perform all the model updates was *FEMtools 4*, by Dinamic Design Solutions. It is a multi-functional, cross-platform and solver-independent family of Computer Aided Engineering (CAE) software programs providing analysis and scripting solutions for many different types of applications, such as modal pretest analysis and planning, sensitivity analysis, test-analysis correlation and FEM verification, validation, updating and optimization. Althought *FEMtools* has an incorporated solver, an

Ansys interface and driver was used to perform all the static load and modal calculations just to be accordant with the previously presented analysis.

The remainder of this chapter describes the method used to generate the simplified beam model followed by a detailed analysis of the results obtained from different model update methods based on static loading and ground vibration measures. A discussion about the quality of the outputs for each updating case will be presented along the sections.

6.1   Beam Model Generation

The large complexity due to the high number of elements of the original FEM made it impossible to import and work with in the model updating software. As previously mentioned, to solve this problem, a simplified beam model needs to be developed.

Trying to keep the simplified beam model as close as possible to the original FEM of the wing, some characteristics were taken into account in the design of this model. Beam elements with rectangular cross section were used to connect the centroid of 50 wingbox's sections along the span. The reason to choose beam elements is that, even being simple and fast to compute in any FEM solver, they provide high fidelity results. The centroid's coordinates of the wingbox's sections were chosen to better represent the shape, sweep and dihedral angles of the wing over the span keeping also the same coordinate system. It is visible in figure 6.1 the line that connects the 50 points.
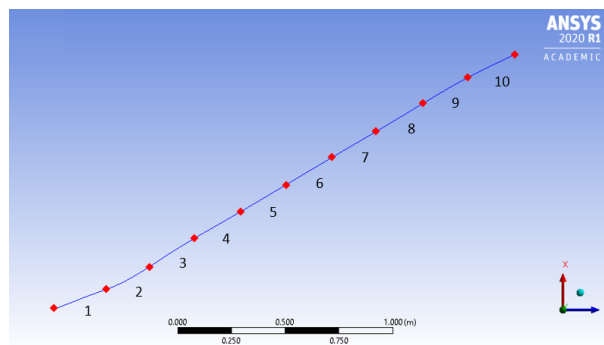
Figure 6.1: Beam FEM developed for the model update.

The boundary conditions in this beam model are implemented by fixing the root node that will represents the 4 holes previously used in the more detailed FEM.

Values of Young's modulus and mass density were defined based in the properties of the constitution material of most of the wing. Young's modulus was defined as 67.1GPa, normal values for the woven carbon fiber composite, and mass density was defined as 2162 Kg/m^3 coming from the update based on preliminary differences of the original model explained in section 3.2.

6.2   Model Updating of the Simplified FEM

In order to achieve a good pairing between responses, the beam model was discretized in 10 equally spaced sections along the span to give to the model more freedom to optimize the parameters in a dis-

tributed way over the span. These sections are numbered as observed in figure 6.1. The Z coordinates gap of each of them is presented in table 6.2.

The beam's FEM and the test model need to be input in *FEMtools* and two correlations are established:

1. A node-point pairing where the nodes of the FEM are associated to the correspondent testing points;

2. A displacement shape correlation where their deformed shapes are correlated.

Throughout the model update process, different parameters were considered depending on the data that is being used to match the responses. Young's modulus and bending moments of inertia were choosen for the update of the stiffness based on static loading tests results. The update of the dynamics of the structure based on GVT results considered all the parameters studied and displayed in the table 6.1. Many iterations were performed varying the number of parameters used for the update to understand which of them are fundamental to converge the responses and which can output more interesting results.

Table 6.1: Parameters studied to update.

Parameters	
Label	**Description**
E	Young's modulus
ρ	Mass density
A	Cross section area
Ix	Bending moment of inertia about x
Iy	Bending moment of inertia about y
Iz	Bending moment of inertia about z
MG	Lumped mass

When performing the automatic model updating, some constants need to be defined in order to achieve a good convergence in responses and overall results. Since the results are not predicted in advance, these constants do not have a correct value associated. For example, a maximum number of iterations was defined as 50 expecting to achieve a fast convergence before reaching this maximum but if in some case the responses were not converged after 50 iterations this value is not enough. The absolute CC target (ϵ_1) was defined as 0.1 intending to achieve high pairing results and a minimum relative CC improvement (ϵ_2) as 0.1 per iteration to certify that the results were converged. If one of this values is achieved, the updating will stop. The minimum parameter change was defined as 0.1% and the maximum parameter change allowed, depending on how easy it is for the software to achieve the convergence, varied between 30% and 1000% per iteration was considered. This value is different for each model update case and it was choosen most of the times by trial and error and selecting the option which outputs best results. The CC used when the responses were displacements from static tests was CCDISP and when the responses were the natural frequencies from the GVT was CCABS. These CCs choice is explained in section 2.4.2.

6.2.1 Preliminary Updates

The first changes on a model updating process start with a manual mass matching between the computational model and the real mass of the wing obtained resorting to a high precision scale. It is also possible at this stage to update manually the area moments of inertia for each section. These values are not a perfect representation of the structure but they can be an initial a good aproximation of the distribution of these parameters along the span.

The bending moments of inertia about each axis and cross section area values were calculated resorting to the follow equations with base and height values of the wingbox obtained in the centroid of each section.

$$Ix = \frac{1}{12}bh^3 - \frac{1}{12}(b-2e)(h-2e)^3 \tag{6.1}$$

$$Iy = \frac{1}{12}b^3h - \frac{1}{12}(b-2e)^3(h-2e) \tag{6.2}$$

$$Iz = Ix + Iy \tag{6.3}$$

$$A = bh - (b-2e)(h-2e) \tag{6.4}$$

Where:

- b is the base length of the wingbox;

- h is the height length of the wingbox;

- e is the defined thickness for the rectangular cross section area, arbitrated as 5mm.

To match the real mass of the wing, a correction factor of 0.625 was applied to all cross section areas in order to keep the distribution over the span and resize the values to obtain the expected mass. The results of all the preliminary manual updates for each section are presented in table 6.2.

Table 6.2: Preliminary manual parameters update.

Section of the wing	Z coordinates interval (m)	Ix (m^4)	Iy (m^4)	Iz (m^4)	A (m^2)	Resized A (m^2)
1	0.57 - 0.78	4.84E-06	2.21E-04	2.26E-04	6.47E-03	4.05E-03
2	0.78 - 0.99	1.27E-06	7.84E-05	7.97E-05	4.57E-03	2.86E-03
3	0.99 - 1.21	8.48E-07	4.61E-05	4.69E-05	3.83E-03	2.40E-03
4	1.21 - 1.42	5.99E-07	3.31E-05	3.37E-05	3.43E-03	2.15E-03
5	1.42 - 1.63	4.35E-07	2.38E-05	2.42E-05	3.07E-03	1.92E-03
6	1.63 - 1.84	3.20E-07	1.63E-05	1.66E-05	2.71E-03	1.69E-03
7	1.84 - 2.06	2.28E-07	7.28E-07	9.56E-07	2.35E-03	1.47E-03
8	2.06 - 2.27	1.40E-07	6.35E-06	6.49E-06	1.98E-03	1.24E-03
9	2.27 - 2.48	8.24E-08	3.47E-06	3.55E-06	1.62E-03	1.01E-03
10	2.48 - 2.70	5.13E-08	1.65E-06	1.71E-06	1.27E-03	7.92E-04

6.2.2 Based on Static Tests Results

After the above mentioned preliminary updates, the beam FEM is closer to the test model but it stills showing significant differences in responses, as presented in the maximum displacements values in figure 6.3. To improve these values, an automatic model update resorting to the *FEMtools* software functionalities will begin to update the stiffness using data from the static tests. The data from the static loading tests that will be used is referred to the third scanning case results correspondent to the 22.5 Kg load applied at the wing tip's aerodynamic center.

Although displacements were collected in different points along all the wing's surface, the displacements measurements were not all used as response because the software showed difference when matching values of diplacements lower than 1cm. For that reason, only points where displacements were higher than 1cm were considered. The pairing between the experimental testing points and the beam FEM was done by associating the 6 points of the same wing section with the closer node of the beam FEM. The overlap of both models used for the model update can be seen in figure 6.2.

For the stiffness update, young's modulus and bending moment of inertia about x and y axis were the chosen parameters to change by reason of being the parameters responsible for the stifness behaviour.
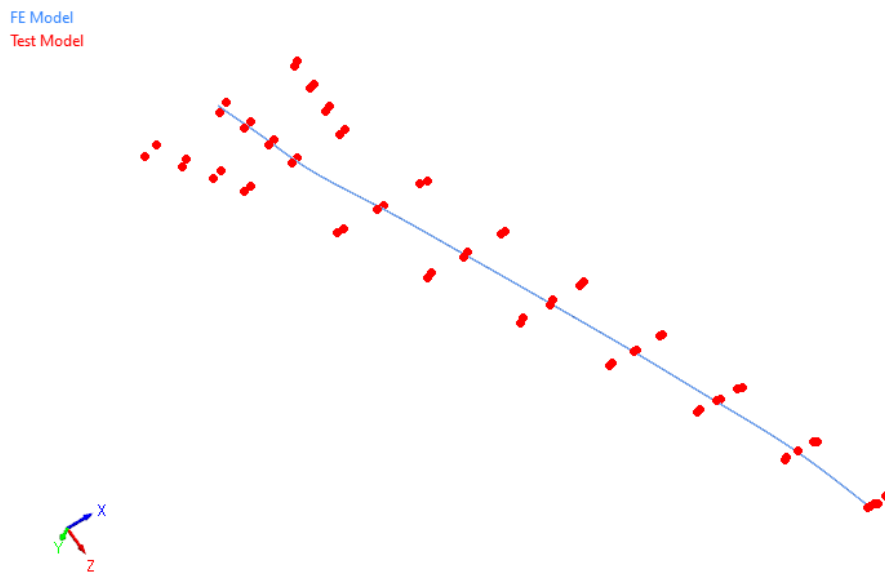
Figure 6.2: Pairing between the simplified FEM and the static loading test points used to perform the model update.

With a maximum parameter change of 1000% per iteration the CCDISP CC converged after 10 iterations in 3,1%, as visible in figure 6.4, which means an average similarity between responses of 96.9 %.

After all the parameters' changes, the improvements of the responses when compared with the experimental results are highlighted in figure 6.3. It is clearly visible, for example in the values obtained on the tip's displacement, that the differences went from 97.8% to 3.1%.

(a) Simplified FEM results preliminary manual parameters' update.

(b) Simplified FEM results after parameters' update based on static tests data.

(c) Static loading tests results.
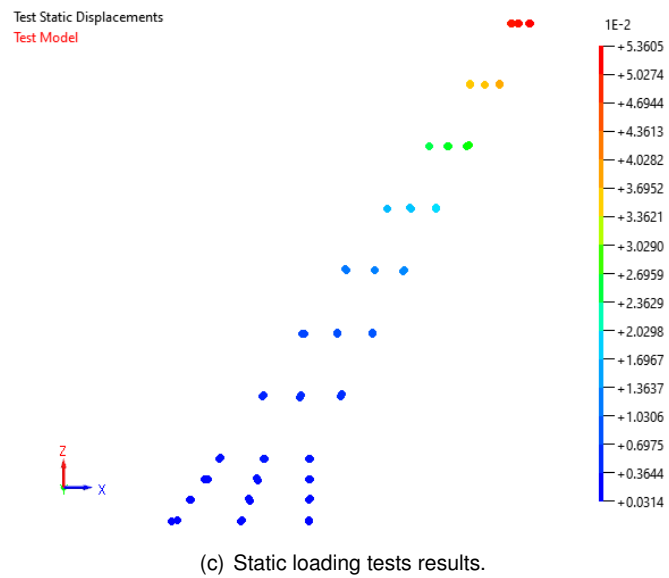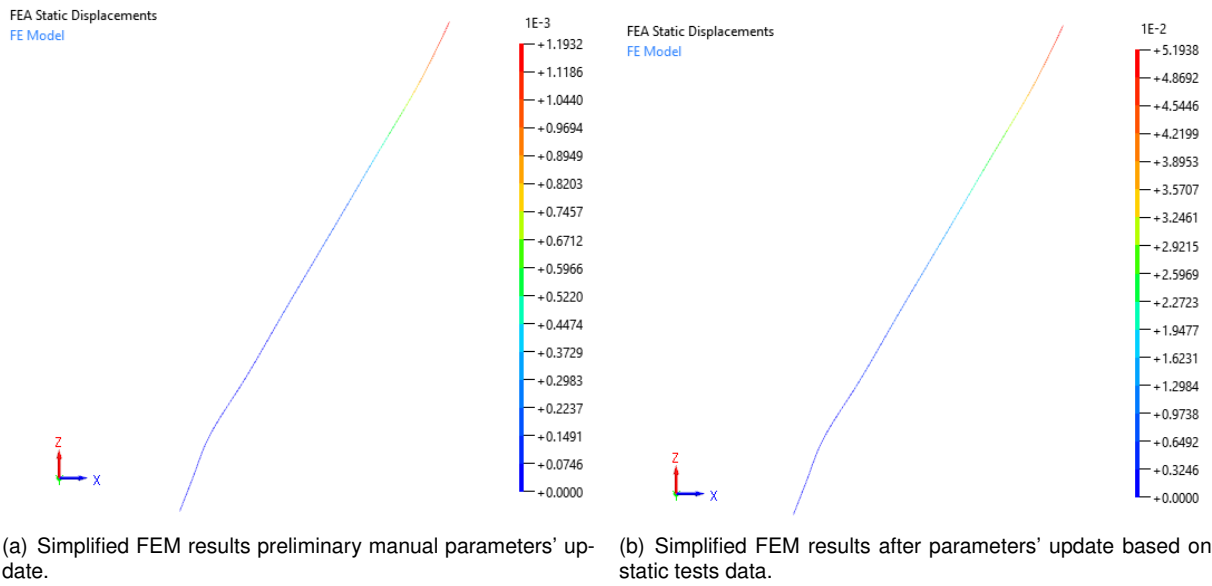
Figure 6.3: Diplacement results comparison between simplified FEM before and after parameters update and static loading test results.

(a) CC CCDISP.

(b) Avergare of the all the displacement responses.
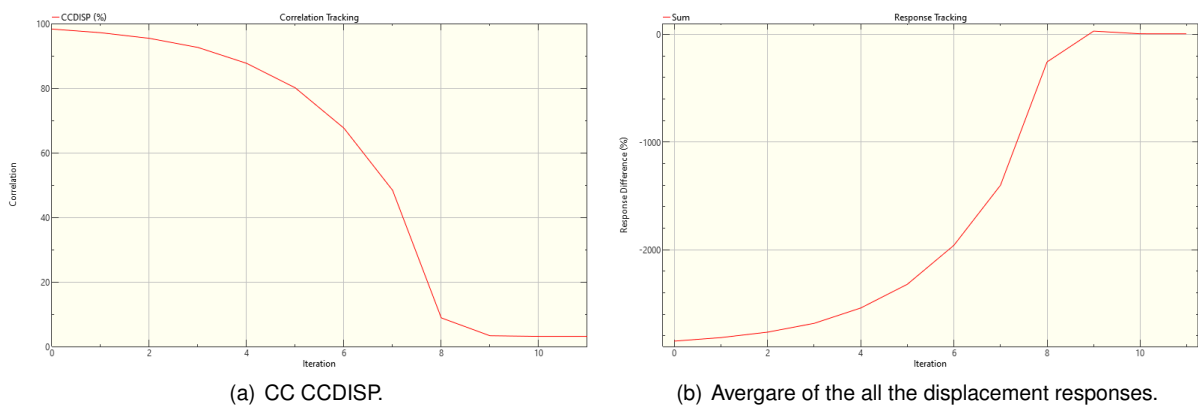
Figure 6.4: Convergence of CC and average responses along the iterations for the first model update based on static load tests data.

60

(a) Young's modulus.

(b) Moment of inertia about x.

(c) Moment of inertia about y.

(d) Differences between initial and updated values.
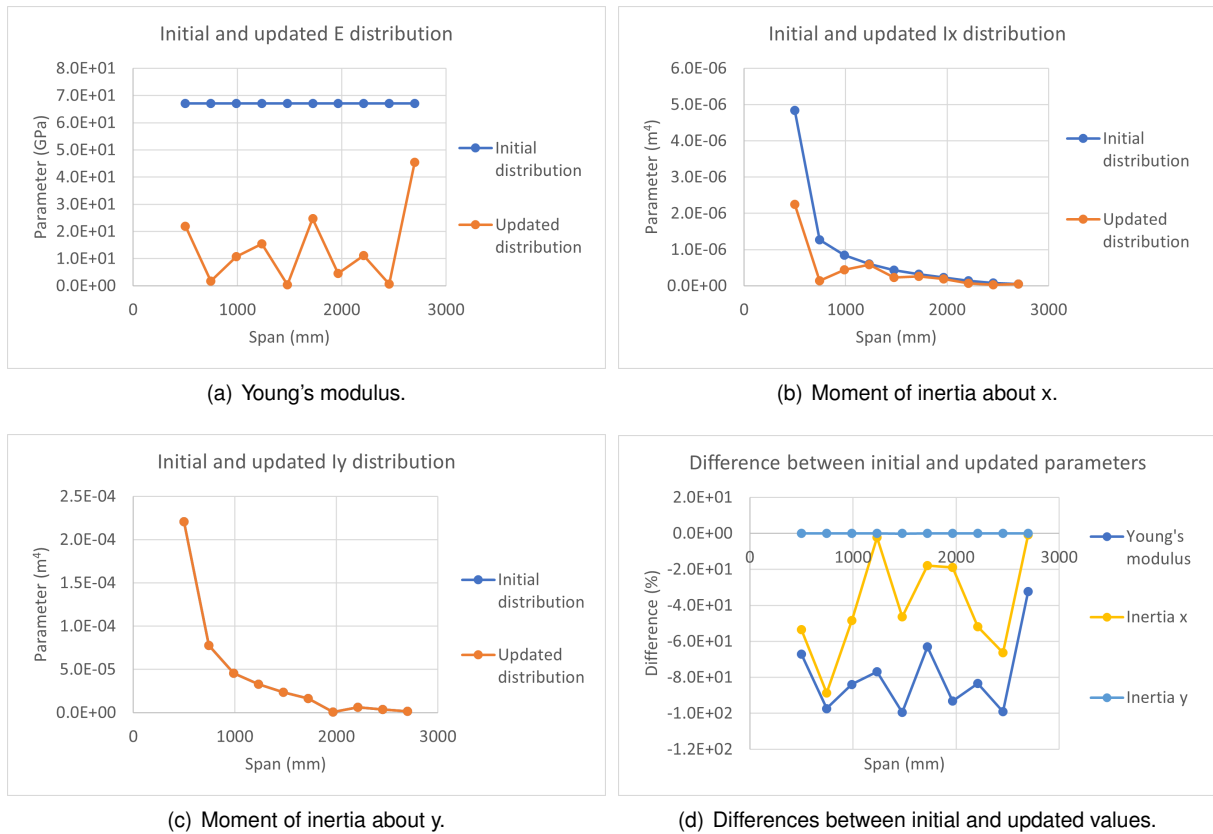
Figure 6.5: Relationship between initial and updated values of parameters for the first model update based on static load tests data.

The parameter changes to obtain these results were significant and are present in figure 6.5. It is important to highlight the differences between initial and updated parameters of Young's modulus in specific sections of the wing that is two orders of magnitude lower. A possible explanation for this fact is that the sensitivy to this parameter is higher than for the moments of inertia. No significant changes can be seen in bending moment of inertia about the y axis, as expected, because the static test considered applied on the aerodynamic center corresponds mainly to an out of plane bending load case.

An attempt was made to update the stiffness and achieve an acceptable correlation using as variables parameters the moments of inertia about x and y axis. When trying to match the displacements along the span the moments of inertia are reduced and required to go lower than 10^{-10}. These low values are interpreted as zero on the FEM solver and no computational results can be calculated.

6.2.3 Based on GVT Results

After updating the beam FEM with the results obtained from the static tests, one can assume a reliable stiffness pairing between computational and real model. It is then time to proceed to the dynamic update, which will resort to the GVT results to match the computational responses. However, along this section, different starting points will be studied for the dynamic update to analyze if the results obtained are similar or, if otherwise, to understand the cause for the difference between them.

In table 6.3, it is possible to visualize how different are the FEA modal results of the beam FEM,

without any update apart from the preliminary moment of inertia and cross section area distributions, when compared with the EMA data obtained from the tests. Firstly, three different model updates will be perfomed starting with this beam FEM, the same used as input on the stiffness update for the static tests data.

Then, four different model updates will be perfomed starting with the updated beam FEM obtained from the stiffness update based on static tests, presented in section 6.2.2. Again, different parameters selection will be explored for each run. This means, starting with values similar to the expected resutls, also visible on table 6.3, that can maybe influence the model update results.

Table 6.3: Natural frequencies comparison between results of original beam model, stiffness updated beam model and experimental results obtained from the GVT.

Mode #	Tests f_{EMA} **(Hz)**	Initial FEM f_{FEA} **(Hz)**	Δ_f **(%)**	Updated FEM f_{FEA} **(Hz)**	Δ_f **(%)**
1	10.30	75.93	637.17	9.59	-6.91
2	35.30	80.93	129.25	15.89	-54.99
3	50.40	215.13	326.85	36.96	-26.66
4	81.30	240.07	195.29	53.76	-33.88
5	130.00	629.04	383.88	90.58	-30.32
6	143.00	633.16	342.77	116.43	-18.58
7	157.00	748.27	376.61	124.79	-20.52

The chosen responses to match to the GVT test results were always the same. The most important are the frequencies obtained from the tests, staring in the first mode till reaching first torsion mode, which is in this case the 6th mode. Thus, frequencies correpondent to the first two in plane modes, first three out of plane modes and the first torsion mode were planned to be matched.

Another response is the total mass of the model. Choosing the total mass as a response, with the value already updated from the begining, all the parameters updated will change the distribution of the mass but always keep the total mass.

6.2.3.1 Starting with the FEM Without Updates

In table 6.3, it is possible to see how different from the test's results are the starting points chosen for the model updates in this section. Three iterations will be studied changing the parameters' selection to find out which one can output the best match:

1. Parameters E, ρ, A, Ix and Iy selected to be updated;

2. Parameters A, Ix and Iy selected to be updated with fixed values of E=67.1GPa and ρ=2162 Kg/m^3;

3. Parameters Ix and Iy selected to be updated with fixed values of E=67.1GPa, ρ=2162 Kg/m^3 and A from the preliminary updates.

The purpose of this study is to understand which parameters are needed to achieve good results. For example, the first case explores total freedom of all the parameters to understand how the model updating acts on each parameter. However, it is assumed that the values of E and ρ should be correct because they are charateriscs of the material used in the manufacture of the test article and, because of that, from the first to the second case, the goal of the analysis is to see if the model update is capable to converge the responses only updating the A, Ix and Iy. In the last case, the goal is to check the differences in Ix and Iy if the A is not updated.

Starting with the first case, where all the parameters (E, ρ, A, Ix, Iy) were taken into account for the process, it can be seen in figure 6.6 that the model converged in 10 iterations even if starting with such different natural frequencies when compared with tests results. The CC CCABS achieved impressive results and the responses' differences between FEA and EMA converged in an average values of 99.9% of similarity.

(a) CC CCABS.   (b) Avergare of the 7 responses.
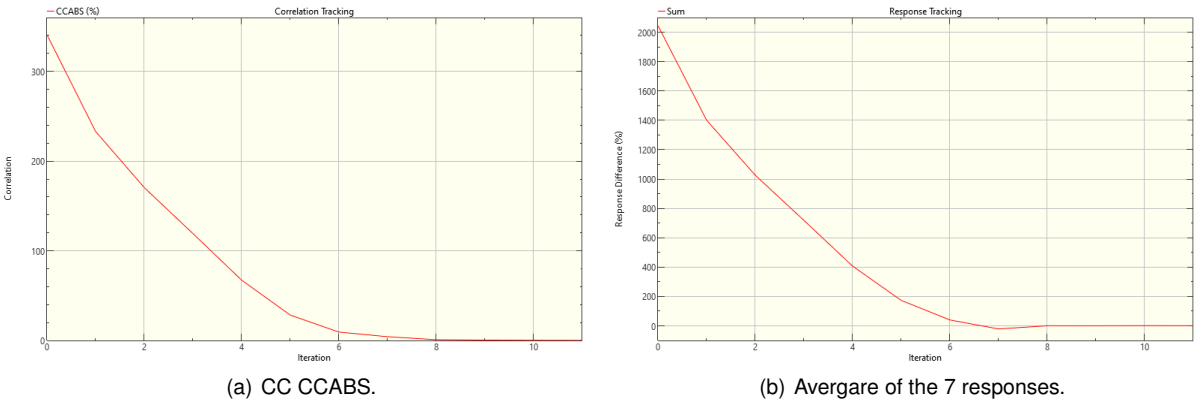
Figure 6.6: Convergence of CC and average responses until the iteration # for the first model update based on GVT data starting from the initial FEM.

In order to achieve this pairing, some parameters were changed significantly. Results of the parameters modifications are presented in figure 6.7. Differently from the stiffness update, most of the young's modulus values obtained have the same order of magnitude as the initial value. Changes in mass distribution for the frequencies' pairing peaks in density in two points. These peaks and the density distribution as a whole is similar to the area distribution, reinforcing the trend of mass concentration in the referred points. The Ix distribution is not significantly changed apart from the root region. This part, together with the reduction in E at the root suggests an excessively stiff root initially. Overall, the sensitivity to the mass related parameters and E seem to be high, when it comes to matching the natural frequencies as could be expected.
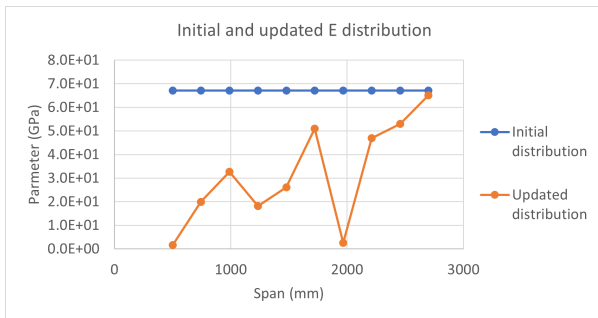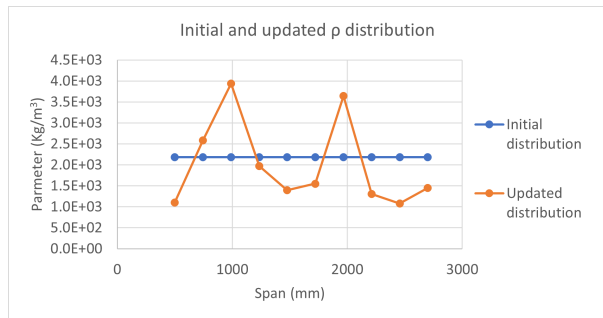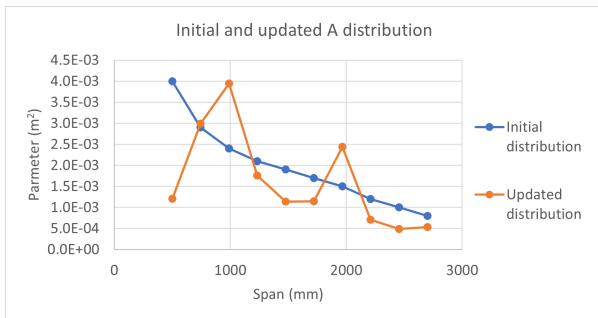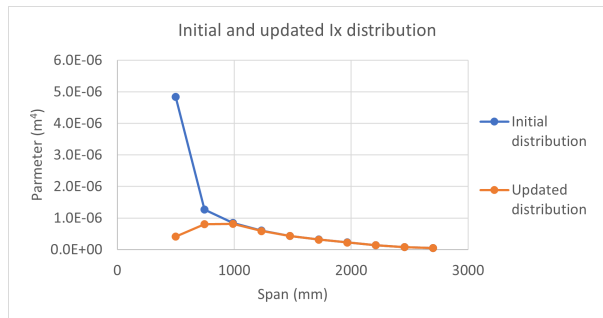
63

(a) Young's modulus.

(b) Mass density.

(c) Cross section area.

(d) Moment of inertia about x.
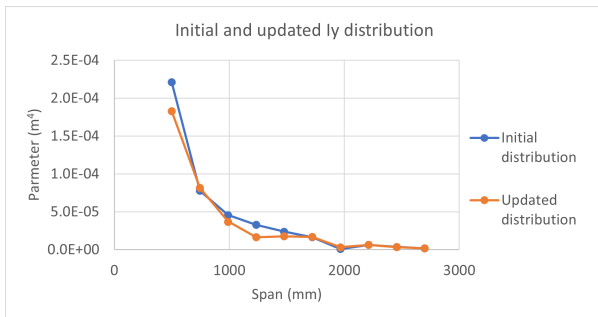
(e) Moment of inertia about y.
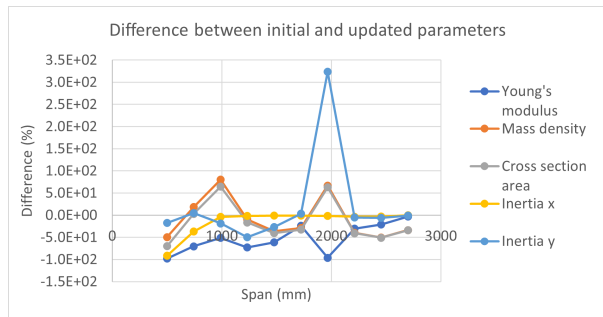
(f) Differences between initial and updated parameters values.
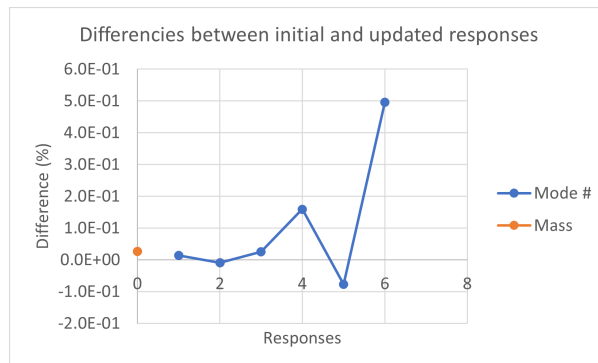
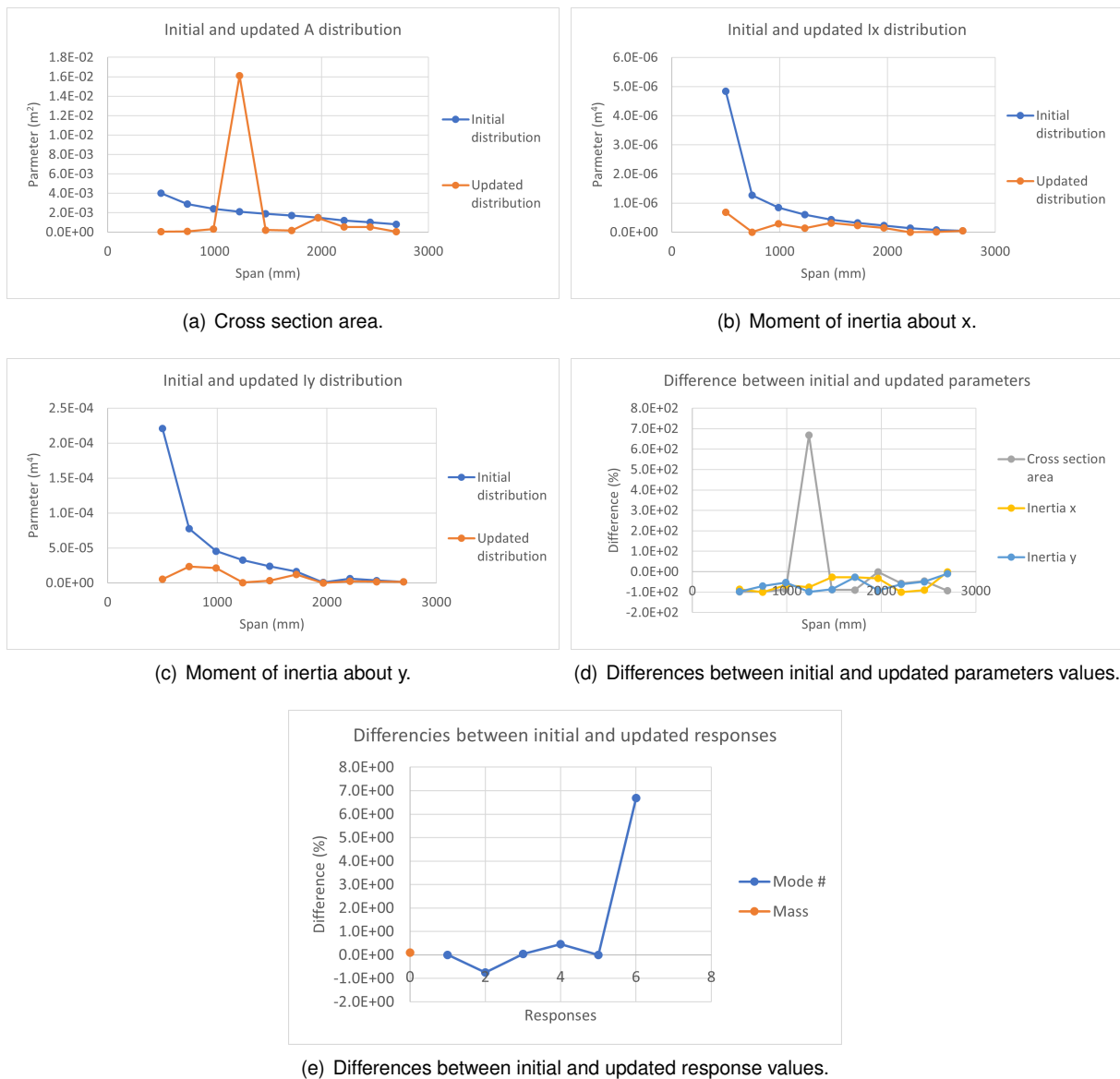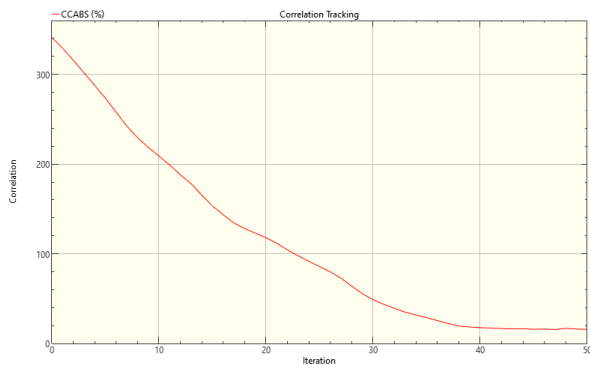(g) Differences between initial and updated response values.

Figure 6.7: Relationship between initial and updated parameters (E, ρ, A, Ix, Iy) and responses for the first model update based on GVT data starting with the beam FEM without updates.

The second model update based on the GVT results sets E and ρ as a constant parameters with original values of 67.1GPa and 2162 Kg/m^3, respectively.

It is possible to see in figure 6.8 that this time the convergence of the procedure required more iterations comparing with the 10 iterations from the first update, the CCABS needed around three times more iterations to converge for this second case. However, it kept showing accurate results of pairing with an average similarity between responses of 98.7%.


(a) CC CCABS. (b) Avergare of the 7 responses.
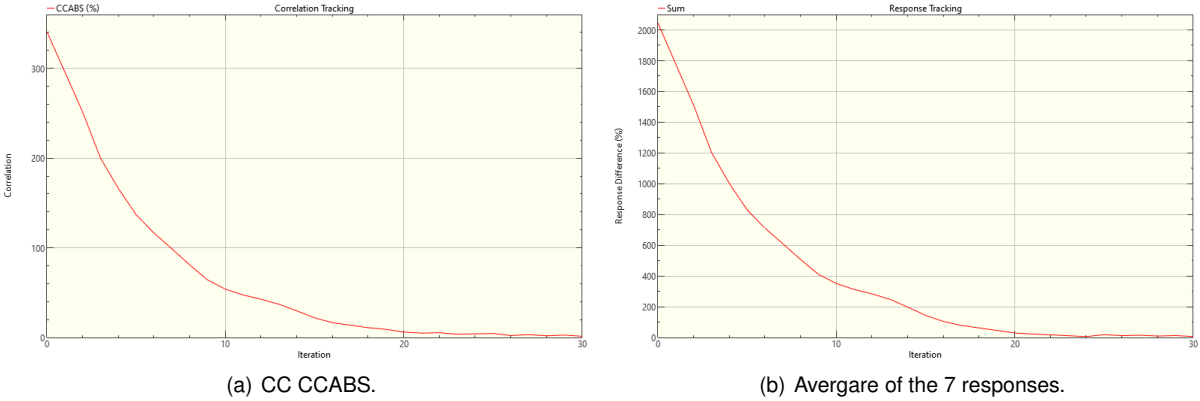
Figure 6.8: Convergence of CC and average responses with the iteration # for the second model update based on GVT data.

Without changing the Young's modulus, some parameters changes were higher than before and can be visible in figure 6.9. The group of elements near the 1250mm station concentrates most of the mass of the wing. In the absence of suitable constraints, the software iteratively changes the values of parameters in order to match the responses and to obtain good results the mass needs to be around that area.

The matching between the responses was satisfactory achieved with the first torsion mode frequency difference of 7%, corresponding to 11Hz of disparity.

(a) Cross section area.

(b) Moment of inertia about x.

(c) Moment of inertia about y.

(d) Differences between initial and updated parameters values.

(e) Differences between initial and updated response values.

Figure 6.9: Relationship between initial and updated parameters (A, Ix, Iy) and response values for the second model update based on GVT data starting from the initial FEM.

A third model update was performed to evaluate what values of similarity between computational and experimental models can be reached only resorting to bending moments of inertia changes. It is not expected to obtain outstanding results because the mass distribution can not be updated without changing ρ or A.

As can be seen in figure 6.10, the convergence of CCABS criterion took 50 iterations and the average value of similarity between frequencies' responses was 84.3%. This may seen like a reasonable outcome in general but, looking at the parameters changes and responses differences presented in figure 6.11, the frequencies of the second and the sixth mode show a difference of 29.1% and 55.3%, respectively. Differences of up to 100% in the bending moment of areas of some sections were not enough to match accurately the natural frequencies.

It can be that results from the model update without allowing changes to the distribution of mass can not accurately update the dynamic behaviour of the structure.

(a) CC CCABS.
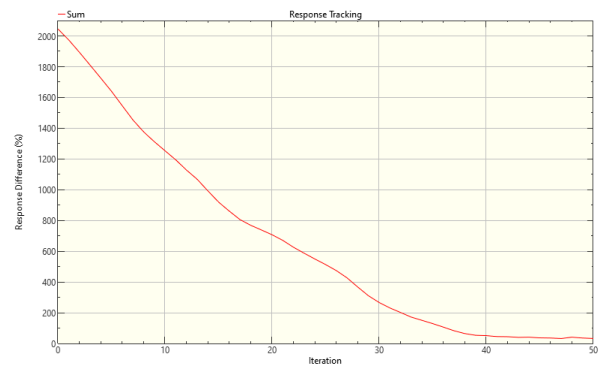
(b) Avergare of the 7 responses.

Figure 6.10: Convergence of CC and average responses with the iteration # for the third model update based on GVT data starting from the initial FEM.
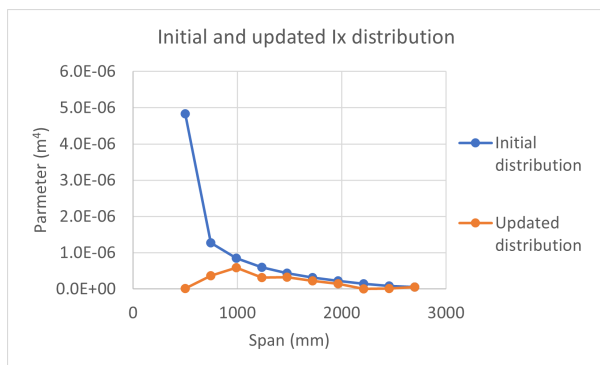
(a) Moment of inertia about x.
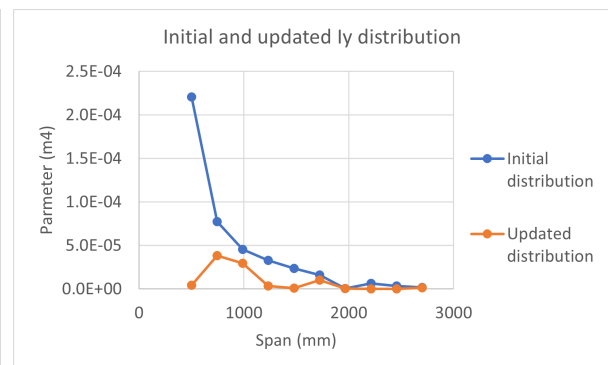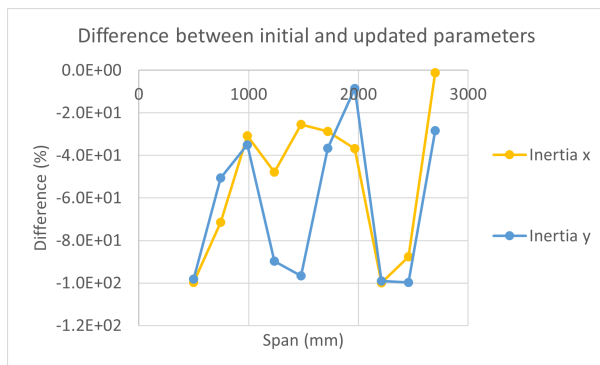
(b) Moment of inertia about y.

(c) Differences between initial and updated parameters values.
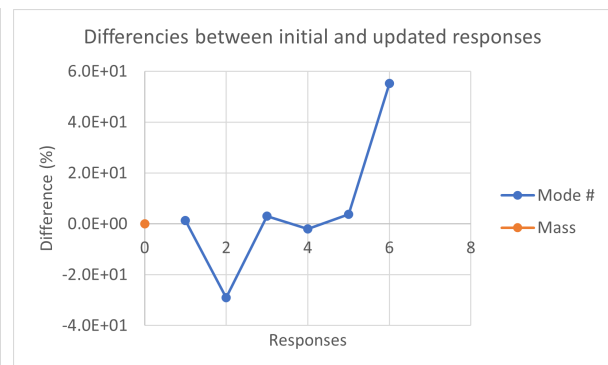
(d) Differences between initial and updated response values.

Figure 6.11: Relationship between initial and updated parameters (Ix, Iy) and response values for the third model update based on GVT data starting from the initial FEM.

6.2.3.2   Starting with the Stiffness Updated FEM Based on Static Tests Results

This section will present a study of the differences in results doing the same process as previously, but starting the model update with a stiffness updated FEM based on static tests results.

In table 6.3, a comparison was previously presented between the natural frequencies results obtained from the EMA and from the stiffness updated beam's FEA. These values when compared with the beam model without any update showed a remarkable improvement in dynamic similarity, even thought without any type of update based on experiemntal modal results.

Four cases will be studied, changing the parameters' selection to find out which one can output the best match:

1. Parameters E, ρ, A, Ix and Iy selected to be updated starting with the FEM resulting from the stiffness update;

2. Parameters A, Ix and Iy selected to be updated starting with Ix and Iy values resulting from the stiffness update. Fixed E=67.1GPa and ρ=2162 Kg/m^3;

3. Parameters A, Ix and Iy selected to be updated starting with E, Ix and Iy values resulting from the stiffness update. Fixed ρ=2162 Kg/m^3;

4. Parameters Ix and Iy selected to be updated starting with E, Ix and Iy values resulting from the stiffness update. Fixed ρ=2162 Kg/m^3 and A to the preliminary updates.

The purpose of this study is to understand how the stiffness update affects the results of the model update, exploring again different parameters' selection options. For example, the first case explores total freedom of all the parameters to understand how the model update behaves for each parameter. From the first to the second case, the goal of the analysis is to see if the model update is capable to match the responses only updating the A, Ix and Iy. The third case explores the difference between using E as starting point from the stiffness update or fixed as 67.1 GPa. Finally, on the last case, the goal is to check if, starting from the stiffness updated FEM, the model can converge without the need of using A to change the mass distribution.

Starting with the first case, where all the parameters (E, ρ, A, Ix, Iy) were taken into account for the process, it can be seen in figure 6.12 that the model converged in just 4 iterations. This is indicative of the improvement of starting with a FEM closer to the actual test article.

The CC CCABS achieved matching results and the responses' differences between FEA and EMA converged in an average values of 99.9% of similarity, as it also happened in the first model update case starting with the FEM without updates. Comparing both first's model updating cases with different starting FEMs, at this point no major improvements are visible apart the number of iterations it took to converge.

Results of the parameters modifications are presented in figure 6.13 and instantly differences can be seen. The young's modulus has not changed significantly, which means that the stiffness update results can be confirmed when pairing with GVT data. Relative to mass distribution some parameters' changes

(a) CC CCABS.

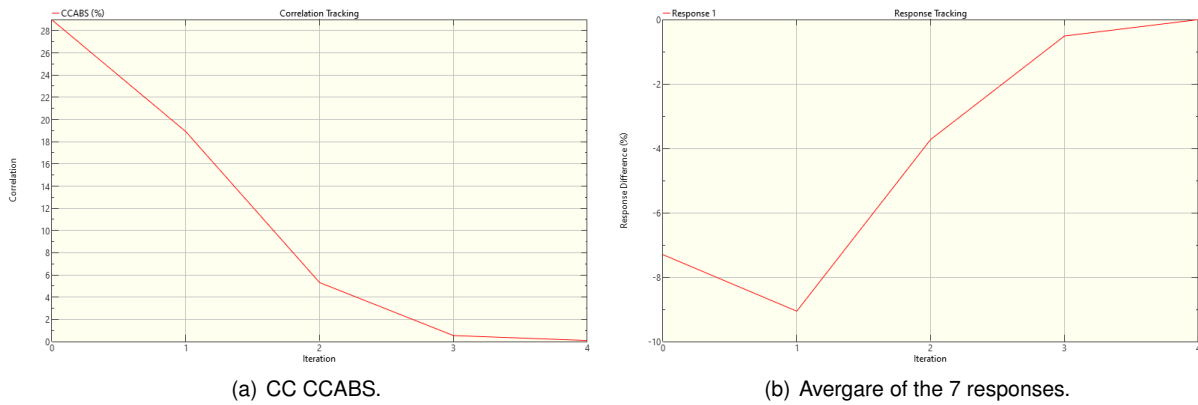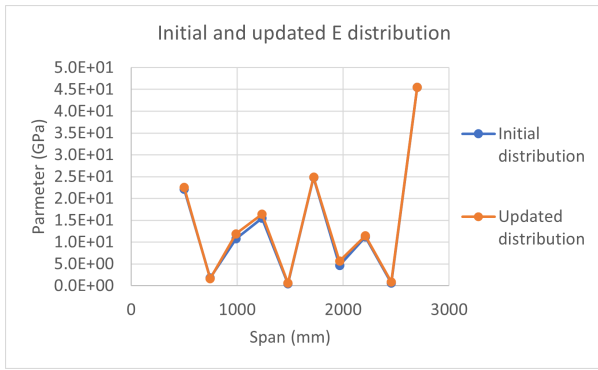
(b) Avergare of the 7 responses.

Figure 6.12: Convergence of CC and average responses with the iterations for the first model update based on GVT data starting with the stiffness updated FEM.

can be observed but of significantly lower magnitude when compared with the sections of high mass present in the last section 6.2.3.1. The higher percentual differences are now present on the bending moment of inertia about Y axis, although not deemed as very significant given the lack of sensitivity to this parameter observed previously.

Apart from the differences, it seems clear that this first model update starting with the stiffness updated FEM shows a more reasonable final output, without the mass concentration in one or two sections and an almost perfect match between the FEA and EMA.

Comparing figure 6.14 for the second model update with figure 6.15 for the third model update it is visible again a different change in the number of iterations to converge. As long as the parameters are closer to a good solution it is much easier to quickly achieve good CCABS correlation values. When looking to the averaging responses differences, the improvements of using the updated model as starting point begins to be evident. The values obtained when A, Ix and Iy are chosen to be updated are 96.6% for the second case contrasting with the 99.9% for the third case. It is an apparently small difference but when analysing the responses difference for each mode separately, as it is showed in the last graphic of figure 6.16 and 6.17, it is the difference between having a significant error in the pairing of the last mode versus doing a perfect match of all the modes in study.

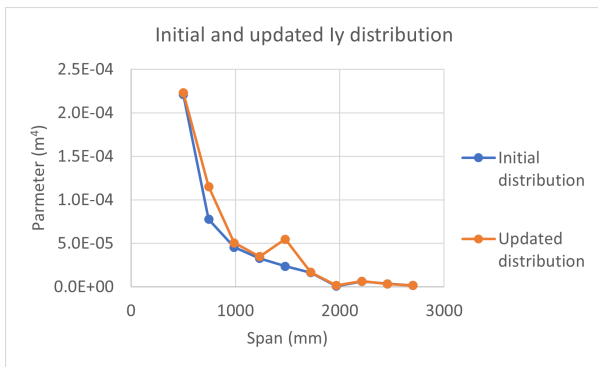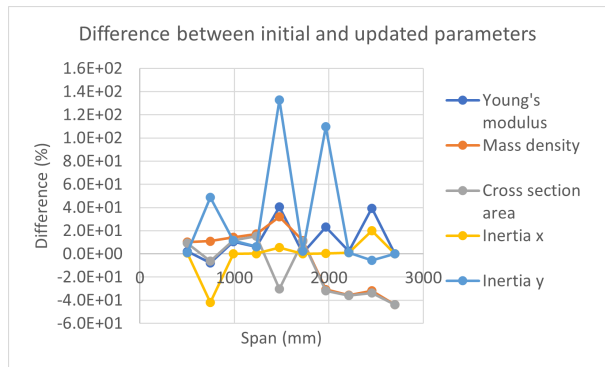(a) Young's modulus.
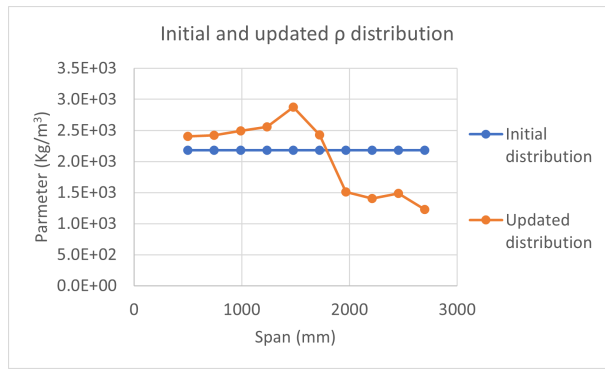
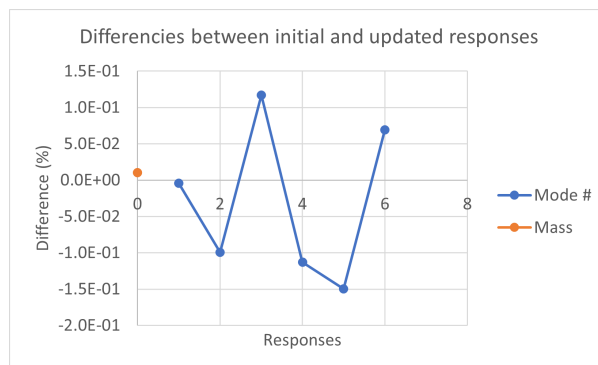(b) Mass density.
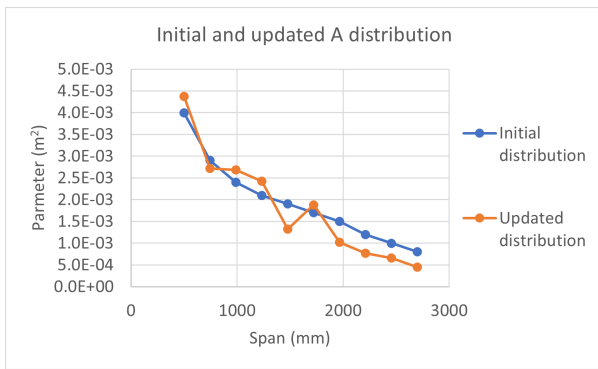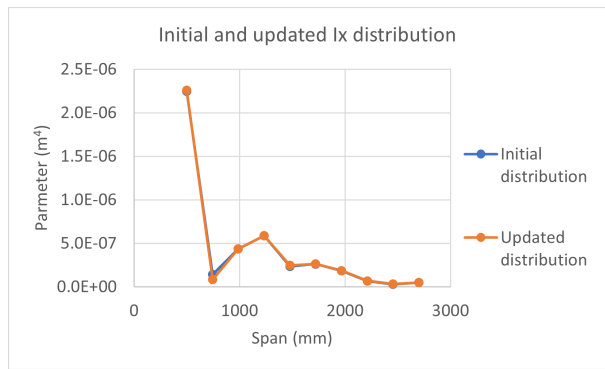
(c) Cross section area.

(d) Moment of inertia about x.
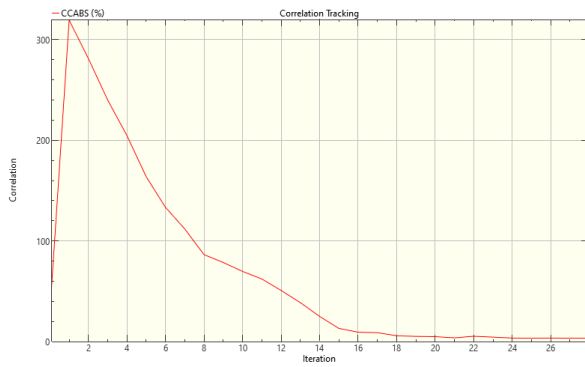

(e) Moment of inertia about y.

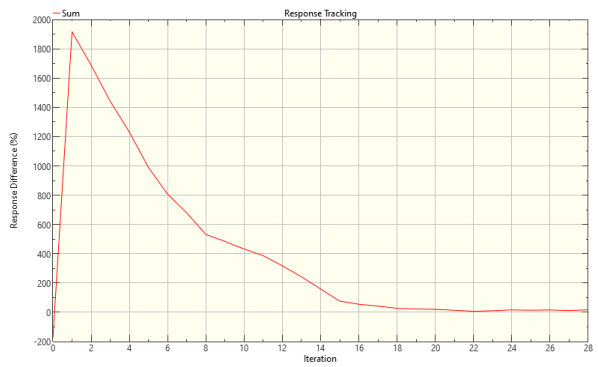(f) Differences between initial and updated parameters values.

(g) Differences between initial and updated response values.

Figure 6.13: Relationship between initial and updated parameters (E, ρ, A, Ix, Iy) and response values for the first model update based on GVT data starting with the updated FEM.
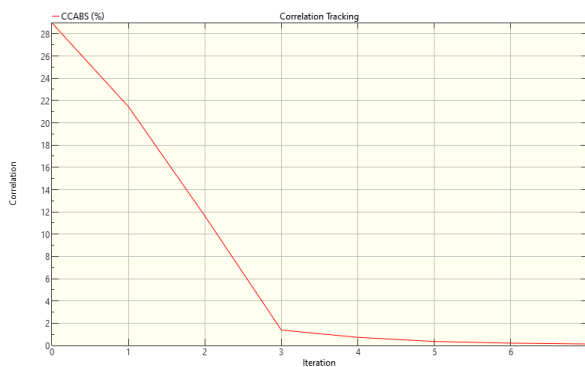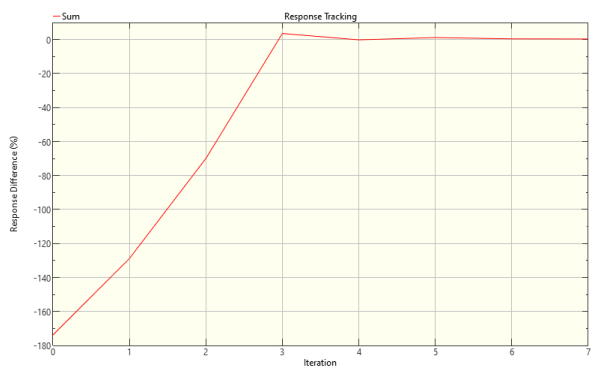
(a) CC CCABS.

(b) Avergare of the 7 responses.

Figure 6.14: Convergence of CC and average responses with the iteration # for the second model update based on GVT data starting with the Ix and Iy updated distribution.


(a) CC CCABS.

(b) Avergare of the 7 responses.

Figure 6.15: Convergence of CC and average responses with the iteration # for the third model update based on GVT data starting with the updated FEM.

Similar differences between the second and third model update can be found as in the updates in the previous section when fixing a constant E, the solution found shows higher magnitude changes and mass peaks, along with worse matching of the sixth mode.
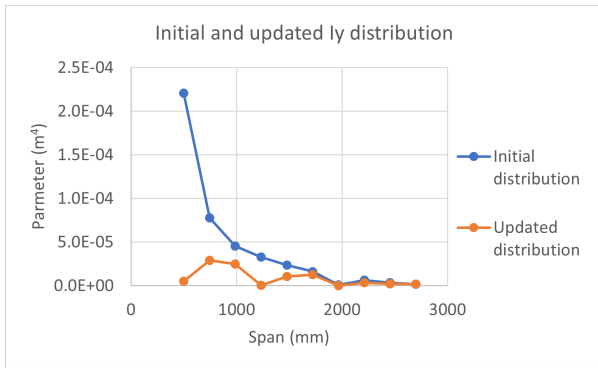
When using the stiffness updating, E distribution lower magnitude adjustments can be seen and a better matching of the sixth frequency obtained.
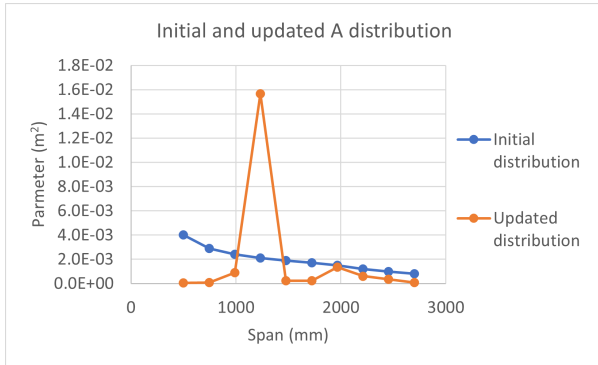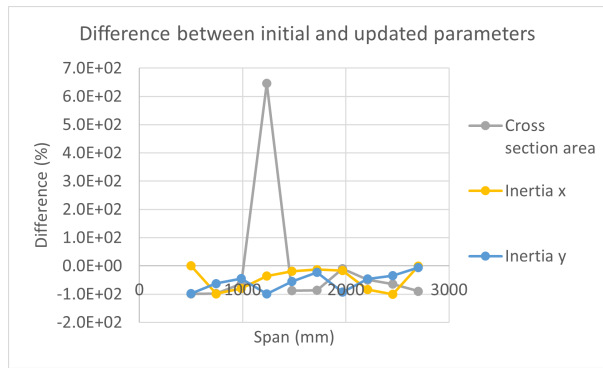
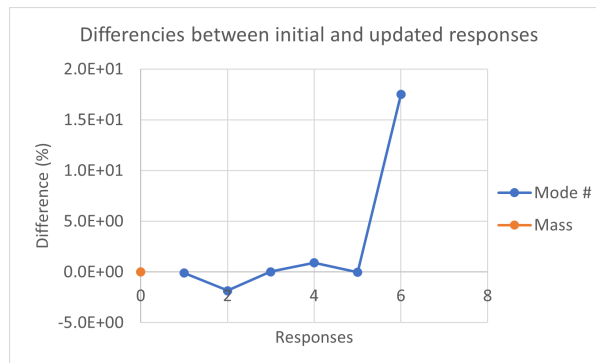(a) Cross section area.
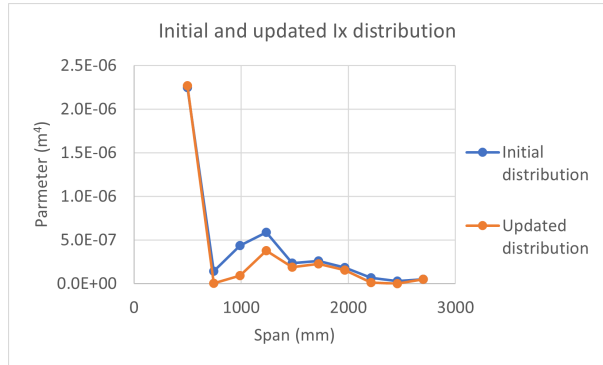
(b) Moment of inertia about x.
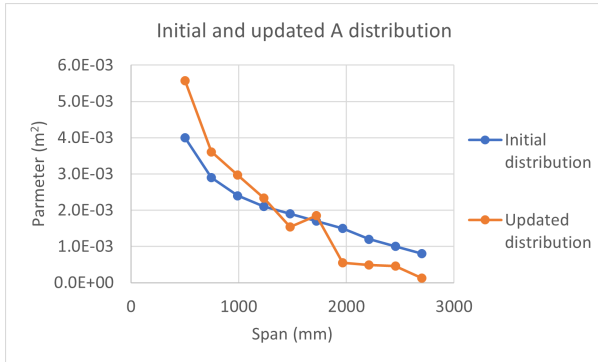

(c) Moment of inertia about y.
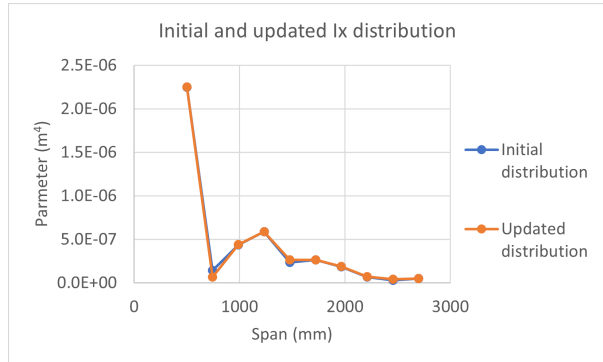

(d) Differences between initial and updated values.

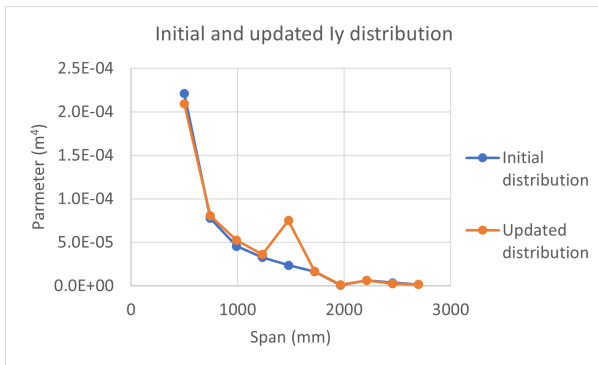(e) Differences between initial and updated response values.

Figure 6.16: Relationship between initial and updated parameters (A, Ix, Iy) and response values for the second model update based on GVT data starting with the Ix and Iy updated distribution.
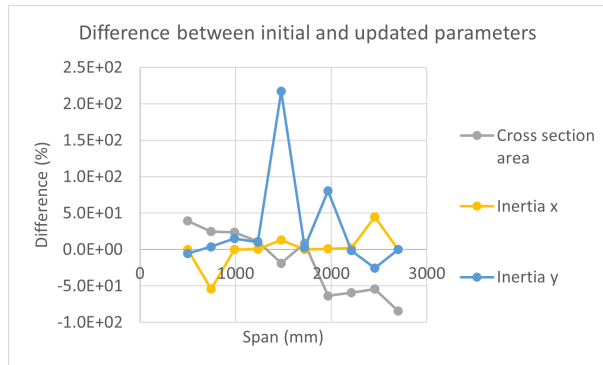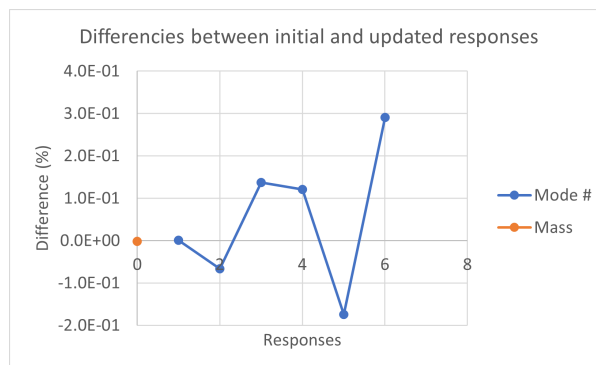
(a) Cross section area.

(b) Moment of inertia about x.

(c) Moment of inertia about y.

(d) Differences between initial and updated parameters values.

(e) Differences between initial and updated response values.

Figure 6.17: Relationship between initial and updated parameters (A, Ix, Iy) and response values for the third model update based on GVT data starting with the updated FEM.

It was seen in the third model update of the last section that the final results were not satisfactory. For that reason, this last and fourth model update was performed to evaluate if better responses matching could be achieved without changing the mass distribution of the FEM if the starting points was closer to the expected outcome FEM. To do this, only Ix and Iy parameters will be selected for the update fixing all the other parameters. As a starting point, the file used was the final output of the stiffness FEM updated based on the static tests data.

As it can be seen in figure 6.18, the convergence of CCABS criterion did not take long to converge. An improvement in the responses' matching exists but the matching is not perfect, 90.1% compared with the 84.3% obtained starting with the not updated model. Looking at the parameters changes and responses differences presented in figure 6.19, the frequencies of the first, third and fifth modes show a difference of 15.3%, 15.97% and 18.93%, respectively. These differences are not particularly high. However, they require very significant changes on the bending moment of areas in some sections.

(a) CC CCABS.　　　　　　　　　　　　　　(b) Avergare of the 7 responses.
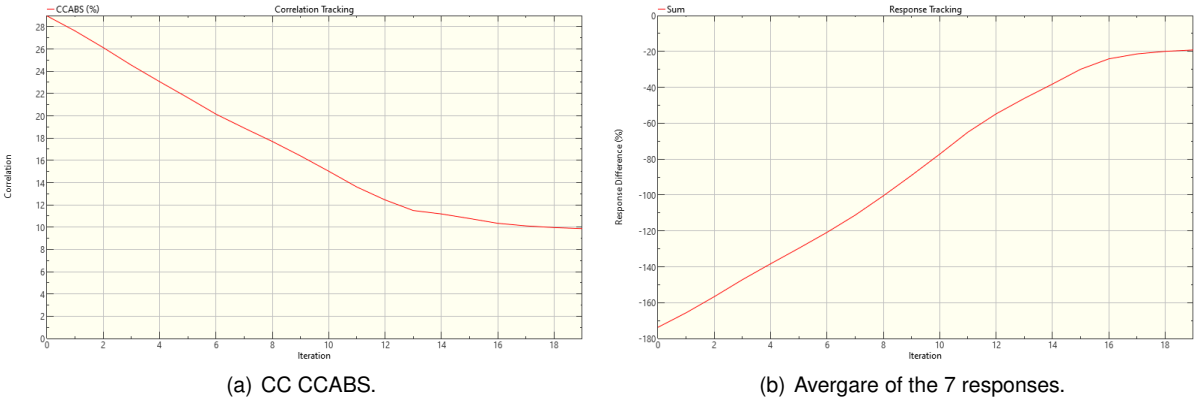
Figure 6.18: Convergence of CC and average responses along the iterations for the fourth model update based on GVT data starting with the updated FEM.
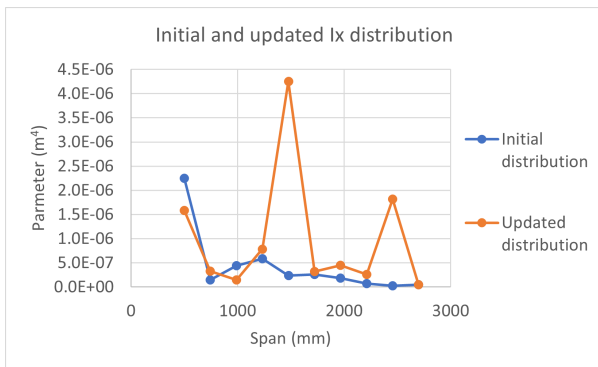
(a) Moment of inertia about x.
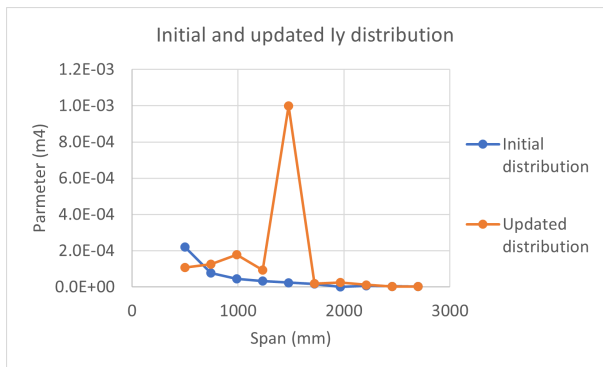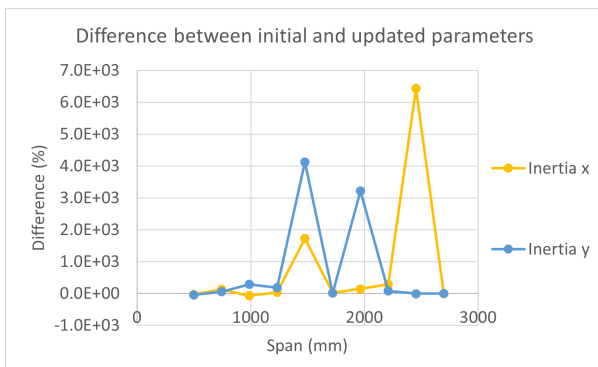
(b) Moment of inertia about y.

(c) Differences between initial and updated parameters values.
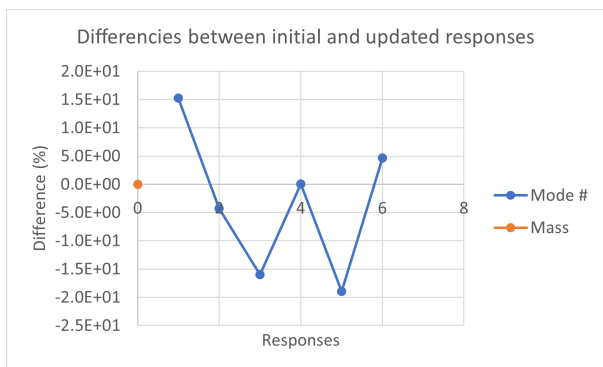
(d) Differences between initial and updated response values.

Figure 6.19: Relationship between initial and updated parameters (Ix, Iy) and response values for the fourth model update based on GVT data starting with the updated FEM.

6.2.3.3 MAC Update

After the successful matching of the frequencies, a MAC analysis was performed to try to pair the mode shapes. Starting with the already updated FEM with 99.9% of similarity in displacements and frequencies, the first approach to update the MAC was to use the same process used for the frequencies.

With a future aeroelastic stability calculation in mind, it is important to match correctly the first bending and torsion modes and for that reason, the MAC of these modes was the response chosen. Firstly, using the same parameters as before (E, ρ, A, Ix, Iy), no improvements were achieved. The software was not able to compute due to the disproportion of the shapes and stopped working after the first iteration.

In order to solve this problem, 11 mass points in the tips of each wing sections were added to give freedom for the model to adapt each mode. Performing the model update with this new model, Mx, My and Mz parameters were added, representing the lumped mass in direction x, y and z, respectively. This would let the model to totally change the mass distribution along the wing. It was also used as parameter the bending moments of inertia to allow small stiffness adjustments if needed. The CC used was the CCTOT that includes all the others mass, frequencies and MAC CC.

Figure 6.20: Beam FEM with mass points.

After numerous tries with different starting points neither the responses or the CC converged in a reasonable value. These values should get closer to zero but, as visible in figure 6.21, values lower than 80% were never obtained.

These results suggest that, for the MAC matching between experiments and computation, higher FEM complexity is required.

<div align="center">(a) CCTOT CC.</div> <div align="center">(b) MAC response of the first torsion mode.</div>
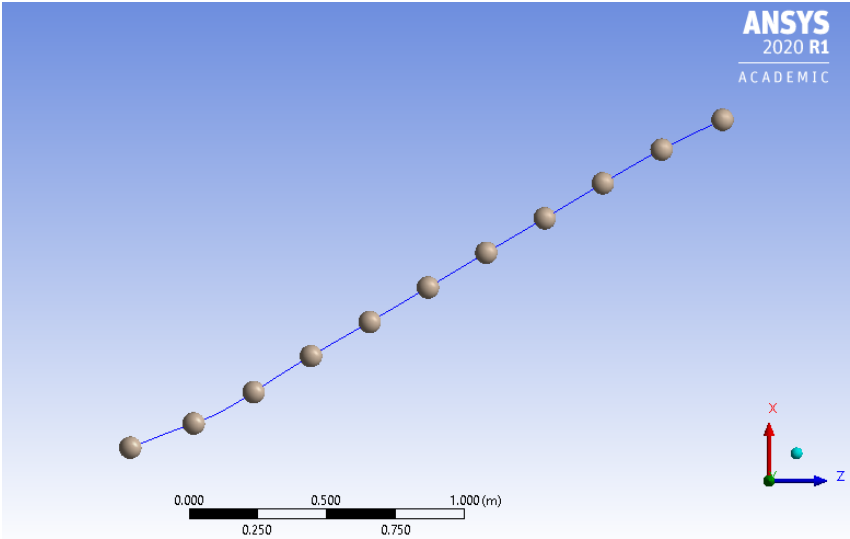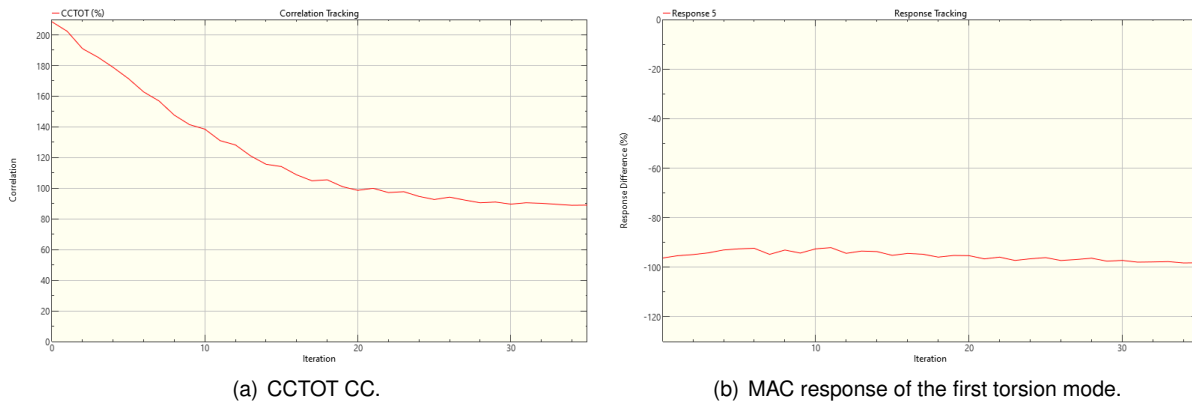
<div align="center">Figure 6.21: Convergence of CC and example of a MAC response with the iteration #.</div>

6.3 Final Model Results

From the previously obtained results based on GVT, three different model updates achieved a convergence metric of 99.9% similarity between responses and mass of computational and experimental models. In order to choose which one of these describes better the real wing behaviour, these three cases of model updates were submitted to the static analysis used for the stifness update.

It may seem redundant once the stiffness update was already performed but, along the model update based on GVT, there were some parameters modifications and for that reason the results could have changed significantly. A 225N load was applied at the tip of the beam's FEM for each updated model and the results are presented in the table 6.4.

Table 6.4: Comparison of static load maximum deflections with a 225N force at the tip between the successfully updated models based on GVT.

Model Update #	Computational max. displacement (cm)	Test max. displacement (cm)	Difference (%)
Case 1 starting without updates	4.51	5.36	-15.89
Case 1 starting with updated FEM	6.08	5.36	13.36
Case 3 starting with updated FEM	7.34	5.36	36.93

Among all the FEMs obtained, the FEM that better represents the real wing's behaviour is the case where the parameters chosen to change are the E, ρ, A, Ix and Iy starting with the stiffness updated model obtained based on static load test resutls. This updated FEM presents a good final stiffness update and a perfect match between all the natural frequencies in study and for that reason, this should be the starting point for any future improvements.

<div align="center">77</div>

Chapter 7

Conclusions and Future Work

This last section presents the achievements of the work perform along this document followed by the main conclusions about the topic, where important procedures and considerations are reviewed. Finally, some suggestions are presented for a future work.

7.1 Achievements

This document propose to perform a static and dynamic characterization of a scaled BWB UAV and answer if static loading tests could be enough to validate a FEM in order to avoid performing GVT that are expensive. The goals were successfully achieved starting with the a FEA followed by the experimental work, static tests measurements that characterized the stiffness and GVT measurements that correlated the modal dynamics of the wing. Looking at the results, it was obvious the disapproval about the previous question.

A beam model was generated and a study on the model updating process of a FEM was performed varying the chosen parameters. Different models that accurately represent the behaviour of the structure were obtained. However, some difficulties were found when trying to match the mode shapes of the structure.

7.2 Conclusions

The main objective of this work is to characterize the dynamics behaviour of the wing. First, deviations in the mass estimations were estimated to be in excess of 25% that was not accounted for in the model. These differences are attributed mainly to the filleting used to increase the bonding area between skin and spars and ribs as well as to the final glassing of the whole internal wing surface although in much less significant degree.

Starting with the static loading tests, expecting to reach 30% or more of deflection with maximum operational load corresponding to a 2.5g's manoeuvre, it was concluded that the manufactured wing is significantly stiffer than the numerical model prediction. The expected vertical displacement at the wing tip is around 40% different when compared to the experimental results. The experimental wing

curvature shows consistently higher values along the wing span than the ones obtained using the computational static. Changing the load application point from the trailing edge to the leading edge also slightly increases the displacement. This was verified both in the FEM and the experimental results.

The twist tends to invert the trend in areas closer to the wing tip as the loading application point is moved towards the leading edge. There is a pattern captured by the FEM that is also visible in the experimental results, although with a different magnitude. It also shows that the torsional stiffness of the wing is under-predicted by the FEM. In conclusion, the significant increase in structural mass is followed by a significant increase in torsional and bending stiffness of the wing.

Since GVT is more time consuming and expensive than a static load test, one of the main goals of ground structural testing was to prove, when comparing the results of both tests, if it is reliable to validate the FEM only resorting to static loading tests. It was expected to find differences in the same order of values when comparing GVT results with modal FEA, however, the average differences between experimental and computational natural frequencies is approximately 8.9%. The mode shapes obtained correspond with the expected ones obtained from the modal FEA.

This difference between static results and GVT's results totally disprove the previous hypothesis. Having an increase in the stiffness of the wing have not affected that much the modal response. With this, it is imperative to perform both tests without the possibility of using one to replace the other.

The generation of a simplified model and associated model updating varying the selected parameters shows that three different model updates achieved a convergence metric of 99.9% similarity between dynamic responses and mass of computational and experimental models. These accurate values were achieved giving to the model update freedom to change stiffness and density distribution parameters.

Among all the FEMs obtained, the FEM that better represents the real wing behaviour is obtained starting with the stiffness updated model obtained based on static load test results. This updated FEM presents a good final stiffness update and a perfect match between all the natural frequencies in study and for that reason, this should be the starting point for any future improvements. However, some difficulties were found when trying to match the mode shapes of the structure. A hypothesis that may justify this event may come from the material considered that, despite being orthotropic, there was only the possibility to change the values of the Young's Modulus corresponding to the direction of the fibers, for example. It can impair the ability to successfully characterize the torsion of the structure compromising the results when trying to perform MAC-based updates.

7.3 Future Work

A continuation of this work can go through generating a more complex and elaborated FEM, without compromising the capabilities of the software, but that is capable of improving the matching of the mode shapes. A suggestion for this process can be to change the type of elements used to create the simplified FEM.

Once this perfect matching is achieved, aeroelastic flutter calculations can be performed to study the dynamic instabilities of the wing.

Bibliography

[1] Z. CHEN, M. ZHANG, Y. CHEN, W. SANG, Z. TAN, D. LI, and B. ZHANG. Assessment on critical technologies for conceptual design of blended-wing-body civil aircraft. *Chinese Journal of Aeronautics*, 32(8):1797–1827, 2019. ISSN 10009361. doi: 10.1016/j.cja.2019.06.006. URL `https://doi.org/10.1016/j.cja.2019.06.006`.

[2] N. Qin, A. Vavalle, A. Le Moigne, M. Laban, K. Hackett, and P. Weinerfelt. Aerodynamic considerations of blended wing body aircraft. *Progress in Aerospace Sciences*, 40(6):321–343, 2004. ISSN 03760421. doi: 10.1016/j.paerosci.2004.08.001.

[3] S. L. Yang, M. A. Page, and E. J. Smetak. Achievement of NASA new aviation horizons N+2 goals with a blended-wing-body X-plane designed for the regional jet and single-aisle jet markets. In *AIAA Aerospace Sciences Meeting, 2018*, number 210059, 2018. ISBN 9781624105241. doi: 10.2514/6.2018-0521.

[4] M. Sanayei, A. Khaloo, M. Gul, and F. N. Catbas. Automated finite element model updating of a scale bridge model using measured static and modal test data. *Engineering Structures*, 102:66–79, 2015. ISSN 0141-0296. doi: 10.1016/j.engstruct.2015.07.029. URL `http://dx.doi.org/10.1016/j.engstruct.2015.07.029`.

[5] S. Warwick, M. Bras, J. Richards, and A. Suleman. Measurement of Aeroelastic Wing Deflections Using Modal Shapes and Strain Pattern Analysis. In *AIAA Scitech 2019 Forum*, number January, pages 1–12, 2019. doi: 10.2514/6.2019-1116.

[6] C.-g. Pak and S. Truong. Creating a Test Validated Structural Dynamic Finite Element Model of the X-56A Aircraft. In *15th AIAA/ISSMO Multidisciplinary Analysis and Optimization Conference AIAA 2014-3157 Downloaded*, number June, pages 1–39, 2014.

[7] Dynamic Design Solutions. FEMtools Product Overview. Essential Tools for Finite Element Based Simulation, Validation, Updating and Optimization. Technical report, 2019.

[8] N. R. Fields. Advantages and challenges of unmanned aerial vehicle autonomy in the postheroic age. Master's thesis, James Madison University, 2012.

[9] A. Timmis, C. Soutis, and A. Schafer. Environmental impact assessment of aviation emission reduction through the implementation of composite materials. *The International Journal of Life Cycle Assessment*, (January 2018):0–31, 2014. doi: 10.1007/s11367-014-0824-0.

[10] J. E. C. Jan R Wright. *Introduction to Aircraft Aeroelasticity and Loads*. John Wiley Sons, Ltd., 2007. ISBN 9780470858400.

[11] Federal Aviation Administration. Part 25. Airworthiness Standards: Transport Category Airplanes, Retrieved 29 March 2010.

[12] Federal Aviation Administration. Part 23. Airworthiness Standards: Transport Category Airplanes, Retrieved 29 March 2010.

[13] T. Megson. *Introduction to Aircraft Structural Analysis*. Elsevier Ltd, 2018. ISBN 9780081020760. doi: 10.1016/B978-0-08-102076-0.00012-9.

[14] D. D. Klerk, D. J. Rixen, and S. N. Voormeeren. General Framework for Dynamic Substructuring : History, Review, and Classification of Techniques. *American Institute of Aeronautics and Astronautics*, 46(5), 2008. doi: 10.2514/1.33274.

[15] M. A. Sutton, J.-J. Orteu, and H. W. Schreier. *Image Correlation for Shape, Motion and Deformation Measurements*. Springer, 2009.

[16] P. Wu, B. Stanford, and P. Ifju. Structural Deformation Measurements of Anisotropic Flexible Flapping Wings for Micro Air Vehicles. In *49th AIAA/ASME/ASCE/AHS/ASC Structures, Structural Dynamics, and Materials Conference*, number April, pages 1–13, 2008.

[17] R. Albertani, B. Stanford, J. P. Hubner, and P. G. Ifju. Aerodynamic Coefficients and Deformation Measurements on Flexible Micro Air Vehicle Wings. *Experimental Mechanics*, pages 625–635, 2007. doi: 10.1007/s11340-006-9025-5.

[18] G. Konecny. Keynote Address : The International Society for Photogrammetry and Remote Sensing-75 Years Old, or 75 Years Young. *The International Society for Photogrammetry and Remote Sensing*, 1985.

[19] H. Schreier, J.-J. Orteu, and M. A. Sutton. *Image Correlation for Shape, Motion and Deformation Measurements*. Springer, Boston, MA, 2009. ISBN 9780387787466.

[20] R. Galvao, E. Israeli, S. Arnold, T. Xiaodong, K. Bishop, S. Swartz, and K. Breuer. The aerodynamics of compliant membrane wings modeled on mammalian flight mechanics. In *Collection of Technical Papers - 36th AIAA Fluid Dynamics Conference*, volume 1, pages 11–22, 2006. ISBN 1563478102. doi: 10.2514/6.2006-2866.

[21] J. D. Jacob, S. W. Smith, D. Cadogan, and S. Scarborough. Expanding the small UAV design space with inflatable wings. *SAE Technical Papers*, (724), 2007. ISSN 26883627. doi: 10.4271/2007-01-3911.

[22] G. A. Fleming, S. M. Bartram, M. R. Waszak, and L. N. Jenkins. Projection moire interferometry measurements of micro air vehicle wings. *Optical Diagnostics for Fluids, Solids, and Combustion*, 4448(November 2001):90, 2001. ISSN 0277786X. doi: 10.1117/12.449365.

[23] N. M. Simões. Design of a Ground Vibration Test Certification System For Unmanned Air Vehicles. Master's thesis, Instituto Superior Técnico, Lisbon, 2015.

[24] F. Castro de Almeida. Design of a Ground Static Load Test for a 3 m Flexible Joined Wing Sensorcraft. Master's thesis, Instituto Superior Técnico, Lisbon, 2017.

[25] S. D. W. Warwick. Measurement of Aeroelastic Wing Deflections on a Remotely Piloted Aircraft using Modal Strain Shapes. Master's thesis, University of Victoria, Canada, 2020.

[26] Crystal Instruments. *Basics of Modal Testing and Analysis*, 2017. URL `https://www.crystalinstruments.com/basics-of-modal-testing-and-analysis/`.

[27] M. Peeters, G. Kerschen, and J. C. Golinval. Dynamic testing of nonlinear vibrating structures using nonlinear normal modes. *Journal of Sound and Vibration*, 330(3):486–509, 2011. ISSN 0022460X. doi: 10.1016/j.jsv.2010.08.028. URL `http://dx.doi.org/10.1016/j.jsv.2010.08.028`.

[28] M. Gurgoze. Identifying nodes and anti-nodes of a longitudinally vibrating rod restrained by a linear spring in-span. *Journal of Sound and Vibration*, 219:550–557, 01 1999. doi: 10.1006/jsvi.1998.1896.

[29] G. Kerschen, M. Peeters, J. C. Golinval, and C. Stéphan. Nonlinear Modal Analysis of a Full-Scale Aircraft. *Journal of Aircraft*, 50(5):1409–1419, 2013. ISSN 0021-8669. doi: 10.2514/1.C031918. URL `http://dx.doi.org/10.2514/1.C031918`.

[30] J. C. Carregado. Static and Dynamic Characterization of a Flexible Scaled Joined-Wing Flight Test Demonstrator. Master's thesis, Instituto Superior Técnico, Lisbon, 2017.

[31] A. Brandt. *Noise and Vibration Analysis: Signal Analysis and Experimental Procedures*. John Wiley Sons, Ltd., 2011. ISBN 9780470746448. doi: 10.1002/9780470978160.

[32] I. Ojalvo and M. Newman. Vibration modes of large structures by an automatic matrix-reduction method. *American Institute of Aeronautics and Astronautics*, 8:1234–1239, 07 1970. doi: 10.2514/3.5878.

[33] F. Abdi and F. Shakeri. Power iteration and inverse power iteration for eigenvalue complementarity problem. *Numerical Linear Algebra with Applications*, (August 2017):1–13, 2019. doi: 10.1002/nla.2244.

[34] J. Beisheim. Ansys Inc.: Introducing the Supernode Eigensolver, Ansys Advantage, vol. III. Technical report, 2009.

[35] U. Füllekrug, G. Gloth, M. Sinapius, P. Fargette, B. Levadoux, P. Lubina, and H. Schaak. Tasks for improvement in ground vibration testing of large aircraft. In *IFASD, Madrid/Spain*, pages 121–133, 01 2001.

[36] D. Göge, M. Böswald, U. Füllekrug, and P. Lubrina. Ground vibration testing of large aircraft -state-of-the-art and future perspectives. In *IMAC-XXV: A Conference Exposition on Structural Dynamics*, 02 2007.

[37] B. Peeters, W. Hendricx, and J. Debille. Modern solutions for Ground Vibration Testing of large aircraft. In *IMAC XXVI*, number June 2014, 2008.

[38] J. Carregado, S. Warwick, J. Richards, F. Engelsen, and A. Suleman. Static and Dynamic Characterization of a Flexible Scaled Joined Wing UAV. *Advances in Aircraft and Spaceraft Science*, 6(2): 116, 2019. doi: https://doi.org/10.12989/aas.2019.6.2.117.

[39] G. Osmond, F. Ayme, and N. Lastere. Dgt : A new methodology for highspeed aircraft ground vibration tests. In *International Forum on Aeroelasticity and Structural Dynamics*, number June, pages 1–11, 2019.

[40] J. Cooley and J. W. Tukey. An algorithm for the machine calculation of complex fourier series. *Mathematics of Computation*, 19:297–301, 1965.

[41] SIEMENS SIMCENTER. What modal impact hammer tip should i use? `https://community.sw.siemens.com/s/article/what-modal-impact-hammer-tip-should-i-use`, 2019. (accessed: 07.11.2020).

[42] SIEMENS SIMCENTER. What is a frequency response function (frf)? `https://community.sw.siemens.com/s/article/what-is-a-frequency-response-function-frf`, 2020. (accessed: 07.11.2020).

[43] SIEMENS SIMCENTER. Modal tips: Roving hammer versus roving accelerometer. `https://community.sw.siemens.com/s/article/modal-tips-roving-hammer-versus-roving-accelerometer`, 2019. (accessed: 07.11.2020).

[44] P. L. Mchargue and M. H. Richardson. Operating deflection shapes from time versus frequency domain measurements. In *11th IMAC Conference, Kissimmee, FL*, pages 1–8, 1993.

[45] Dynamic Design Solutions. FEMtools: Pretest and Correlation Analysis User's Guide. Technical report, 2020.

[46] S. Gade, H. Herlufsen, and H. Konstantin-hansen. Application note: How to Determine the Modal Parameters of Simple Structures. Technical report, Bruel Kjaer, 2012.

[47] R. Allemang and D. Brown. A complete review of the complex mode indicator function (cmif) with applications. In *ISMA2006: International Conference on Noise and Vibration Engineering*, 01 2006.

[48] R. Williams, J. Crowley, and H. Vold. The multivariate mode indicator function in modal analysis. In *IMAC III: International Modal Analysis Conference*, volume 1, pages 66–70, 1985. URL `http://www.systemplus.co.jp/support/data/techpaper/mescope/tech/35.pdf`.

[49] Vibrant Technologies. MEScope: Application Note 13 Introduction to Modal Curve Fitting. Technical report, 2019.

[50] I. Popescu, L. Flore, and A. A. Cubillo. Derivation of mass , stiffness and damping matrices of a model wing from experimental modal data. *Scientific research and education in the air force – AFASES2017*, 2017. doi: 10.19062/2247-3173.2017.19.1.39.

[51] K. Shye and M. Richardson. Mass , Stiffness , and Damping Matrix Estimates from Structural Measurements. In *International Modal Analysis Conference V - IMAC*, pages 1–7, 1987.

[52] Dynamic Design Solutions. FEMtools: Model Updating Theoretical Manual. Technical report, 2014.

[53] R. M. Lin and D. J. Ewins. Analytical model improvement using frequency response functions. In *Mechanical Systems and Signal Processing*, volume 8, pages 437–458, 1994. doi: 10.1006/mssp. 1994.1032.

Appendix A

Data Acquisition
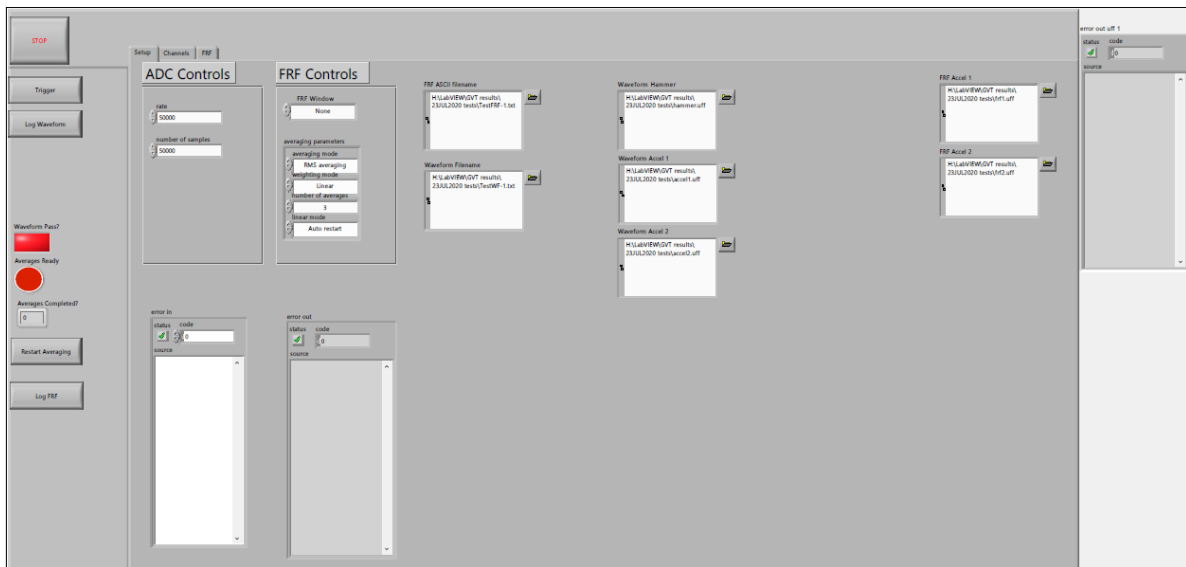
(a) LabVIEW Graphical User Interfaces page 1

(b) LabVIEW Graphical User Interfaces page 2

Figure A.1: LabVIEW Graphical User Interfaces

Model Number **208C01**	**ICP® FORCE SENSOR**	Revision: K ECN #: 45224

Performance	ENGLISH	SI	
Sensitivity(± 15 %)	500 mV/lb	112,410 mV/kN	
Measurement Range(Compression)	10 lb	0.04448 kN	
Measurement Range(Tension)	10 lb	0.04448 kN	
Maximum Static Force(Compression)	60 lb	0.27 kN	
Maximum Static Force(Tension)	60 lb	0.27 kN	
Broadband Resolution(1 to 10,000 Hz)	0.0001 lb-rms	0.00045 N-rms	[2]
Low Frequency Response(-5 %)	0.01 Hz	0.01 Hz	[3]
Upper Frequency Limit	36,000 Hz	36,000 Hz	[4]
Non-Linearity	≤ 1 % FS	≤ 1 % FS	[5]
Environmental			
Temperature Range	-65 to +250 °F	-54 to +121 °C	
Temperature Coefficient of Sensitivity	≤ 0.05 %/°F	≤ 0.09 %/°C	
Electrical			
Discharge Time Constant(at room temp)	≥ 50 sec	≥ 50 sec	
Excitation Voltage	18 to 30 VDC	18 to 30 VDC	
Constant Current Excitation	2 to 20 mA	2 to 20 mA	
Output Impedance	≤ 100 Ohm	≤ 100 Ohm	
Output Bias Voltage	8 to 12 VDC	8 to 12 VDC	[1]
Spectral Noise(1 Hz)	0.0000126 lb/√Hz	0.0000562 N/√Hz	[2]
Spectral Noise(10 Hz)	0.0000042 lb/√Hz	0.0000189 N/√Hz	[2]
Spectral Noise(100 Hz)	0.0000015 lb/√Hz	0.0000067 N/√Hz	[2]
Spectral Noise(1000 Hz)	0.0000005 lb/√Hz	0.0000023 N/√Hz	[2]
Output Polarity(Compression)	Positive	Positive	
Physical			
Stiffness	6 lb/µin	1.05 kN/µm	[2]
Size (Hex x Height x Sensing Surface)	0.625 in x 0.625 in x 0.500 in	15.88 mm x 15.88 mm x 12.7 mm	
Weight	0.80 oz	22.7 gm	
Housing Material	Stainless Steel	Stainless Steel	
Sealing	Hermetic	Hermetic	
Electrical Connector	10-32 Coaxial Jack	10-32 Coaxial Jack	
Electrical Connection Position	Side	Side	
Mounting Thread	10-32 Female	10-32 Female	

CE [6]

All specifications are at room temperature unless otherwise specified.
In the interest of constant product improvement, we reserve the right to change specifications without notice.
ICP® *is a registered trademark of PCB Group, Inc.*

OPTIONAL VERSIONS
Optional versions have identical specifications and accessories as listed for the standard model except where noted below. More than one option may be used.

N - Negative Output Polarity
Output Polarity(Compression)   Negative   Negative

W - Water Resistant Cable

NOTES:
[1]Sensor contains protected electronics which may cause long 'turn-on' times.
[2]Typical.
[3]Calculated from discharge time constant.
[4]Estimated using rigid body dynamics calculations.
[5]Zero-based, least-squares, straight line method.
[6]See PCB Declaration of Conformance PS023 for details.

SUPPLIED ACCESSORIES:
Model 080A81 Thread Locker (1)
Model 081B05 Mounting Stud (10-32 to 10-32) (2)
Model 084A03 Impact Cap (1)
Model M081A62 Mounting stud, 10-32 to M6 x 1, BeCu with shoulder (2)

Entered: LK	Engineer: MJK	Sales: KWW	Approved: APB	Spec Number:
Date: 3/29/2016	Date: 3/29/2016	Date: 3/29/2016	Date: 3/29/2016	**8625**

PCB PIEZOTRONICS
3425 Walden Avenue, Depew, NY 14043

Phone: 716-684-0001
Fax: 716-684-0987
E-Mail: info@pcb.com

Figure A.2: PCB model 086C03 hammer specifications.
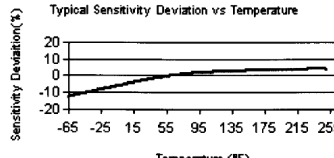
Model Number **352A24**	**ICP® ACCELEROMETER**	Revision: C ECN #: 27171

Performance	ENGLISH	SI	
Sensitivity(± 10 %)	100 mV/g	10.2 mV/(m/s²)	
Measurement Range	± 50 g pk	± 490 m/s² pk	
Frequency Range(± 5 %)	1.0 to 8000 Hz	1.0 to 8000 Hz	
Frequency Range(± 10 %)	0.8 to 10,000 Hz	0.8 to 10,000 Hz	
Frequency Range(± 3 dB)	0.4 to 12,000 Hz	0.4 to 12,000 Hz	
Resonant Frequency	≥ 30 kHz	≥ 30 kHz	
Broadband Resolution(1 to 10,000 Hz)	0.0002 g rms	0.002 m/s² rms	[1]
Non-Linearity	≤ 1 %	≤ 1 %	[2]
Transverse Sensitivity	≤ 5 %	≤ 5 %	
Environmental			
Overload Limit(Shock)	± 5000 g pk	± 49,050 m/s² pk	
Temperature Range(Operating)	-65 to +250 °F	-54 to +121 °C	
Temperature Response	See Graph	See Graph	
Electrical			
Excitation Voltage	18 to 30 VDC	18 to 30 VDC	
Constant Current Excitation	2 to 20 mA	2 to 20 mA	
Output Impedance	≤ 300 ohm	≤ 300 ohm	
Output Bias Voltage	8 to 12 VDC	8 to 12 VDC	
Discharge Time Constant	0.4 to 1.5 sec	0.4 to 1.5 sec	
Settling Time(within 10% of bias)	<8 sec	<8 sec	
Spectral Noise(1 Hz)	80 µg/√Hz	785 (µm/s²)/√Hz	
Spectral Noise(10 Hz)	15 µg/√Hz	147 (µm/s²)/√Hz	[1]
Spectral Noise(100 Hz)	4 µg/√Hz	39 (µm/s²)/√Hz	[1]
Spectral Noise(1 kHz)	1 µg/√Hz	9.8 (µm/s²)/√Hz	[1]
Electrical Isolation(Base)	≥ 10⁸ ohm	≥ 10⁸ ohm	
Physical			
Sensing Element	Ceramic	Ceramic	
Sensing Geometry	Shear	Shear	
Housing Material	Anodized Aluminum	Anodized Aluminum	
Sealing	Epoxy	Epoxy	
Size (Height x Length x Width)	0.19 in x 0.48 in x 0.28 in	4.8 mm x 12.2 mm x 7.1 mm	
Weight	0.03 oz	0.8 gm	[1]
Electrical Connector	3-56 Coaxial Jack	3-56 Coaxial Jack	
Electrical Connection Position	Side	Side	
Mounting	Adhesive	Adhesive	

Typical Sensitivity Deviation vs Temperature

OPTIONAL VERSIONS
Optional versions have identical specifications and accessories as listed for the standard model except where noted below. More than one option may be used.

RH - RoHS Compliant
Supplied Accessory : Model RH030A10 Coax Cable, 10 ft (3 m), 3-56 plug to 10-32 plug, RoHS compliant. replaces Model 030A10

NOTES:
[1] Typical.
[2] Zero-based, least-squares, straight line method.
[3] See PCB Declaration of Conformance PS023 for details.

SUPPLIED ACCESSORIES:
Model 030A10 Coax Cable, 10 ft (3 m), 3-56 plug to 10-32 plug. (1)
Model 039A28 Removal Tool (1)
Model 080A109 Petro Wax (1)
Model ACS-1 NIST traceable frequency response (10 Hz to upper 5% point). (1)

Entered:	Engineer:	Sales:	Approved:	Spec Number:
Date: 8-23-07	Date: 8-23-07	Date: 8-23-07	Date: 8-23-07	**12320**

CE [3]

All specifications are at room temperature unless otherwise specified.
In the interest of constant product improvement, we reserve the right to change specifications without notice.
ICP® *is a registered trademark of PCB Group, Inc.*

PCB PIEZOTRONICS
VIBRATION DIVISION
3425 Walden Avenue, Depew, NY 14043

Phone: 716-684-0001
Fax: 716-685-3886
E-Mail: vibration@pcb.com

Figure A.3: PCB miniature single axis piezoelectric accelerometers model 352A24specifications.